CHARACTERIZATION OF IONIZING RADIATION GENERATED FROM INTERACTION OF HIGH-INTENSITY LASER WITH MATTER

A Dissertation
Presented to
The Academic Faculty

by

Taiee Ted Liang

In Partial Fulfillment
Of the Requirements for the Degree
Doctor of Philosophy in Nuclear & Radiological Engineering
In the George W. Woodruff School of Mechanical Engineering

Georgia Institute of Technology
May 2017

CHARACTERIZATION OF IONIZING RADIATION GENERATED FROM INTERACTION OF HIGH-INTENSITY LASER WITH MATTER

Approved by:

Dr. Nolan E. Hertel, Committee Chair
George W. Woodruff School of
Mechanical Engineering
Georgia Institute of Technology

Dr. C. K. Chris Wang
George W. Woodruff School of
Mechanical Engineering
Georgia Institute of Technology

Dr. Chaitanya S. Deo
George W. Woodruff School of
Mechanical Engineering
Georgia Institute of Technology

Dr. Sayed H. Rokni
Radiation Protection and Physics
SLAC National Accelerator Laboratory

Dr. Anna Erickson
George W. Woodruff School of
Mechanical Engineering
Georgia Institute of Technology

Date Approved: March 7, 2017

ACKNOWLEDGEMENTS

I would like to thank my family first and foremost. It has been a long journey with a few *hearty* bumps along the way, but I have made it! To my parents Mom and Dad, thank you for your many years of support and encouragement although I always had difficulty explaining to you what I was actually doing! I suppose I no longer have an excuse to find my *Rebecca* now! To my brother Justin, your drive and enthusiasm has been an inspiration, and never stop pursuing your dreams. To my sister Hannah, your joy and cheeriness has been a blessing, and I will admit those many late hours of physics tutoring were entertaining.

Before my Ph.D. journey began, I remember being distinctly drawn towards the radiation side of my undergraduate program by Dr. Hertel's Radiation Sources and Applications course. Thank you for agreeing to be my advisor (even though I often sat in the front row and fell asleep) and opening up a world of research opportunities to pursue whether at Tech, Kewaunee, TRU, and SLAC. Thank you also for your prayer and anointment when I was terribly sick that one time. It was quite special, and I will never forget it.

Remembering the many fun times with my friends and colleagues at ORS: Nazia, Gary, Christina, Arlene, Alice, Aaron, Cal, Jenny, Margaret, Jake, Darrell, and Bopp. Wow, there was actually quite a few of us in those short years! It was fantastic to have the opportunity to work with you all! Also, I would especially like to thank Christina for saving my life because without that, I would not have finished my doctorate at all!

Over on the west coast in sunny California, I would like to thank Sayed Rokni for guiding my dissertation research at SLAC. I have learned so much from you over

those few years, and I am very excited for what my future experiences at SLAC will bring! Also thank you and your family for your hospitality for several Thanksgiving dinners. And for the times you offered a ride home in the rainy season, so I did not have to bike in the rain. Your thoughtfulness and hospitality are greatly appreciated!

Furthermore, I would like to thank all my many friends and colleagues from SLAC's Radiation Protection group. It was a great experience working with and learning from all of you in your expertises! Thank you all for the many fond memories during my time at SLAC (too many to list them all): Johannes for the fun little discussions on the nuances of the English language and correcting my grammar, James for your incredible attention to detail and your wife's tasty desserts, Ludovic and Mario for dealing with my bombardment of FLUKA questions, Mike for introducing me to Rufus and learning how to take care of a dog for the first time in my life, Keith and Eddie for introducing me to lunch-time ping pong and all the tricks that came with it, Darryl for sharing delicious barbecue with me.

I am also very grateful to the scientists and supporting staff of the Matter in Extreme Conditions for their crucial role in the many laser experiments I participated in while at SLAC. It was a great experience collaborating with you all, and thank you for your patience and willingness to explain laser *things* to someone who had previously no background in the subject matter! On the same note, I am very grateful to Rohini Mishra and again her patience and willingness to help with my PIC work and understanding plasma physics concepts.

Support from my friends on the east coast to the west coast and everything in between, thank you all for the many years and the fun times.

Thank you all for your support!

TABLE OF CONTENTS

LIST OF TABLES

LIST OF FIGURES

SUMMARY

Technological advances allow an increasing number of facilities around the world to install high-power multi-terawatt and petawatt lasers. These high-power lasers can be focused to high-intensities greater than 10^{17} W cm^{-2} onto target materials to study matter at higher pressures and temperatures. The interaction of a high-intensity laser with matter in vacuum creates a plasma layer on the surface of the target. Additional interactions between the remainder of the laser pulse and the plasma can accelerate electrons in the plasma up to tens and hundreds of MeV in energy. These 'hot' electrons escape from the plasma and interact with the target material and the target vacuum chamber walls and generated bremsstrahlung photons, which can pose an ionizing radiation hazard for personnel working near these laser facilities if radiation shielding is insufficient. Identifying the relation between the laser-plasma interactions and the magnitude of the radiation yields are crucial in developing radiological controls for high-intensity laser facilities.

The particle-in-cell (PIC) method plasma code EPOCH can simulate the laser-plasma interactions and characterize key parameters of the hot electron source term, including the energy distribution, angular distribution, and laser-to-electron conversion efficiency. The Monte Carlo radiation transport and interaction code FLUKA can utilize EPOCH's hot electron source term to calculate the bremsstrahlung photon yields at various angles. A systematic study from coupling EPOCH and FLUKA to develop a bremsstrahlung dose yield source term as a function of laser intensities between 10^{17} and 10^{22} W cm^{-2} is presented, and comparisons with measurement data are also made.

CHAPTER I

INTRODUCTION

1.1 Motivation for high-intensity laser experiments

In recent years, the number and use of high-power lasers to explore laser-matter interactions in research facilities have rapidly increased around the world, and upgrades to pre-existing laser facilities continue to push the envelop in reaching higher laser powers in multi-terawatts and even petawatt range and focusing the laser beam down to micrometer spot sizes to reach increasingly higher laser intensities.

The scientific community use these facilities to perform experiments of matter under extreme conditions (high energy density physics) by focusing the laser to micrometer spot sizes onto matter.[47] Despite its rather short-lived nature in the laboratory setting, matter under extreme conditions (or MEC) is found abundantly in nature and is of interest to scientists in astrophysics and planetary physics. For example, the interior of giant gas planets such as Jupiter, Saturn, Uranus, and Neptune are primarily composed of matter under high pressure and high density conditions.[26]

One byproduct of creating matter under conditions is the generation of high energy electrons, which is also of interest to the scientific community. The interaction between a high-intensity laser and matter can even produce GeV-class beams of electrons, which can be a potential seed for the next generation of synchrotron radiation facilities and free-electron lasers.[38] During these experiments, a gas target is fully ionized by the high-intensity laser to form a plasma, and the electrons in the plasma are accelerated by laser wakefield acceleration that takes advantage of an intense laser pulse that drives a large electric field (the wakefield) on the order of 10–100 GV m^{-1} within very short distances of a few millimeters.[23,20,16] The high-energy electrons

produced from this laser-plasma interaction can further 'wiggle' as a result of the electric field of the plasma and produce pure, highly-collimated beams of betatron X-rays, which has unique applications as a potential diagnostic light source.[14,3]

The interaction of a high-intensity laser with matter can also be used to generate beams of protons (and ions). The laser-generated protons are emitted from the rear and front surfaces of thin solid targets with energies up to tens of MeV. Furthermore, these ions are often highly directional. Laser-induced proton sources have potential applications in the fields of radiotherapy and radiography, and allow for medical facilities to have access to a cheaper and more compact source of MeV-range protons. Outside of medicine, they can also be used as injectors for conventional proton accelerators.[55,19,28]

High-intensity lasers can also be used as a driver in the fast ignition approach to inertial confinement fusion, where supra-thermal electrons from high-intensity laser-plasma interactions ignite the fusion fuel pellet. Studying the interaction of a high-intensity laser with matter in the laboratory setting can provide insight into the material properties of the fuel under high energy and high density conditions.[57]

1.2 Source of laser-induced ionizing radiation

High-intensity lasers have a wide variety of research applications in science, and their use only continue to grow among the international science communities. Figure 1 demonstrates the widespread use of high-intensity lasers worldwide, which has seen especially rapid growth in the United States, Europe, and Asian in particular.

However, as these laser facilities continue grow, the radiation protection of these facilities must be considered. The interaction of a high-intensity laser with a solid target creates a plasma layer on the surface of the target. Further laser interactions with the plasma accelerates electrons in the plasma to tens and hundreds of MeV in energy.[58,59] These 'hot' electrons will interact with the laser target and the target

Figure 1: Map of the high-intensity laser facilities located around the world from 2011. Image from The International Committee on Ultra-High Intensity Lasers (ICUIL).[2]

vacuum chamber and generate bremsstrahlung photons.[27,13] This mixed field of electrons and photons is a source of ionizing radiation and can create a radiation hazard for personnel unless sufficient radiological controls are implemented.

1.3 Thesis objectives

Currently, the majority of radiation protection dose data and shielding practices for high-intensity laser-solid experiments is scattered and only describes conditions for a small range of laser intensities unique to each facility. Furthermore, the relation between the ionizing radiation yields and laser-optic parameters is crucial in evaluating hazards and developing radiological controls, but they are also not well quantified yet. The work presented here is part a multi-year effort focused on the radiation protection of high-intensity laser facilities and in collaboration with colleagues from SLAC National Accelerator Laboratory (SLAC), the Georgia Institute of Technology, Helmholtz-Zentrum Dresden-Rossendorf (HZDR) in Germany, Rutherford Appleton Laboratory (RAL) in United Kingdom, Extreme Light Infrastructure (ELI) in Czech

Republic, and Tsinghua University (THU) in China.

The primary objectives of this thesis are twofold. The energy distribution, angular distribution, and laser-to-electron energy conversion efficiency of the hot electron source generated from high-intensity laser-solid interactions will be characterized. A bremsstrahlung source term from the characterized hot electrons will be developed to estimate the radiation hazard to personnel at these high-intensity laser facilities. These objectives will cover the full range of laser intensities generated from terawatt and petawatt laser systems. The source terms will be evaluated by systematic measurements at SLAC's MEC laser facility and by coupling the particle-in-cell (PIC) method plasma code EPOCH and the Monte Carlo multi-particle transport and interaction code FLUKA.

CHAPTER II

LASER-MATTER INTERACTIONS

2.1 Laser basics

2.1.1 Gaussian laser beam

Before relating laser-optics parameters with the generated radiation yields, it is important to clearly define several laser parameters used specifically for characterizing Gaussian laser beams. The power of a laser is the amount of energy contained in a laser pulse compressed within the pulse's duration (or pulse length). For example, a laser pulse with energy of 1 J delivered within 40 fs gives a laser power of 25 TW. The intensity of a laser pulse describes its power per unit area and is commonly expressed in units of W cm^{-2}. Achieving high laser intensities requires focusing the laser beam with mirrors to small spot sizes within a vacuum.[61] Under vacuum conditions, a Gaussian laser beam can be focused to much smaller spot sizes and higher intensities than in air where laser intensity is limited by air ionization to an upper limit of about 5×10^{14} W cm^{-2}.[63]

The radial intensity of a Gaussian beam is given by Equation 1 where P is the laser power (Watts) and ω is the laser beam's $1/e^2$ radial spot size (meters).

$$I(r) = \frac{2P}{\pi\omega^2}\, e^{-2r^2/\omega^2} \tag{1}$$

The $1/e^2$ radial spot size is where the intensity has dropped to $1/e^2 \approx 0.135$ of its peak intensity and can be approximated by the product of the focusing optic's f-number f# and the laser wavelength λ ($\omega \approx \text{f\#} \cdot \lambda$). Again, the laser power P is simply the laser energy (Joules) contained within a small (or short) pulse length (seconds). Short-pulse lasers operate on a femtosecond time-scale are ideal in achieving high

intensities because they compress a few Joules of energy within a small amount of time.

It is common practice to describe a laser beam by its 'peak' intensity as $r \to 0$, which is given in Equation 2.

$$I_0 = \lim_{r \to 0} \frac{2P}{\pi\omega^2}\, e^{-2r^2/\omega^2} = \frac{2P}{\pi\omega^2} \tag{2}$$

The peak laser intensity will simply be referred to as laser intensity for the remainder of this dissertation. When comparing laser intensities from different lasing mediums, it is useful to normalize the laser beam's intensity I to its wavelength λ. For example, the short-pulse laser at MEC utilizes a Ti:sapphire crystal tuned to wavelength of 0.8 μm, whereas another facility may utilize Nd:YAG tuned to a wavelength of 1.064 μm. To compare the two lasers, the normalized laser intensity $I\lambda^2$ in units of W μm^2 cm^{-2} is used.

2.1.2 Laser strength parameter

Similar to the $I\lambda^2$ term, the laser strength parameter (or normalized laser amplitude) is also a common method for comparing different laser systems as it also accounts for wavelength

$$a_0 = \sqrt{\frac{e^2(I\lambda^2)}{2\pi^2 c^5 \epsilon_0 m_e^2}} \tag{3}$$

$$= \sqrt{\frac{I\lambda^2}{1.37 \times 10^{18}}} \tag{4}$$

where e is the electron's elementary charge (coulombs), c is the speed of light in vacuum (m s^{-1}), ϵ is the vacuum permittivity (F s^{-1}), and $I\lambda^2$ is the normalized laser intensity (W μm^2 cm^{-2}).[22] The laser strength parameter also describes if the motion of an electron oscillating in the electromagnetic field of the laser is in the relativistic regime ($a_0 \geq 1$), which is the ponderomotive force that will be covered later.[35]

2.1.3 Laser pre-pulse

A laser pre-pulse is an important property of short pulse high-intensity lasers. The laser pre-pulse precedes the main laser pulse on a nanosecond time-scale and will also interact with the target before the main pulse. The schematic in Figure 2 gives the typical power-time profile of a short-pulse laser where P_0 is the power of the main pulse and P_p is the power of the pre-pulse. The ratio between the powers of the main pulse and the pre-pulse is referred to as the laser system's contrast ratio. For example, the contrast ratio for the Ti:sapphire laser at the MEC laser facility has been measured to be in the range of 10^{10}.[25]

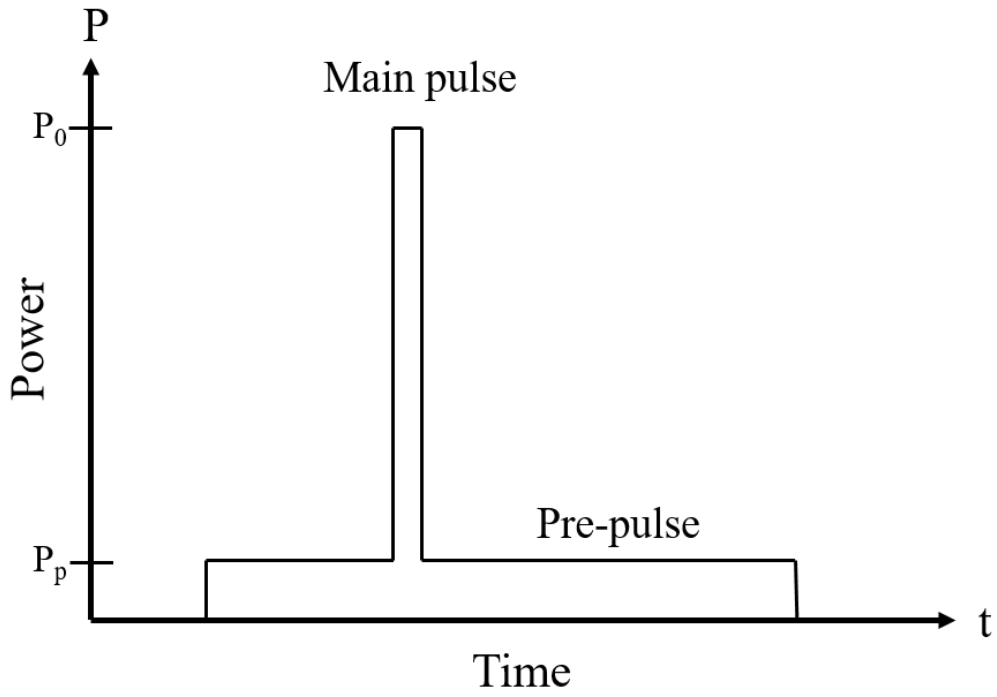

Figure 2: Typical power-time profile of a short-pulse laser where P_0 is the power of the main pulse and P_p is the power of the pre-pulse.

The pre-pulse of a high-intensity laser pulse is sufficient to ionize the target material and create a pre-plasma that expands off the surface of the target, which all takes place before the main pulse even arrives. Pre-pulse and pre-plasma will influence the

main pulse's eventual interaction with the target material and affects plasma properties such as density gradient, energies of the plasma electrons, and conversion of laser light energy to hot electron energy. This can significantly affect the acceleration of the hot electrons inside the plasma.[4] Depending on the experimenters' scientific motivation, various methods and techniques have been found to reduce or increase the laser pre-pulse.[32]

2.1.4 MEC laser facility at SLAC

Parameters of the short-pulse laser located at the MEC laser facility were frequently used as examples in the previous sections and are summarized below for 25 TW operation:

- Ti:sapphire wavelength, $\lambda = 0.8$ μm
- laser pulse energy, $E = 1.0$ J
- short-pulse length, $\tau = 40$ fs
- $1/e^2$ radial spot size, $\omega \sim 10$ μm
- peak laser intensity, $I \sim 10^{20}$ W cm^{-2}
- pulse repetition rate, $f = 1$ Hz

Plans for future upgrades will increase the laser power to 200 TW (8 J in 40 fs) and 500 TW (50 J in 100 fs) to higher laser intensities on the order of 10^{21} W cm^{-2} and above.

2.2 Plasma basics

2.2.1 Plasma formation

A laser pulse's initial interaction with a solid opaque target heats the surface and creates a low density transparent vapor consisting of neutral atoms of the target material. Ionization of the neutral atoms can be produced via multi-photon ionization,

where several photons of energy below the ionization threshold combine their energies to ionize a neutral atom. The probability of multi-photon ionization decreases rapidly with the number of photons required, but a high-intensity laser pulse can overcome this barrier.

An avalanche effect soon follows as the 'seed' electrons from multi-photon ionization oscillate with the laser's electric field ($q\mathbf{E}$ of the Lorentz force). These electrons gain energy through collisions with atoms, and with sufficient electron energy, a collision will produce a new electron. More electrons are produced with each subsequent generation of electrons, and an electron avalanche occurs. Due to this process, a plasma is formed on the target surface and begins to absorb the laser energy.[44]

2.2.2 Plasma parameters

Several key parameters for describing laser-plasma interacts are governed by the laser wavelength λ. The laser angular frequency ω_0 is defined in Equation 5 where c is the speed of light in vacuum.

$$\omega_0 = 2\pi \cdot \frac{c}{\lambda} \tag{5}$$

For a given laser frequency ω_0 and wavelength λ, the critical plasma density n_c can be calculated from Equations 6 and 7. The critical plasma density is the density at which the frequency of the plasma oscillation is equal to the frequency of the laser. This is also density to which a laser pulse is able to propagate, upon which the pulse energy is partially absorbed with some fraction reflected.

$$n_c = \frac{\omega_0^2 \epsilon_0 m_e}{e^2} \tag{6}$$

$$= \frac{1.1 \times 10^{21}}{\lambda^2\ [\mu\mathrm{m}]^2}\ \frac{1}{cm^3} \tag{7}$$

Also related to the laser angular frequency ω_0 is the plasma skin depth δ in Equation 8, which is the depth in a plasma to which electromagnetic radiation can penetrate. For a wavelength of 0.8 μm, Equations 7 and 8 give n_c of 1.72×10^{21} cm^{-3}

and δ of 0.13 μm.

$$\delta = \frac{c}{\omega_0} \tag{8}$$

A few high power lasers and their laser and plasma parameters covered earlier are given in Table 1. The laser in use at SLAC MEC is a Ti:sapphire laser.

Table 1: Laser and plasma parameters of a few high-power lasers.

Laser	λ (μm)	ω_0 (s^{-1})	$\hbar\omega$ (eV)	n_c (cm^{-3})	δ (μm)
CO_2	10.6	1.78×10^{14}	0.12	1.0×10^{19}	1.7
I	1.315	1.43×10^{15}	0.94	6.5×10^{20}	0.21
Nd	1.06	1.78×10^{15}	1.17	1.0×10^{21}	0.17
Ti:sapphire	0.8	2.35×10^{15}	1.55	1.8×10^{22}	0.13

As described earlier, a solid target irradiated by a laser pulse has a plasma that extends out into vacuum. The profile of the plasma density n_e follows that of a simple exponential function in one-dimension

$$n_e(x) = n_{solid} \exp\left(-\frac{x}{L_s}\right) \tag{9}$$

where n_{solid} is the electron density of the solid material, x is the distance from the peak density at n_{solid}. The slope of the exponential is characterized by the plasma scale length L_s that is the distance at which the density drops by a factor of $1/e$ (~ 0.3679), where e is Euler's number. At times, the plasma scale length can be seen normalized to the laser wavelength as the dimensionless ratio L_s/λ.

The parameters covered in this section all affect the interaction of the laser pulse with the plasma and can influence the dominant plasma heating mechanism, the conversion from laser energy to electron energy, penetration depth of the laser pulse, and even the subsequent generation of secondary particles from energetic electrons.

2.2.3 Hot electron temperature

The accelerating force experienced by the electrons in the plasma from the laser is given by the Lorentz force $\mathbf{F_L}$ equation

$$\mathbf{F_L} = \frac{d\mathbf{p}}{dt} = m_e \frac{d(\mathbf{v}\gamma)}{dt} = -q\left(\mathbf{E} + \mathbf{v} \times \mathbf{B}\right) \tag{10}$$

where $\mathbf{p}$ and $\mathbf{v}$ are the electron's momentum and velocity, $\mathbf{E}$ and $\mathbf{B}$ are the laser's electric and magnetic fields, and $\gamma = \left(1 - {}^{v^2}/_{c^2}\right)^{-1/2}$. From the Lorentz equation, the electron experiences the ponderomotive force and oscillates with the electromagnetic field of the laser pulse. At high laser intensities, the force on the electrons due to the magnetic component, $q\left(\mathbf{v} \times \mathbf{B}\right)$ or more simply $\mathbf{j} \times \mathbf{B}$, becomes comparable to the force resulting from the electric field and accelerates electrons in the direction of laser propagation. For clarity, the accelerated electrons will be referred to as hot electrons for the remainder of the dissertation.

The acceleration of hot electrons from the laser results in a Maxwellian distribution, which can be can be expressed as a function of the electron energy as

$$f(E) \sim E^{1/2} \exp\left(-\frac{E}{T_h}\right) \tag{11}$$

where T_h is the key parameter known as the hot electron temperature. The electron distribution has an average energy of $1.5 \times T_h$.

Some sources in literature have also used the relativistic Maxwellian distribution for the hot electron population, which is a higher energy (or harder) spectrum with an average electron energy of $3 \times T_h$. The choice of energy distribution will significantly affect the magnitude of the generated radiation hazard, and this dissertation will investigate which distribution is more appropriate.

$$f(E) \sim E^{2} \exp\left(-\frac{E}{T_h}\right) \tag{12}$$

The hot electron temperature T_h characterizes the slope of the energy distribution and scales with laser intensity. Literature reports several different power scaling laws

for the hot electron temperature. For short-pulse laser intensities on the order of $I\lambda^2 > 10^{17}$ W μm^2 cm^{-2}, the dominant heating mechanism is the ponderomotive $\mathbf{j} \times \mathbf{B}$ scaling given by Wilks *et al.* (1992) as

$$T_h = m_e c^2 \left(\sqrt{1 + \frac{I\lambda^2}{1.37 \times 10^{18}}} - 1 \right) \tag{13}$$

where $m_e c^2$ is the electron rest mass of 0.511 MeV.[60]

At lower laser intensities between 10^{12} to 10^{17} W μm^2 cm^{-2}, inverse bremsstrahlung and resonance absorption are the dominant absorption mechanisms, and the hot electron temperature scales with $(I\lambda^2)^{1/3}$. Meyerhofer *et al.* described a temperature scaling based on experimental results with Equation 14.[59,45]

$$T_h \, [\text{MeV}] = 6 \times 10^{-8} \left(I\lambda^2 \right)^{0.33} \tag{14}$$

At intensities higher than 10^{17} W μm^2 cm^{-2}, inverse bremsstrahlung and resonance absorption do contribute to the total acceleration of hot electrons, but they will not be dominant factors. The same concept can also be applied in reverse for the ponderomotive $\mathbf{j} \times \mathbf{B}$ heating. Figure 3 summarizes the relationship between laser parameters (λ_L, a_0, θ_L) and plasma parameters (n_c, L_s) and the resulting hot electron heating mechanism that is dominant. During the laser-plasma interactions, all heating mechanisms are expected to generate hot electrons but to varying degrees.

It must be noted that the electron energy distribution within the plasma is not directly measured in literature but inferred from emission of secondary particles and activated materials in conjunction with laser-plasma simulation codes. Numerous other scaling laws for the hot electron temperature are also reported in literature besides the two from Equations 13 and 14.

The numerous scaling laws make identifying the proper hot electron temperature for a specific laser-solid experiment very difficult. In a later section, this dissertation will present plasma code simulations for the hot electron temperature as a function of laser intensity. Comparison to several scaling laws from literature will also be made.

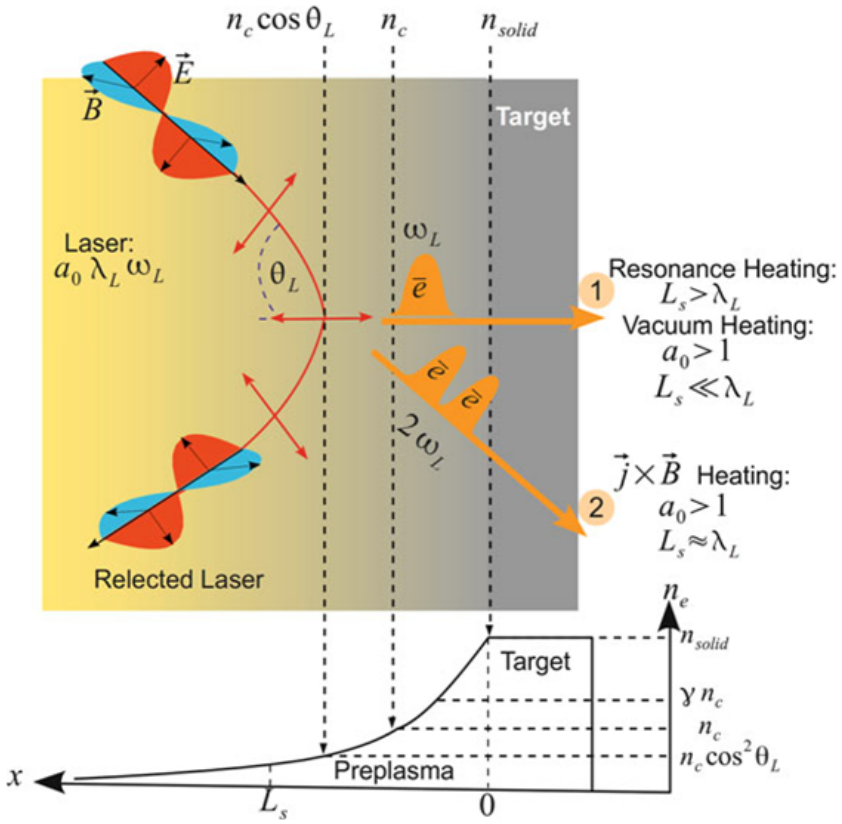

Figure 3: Relationship between laser parameters (λ_L, a_0, θ_L), plasma parameters (n_c, L_s), and hot electron heating mechanisms. Image from the textbook *Laser-Plasma Interactions and Applications* by McKenna *et al.*[44]

2.3 Sources of ionizing radiation

The hot electrons generated from laser-plasma interactions are the primary source of ionizing radiation. As they stream out of the plasma, they interact with the target material and target chamber and generate secondary sources of ionizing radiation such as bremsstrahlung. In most cases, the experimental target chamber is adequate to attenuate the majority of the hot electrons but may not be sufficient for bremsstrahlung, which will create a radiation hazard to personnel working near the facility.

In addition, high-energy bremsstrahlung in the MeV energies can induce photonuclear interactions and generate neutrons via (γ, n). This is especially likely to occur for hot electrons in the high-energy tail (tens of MeV) of the Maxwellian distribution in Equation 11. Of course, the tail portion is a small fraction of the overall

hot electron population, and neutron hazards will be comparatively low compared to electrons and photons. However, at very high laser intensities when electrons in the tail can be in the hundreds of MeV, a neutron hazard may be generated and may even require dedicated local shielding, such as polyethylene.

CHAPTER III

CHARACTERIZATION OF THE HOT ELECTRON SOURCE

3.1 EPOCH: plasma physics simulation code

The code EPOCH is a computational plasma physics simulation code and utilizes the particle-in-cell (PIC) algorithm to study high energy density physics and laser-plasma interactions. The code was developed at the University of Warwick as part of an open collaboration project to develop an advanced relativistic electromagnetic PIC code.[5,8]

The PIC method is suitable for simulating femtosecond, micron-scale laser-to-plasma interactions that are typical at the MEC laser facility at SLAC and other short-pulse laser facilities worldwide. In the EPOCH simulation, physics particles (such as the electrons in a plasma) are represented by a smaller number of macro-particles. Interactions between macro-particles and electromagnetic fields (such as from an incident laser pulse) are tracked iteratively over time with two coupled solvers. The particle pusher moves charged particles under the influence of electromagnetic fields and calculates the currents due to particle motions. The field solver solves Maxwell's equations on a fixed spatial grid subject to the currents calculated from the particle motions. This completes the iterative loop and allows the code to cycle through again. Macro-particle weighting is adjusted in the intermediate steps of the iteration process. Figure 4 visualizes the computational cycle of the PIC method, where the subscript *'i'* notates macro-particles and *'j'* notates spatial grids.[5,8]

For the purpose of this dissertation, EPOCH was used to simulate the interaction of a high-intensity short-pulse laser beam with an initialized plasma target composed

of populations of electrons and ions. Heating of the electron population by the incident laser pulse and conversion of the laser pulse energy to electron energy were investigated by tracking their kinetic energy over each iterative loop of the code. Angular information of the electrons was derived from tracking their spatial momentum (p_x, p_y, and p_z). Characterization of the electrons with EPOCH compose the hot electron source term from laser-plasma interactions: energy distribution, angular distribution, and laser-to-electron energy conversion efficiency.

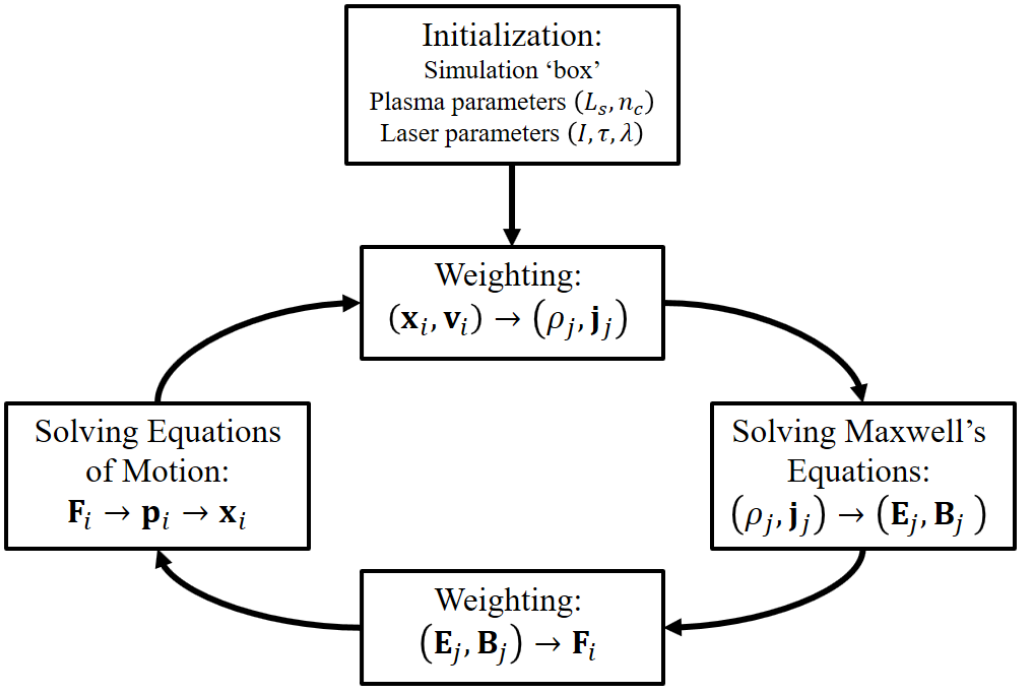

Figure 4: Computational loop starts after initialization of the plasma target and incident laser pulse. Macro-particles are assigned to the spatial grid, and with resulting charge and current densities, the Maxwell equations are solved. The fields are interpolated to the particles' positions, and the equations of motion are solved for each particle.[22]

3.2 EPOCH input parameters

Simulations of laser-plasmas interactions were performed using EPOCH in two dimensions (2D). The simulation box was 20 μm long (in x) by 20 μm wide (in y) on a 400 by 400 grid (grid size of 0.05 μm). Outflow boundary conditions (fields and particles

removed from simulation) were applied to the longitudinal 'left and right' boundaries in x. Periodic boundaries (fields and particles wrapped to opposite boundary) were applied to the lateral 'top and bottom' boundaries in y. The simulation was followed with a time step of 0.1 fs to a total time of 400 fs. At 400 fs, the laser beam has completely interacted with plasma, and the peak hot electron energies have already been achieved.

A p-polarized laser beam with wavelength (λ) of 0.8 μm was emitted from the left boundary and propagated in x. The laser had a peak intensity (I) expressed in W cm^{-2} with a Gaussian profile in space and time: $1/e^2$ radial spot size (ω_0) of 2 μm and FWHM pulse length (τ) of 40 fs. This spot size, together with peak intensity I, sets the total laser pulse energy. Figure 5 shows a snapshot of the kinetic energy of electrons inside the EPOCH simulation described above at 120 fs for an incident laser pulse with an intensity of 10^{20} W cm^{-2}.

The laser pulse interacted with a plasma target composed of electrons and Cu ions. The use of Cu foils for high-intensity laser experiments is common at MEC and many other facilities. Implementing Al or Au ions in EPOCH only resulted in small variations energy distribution and angular distribution of the hot electron source term. The metal ions are much more massive than the electrons in a plasma, so they move very little on a femtosecond time-scale and do not significantly affect electron heating. Similar to another study, it was concluded that dependence of the hot electron source on different metal targets was negligible.[12] On the other hand, dependence on target material (in particular, low-Z plastics) has been found to affect electron heating for long-pulse (picosecond to nanosecond time-scale) laser experiments. However, this is both beyond the scope of this dissertation and beyond the intended use of PIC codes but would instead require simulations with hydrodynamic codes.[31]

The plasma target in EPOCH has an exponential density ramp (Equation 9), which represents the behavior of pre-plasma expanding from the surface of the solid

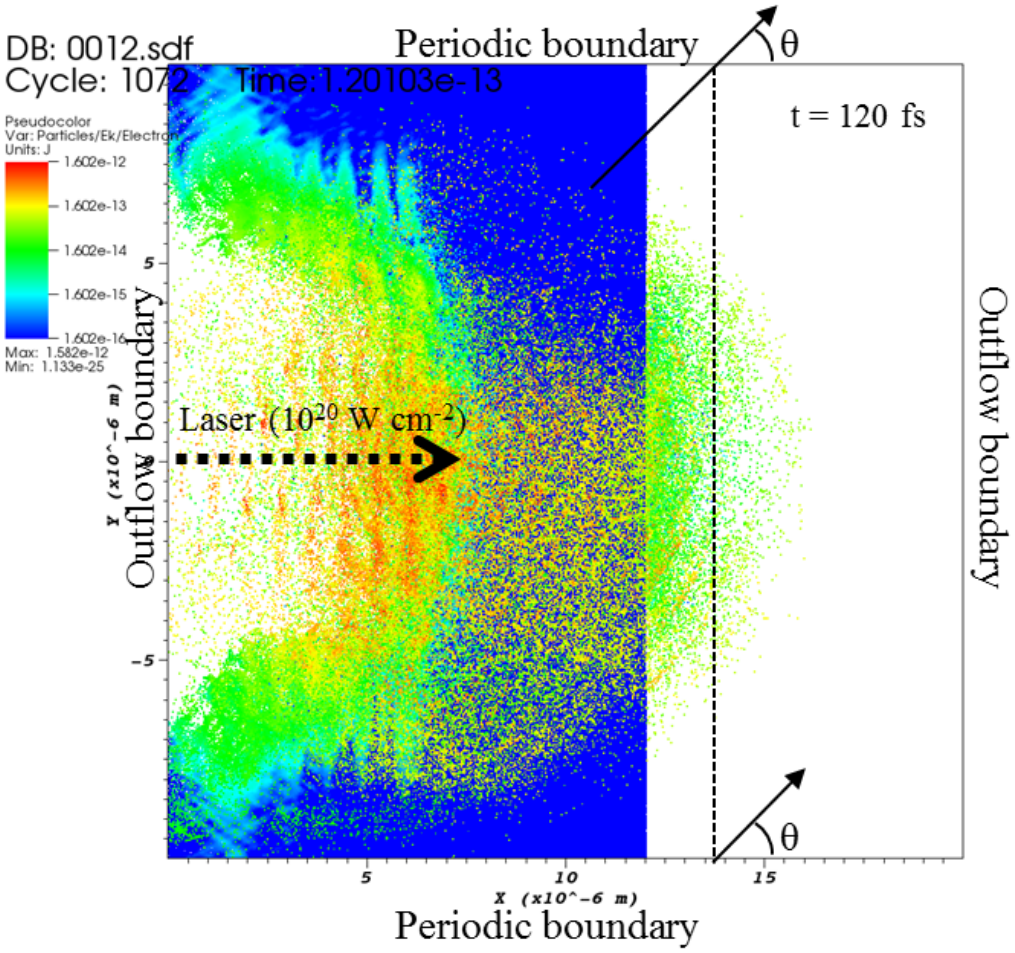

Figure 5: Snapshot of the kinetic energy of electrons inside a 2D EPOCH simulation at 120 fs. The laser is emitted from the left boundary, propagates in x, and interacts with the plasma target. The color scale is increasing in energy from 1 keV to 10 MeV.

target due to the laser's pre-pulse preceding the main pulse. The pre-plasma has a density ramp from $0.01n_c$ to $10n_c$ with a plasma scale length (L_s) that was optimized for maximum energy of the generated hot electrons.[43] The plasma scale length L_s characterizes the density gradient of the plasma as the distance at which the electron density drops to $1/e$. Following the density ramp, the plasma target has a 4 μm-thick flat density region of $10n_c$. An example of the EPOCH input code used in this dissertation is provided in Appendix A.

3.3 Hot electron source term

The following section details the characterization of the hot electron source term from laser-plasma interactions. The hot electron source term is composed of its energy distribution, angular distribution, and laser-to-electron energy conversion efficiency.

3.3.1 Hot electron energy distribution

Characterization of the hot electrons from PIC simulations involves fitting the slope of the high energy tail of the electron energy spectrum in Figure 6. This slope is commonly referred to as the hot electron temperature or T_h of the hot electron energy spectrum. Fitting different energy bounds of the higher energy tail may result in slightly different values for T_h, so the peak T_h value is the one reported.

During an EPOCH simulation of a laser-plasma interaction, the hot electron energy spectrum has two main components: the electrons currently inside the simulation system and the hot electrons that have streamed out of the boundaries of the system. There is also a low energy background population of 'cold' electrons that remain trapped in the plasma. As an example, Figure 6(a) plots the hot electron energy spectrum inside the simulation system at simulation times (or 'snapshots') of 200, 300, and 400 fs calculated from an EPOCH simulation with a laser intensity of 10^{20} W cm^{-2} and laser wavelength of 0.8 μm. From the same simulation, Figure 6(b) plots the hot electron energy spectrum integrated from 0 to 400 fs (total time) that streams forward out of the right boundary of the simulation system. Both hot electron energy spectra can be fitted well with the Maxwellian distribution in Equation 15.

$$f(E) \sim E^{1/2} \ \exp\left[-\frac{E}{T_h}\right] \tag{15}$$

In Equation 15, E is the electron energy (MeV) and T_h is the hot electron temperature (MeV). The Maxwellian fits for Figures 6(a) and 6(b) give T_h of 2.1 and 2.0, respectively, which are in good agreement.

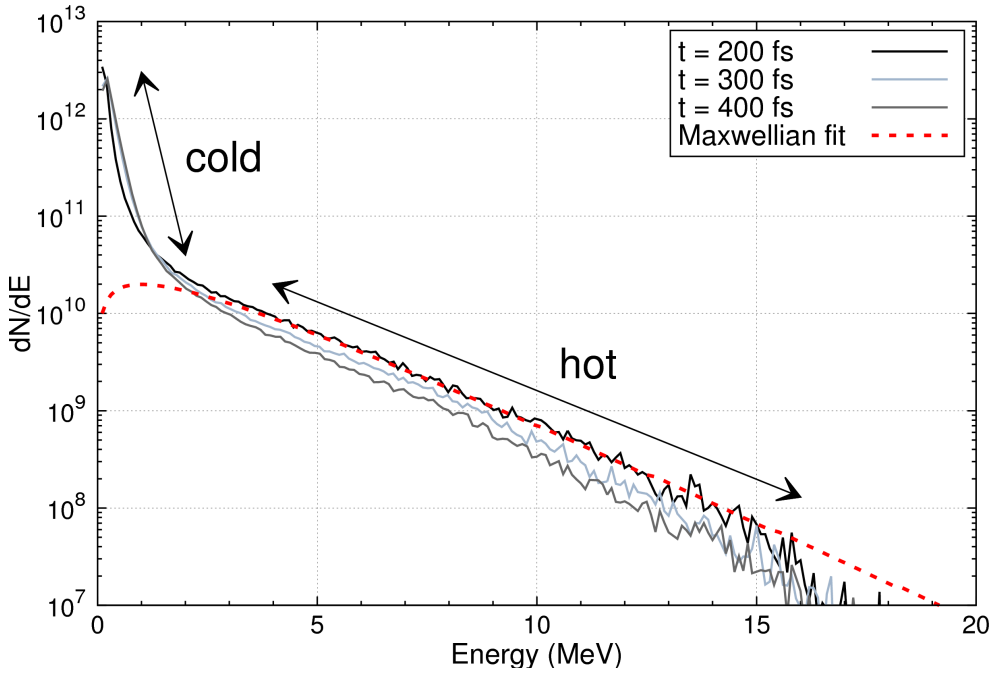

(a) Hot electrons inside simulation system, T_h of 2.1 MeV.

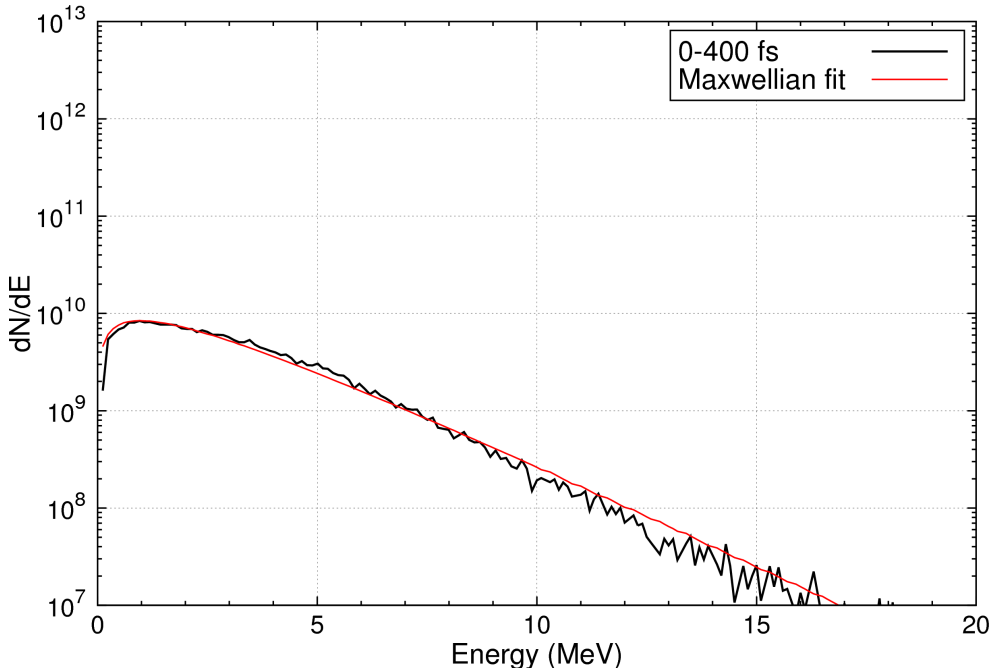

(b) Hot electrons streaming forward out of system, T_h of 2.0 MeV.

Figure 6: Hot electron energy spectra calculated from EPOCH simulations for 10^{20} W cm^{-2}. Fitting to the Maxwellian distribution yields very similar T_h for both spectra (2.1 and 2.0 MeV) and good agreement with the ponderomotive $\mathbf{j} \times \mathbf{B}$ scaling formulas.

The EPOCH-calculated hot electron temperature T_h agrees well with the $I\lambda^2$ ponderomotive $\mathbf{J} \times \mathbf{B}$ scaling formulas found in literature. For example, Wilks *et al.* (1997) gives Equation 16, where $I\lambda^2$ is in units of W-μm^2 cm^{-2} and $m_e c^2$ is the electron rest mass energy of 0.511 MeV.[59] For a laser intensity of 10^{20} W cm^{-2} and wavelength of 0.8 μm, Equation 16 gives a T_h of 2 MeV, which agrees very well with the T_h fitted from the energy spectra.

$$T_h = m_e c^2 \left[-1 + \sqrt{1 + \frac{I\lambda^2}{2.38 \times 10^{18}}} \right] \tag{16}$$

An additional study was performed to confirm that T_h scales also with λ (parameter, $I\lambda^2$), and results again showed good agreement between T_h calculated from EPOCH and T_h from Equation 16. For example, for a laser intensity of 10^{20} W cm^{-2} and wavelength of 0.4 μm, EPOCH simulations found a T_h of 1.2 MeV compared to 1.3 MeV calculated from Equation 16.

Figure 7 plots the hot electron temperature T_h as a function of laser intensity I from EPOCH simulations with λ of 0.8 μm (Ti:sapphire short-pulse laser). The calculated T_h from EPOCH has a standard deviation of about 15% due to using different lower and upper energy bounds when fitting the hot electron spectra. A fit for the calculated hot electron temperatures is also given in Equation 17 as

$$T_h(I) = 1.05 \times 10^{-10} \; I^{0.514} \tag{17}$$

where T_h is in units of MeV and I is in W cm^{-2}. The EPOCH results also agree well with $I\lambda^2$ scaling laws and PIC simulations from work by Wilks *et al.* (1992 & 1997)[59,60] and Kluge *et al.* (2011).[35]

The EPOCH simulations at each laser intensity were calculated for a plasma scale length that resulted in optimal hot electron heating and subsequent bremsstrahlung dose generation. Plasma electrons absorb energy from the laser via various mechanisms such as resonance absorption and ponderomotive heating, which are sensitive

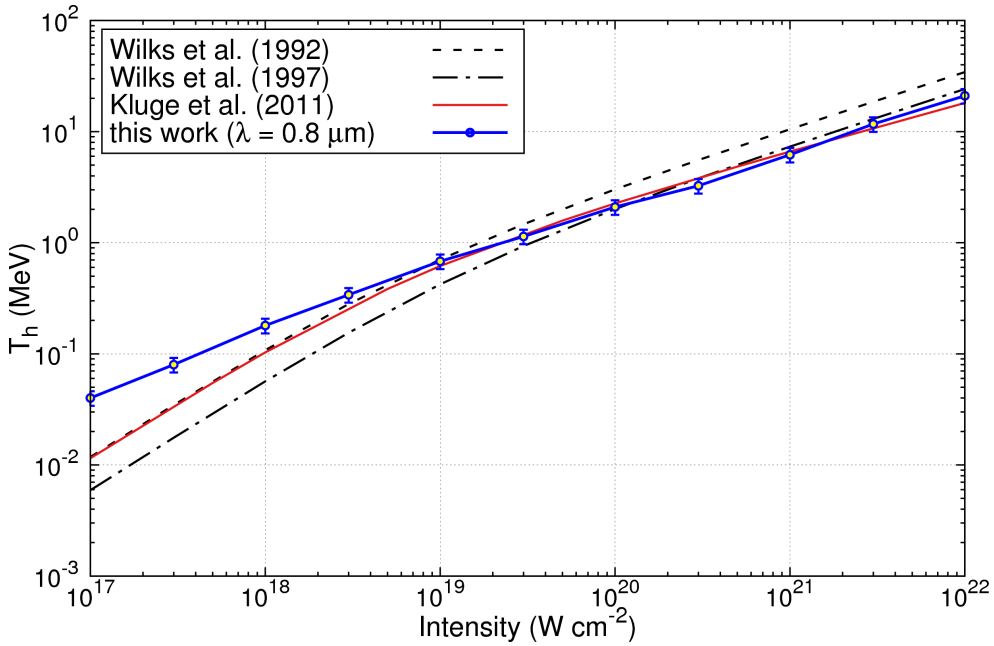

Figure 7: The hot electron temperature T_h calculated in this work with EPOCH scales with laser intensity and agrees well with literature.[59,60,35]

to laser intensity and plasma scale length. Resonance absorption occurs for moderate laser intensities in the range of about 10^{14}–10^{17} W cm^{-2} and for a plasma scale length greater than the laser wavelength ($L_s > \lambda$). Ponderomotive heating dominates at higher laser intensities $I \geq 10^{18}$ W cm^{-2} and for a plasma scale length comparable to the laser wavelength ($L_s \approx \lambda$).[5,44]

As seen in Figure 7, the differences the EPOCH results presented here and the formulas found in literature is because analytical models in literature often account for only one heating mechanism (such as ponderomotive heating). While these analytical models provide good estimates of T_h for $I \geq 10^{18}$ W cm^{-2}, they may underestimate T_h for lower laser intensities where mechanisms such as resonance absorption are more dominant.

PIC codes such as EPOCH do not differentiate between various electron heating mechanisms. Therefore, hot electron heating can be optimized for the highest T_h by adjusting the plasma scale length parameter, L_s. This result was seen in Figure 7 between 10^{17} and 10^{19} W cm^{-2} where the EPOCH simulations gave T_h greater than

values given in literature.

As a demonstration of this tricky concept, EPOCH simulations with an unoptimized plasma scale length (L_s set constant at 1.2 μm) resulted in lower T_h values between 10^{17} and 10^{19} W cm^{-2}, which exactly matches the analytical formulas in literature and is shown in Figure 8. For radiation protection, the hot electron source with the highest T_h (and results in the highest bremsstrahlung dose) at each laser intensity is desired, so T_h from Figure 7 will be used for the remainder of this dissertation.

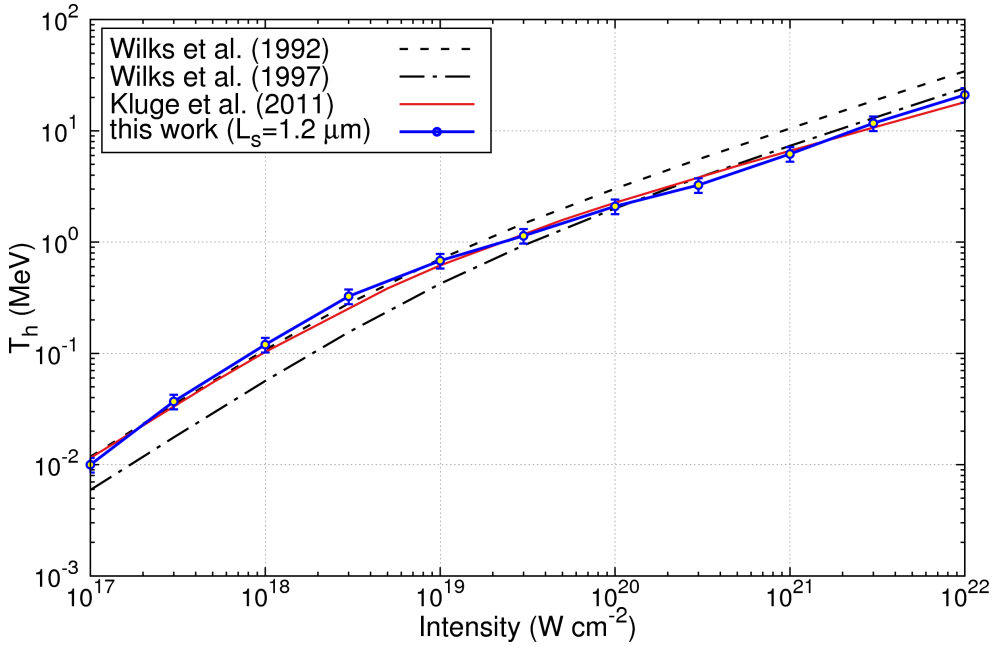

Figure 8: EPOCH simulations with an unoptimized plasma scale length resulted in T_h values that exactly match analytical formulas in literature.

3.3.2 Hot electron angular distribution

During laser-plasma interactions, a population of hot electrons will stream out from the plasma in the upstream (backward) direction and another in the downstream (forward) direction. The angular distributions of both these hot electron populations were derived from the momentum vectors (p_x and p_y) of tracked the tracked hot electrons during the EPOCH simulation. It was found that the Gaussian function in

Equation 18 fit the hot electrons' angular distributions well.

$$f(\theta) \sim \exp\left[-\frac{\theta^2}{2\sigma^2}\right] \tag{18}$$

Figure 9 plots the angular distributions of hot electrons streaming out of the plasma (integrated over the simulation time from 0 to 600 fs) in the forward and backward directions for 10^{20} W cm^{-2}. The parameter σ was fitted to be 49° and 47° for the backward and forward directions, respectively. This agrees well with another PIC study by Sircombe *et al.* (2013) that found the hot electron angular distribution can be fitted with a Gaussian with σ of 40.3° at 6×10^{19} W cm^{-2}.[54]

The angular distributions of hot electrons streaming from the plasma within each 100 fs increment are also plotted to show that the distribution remains consistent over time. Therefore, it can also be assumed that the hot electrons not streaming out (remaining inside simulation) have similar Gaussian angular distributions.

A small reduction in σ or 'narrowing' of the angular distribution was observed with increasing laser intensity from 10^{17} to 10^{22} W cm^{-2} in EPOCH simulations. However, since σ remained consistently within 45°$\pm$ 5° for the intensity range, this reduction is not pronounced enough to significantly affect the angular yield of bremsstrahlung. For the hot electron source term in this dissertation, the angular distributions of hot electrons for intensities between 10^{17} and 10^{22} W cm^{-2} were simply estimated to be Gaussian with a σ of 45°.

As seen in Figure 9, additional information from angular distributions is the ratio of hot electrons emitted in the forward and backward directions (or downstream and upstream from the plasma). This was calculated by taking the ratio between the total energy of hot electrons traveling in the forward direction and those in the backward direction. The forward-to-backward ratio of hot electron yield is plotted in Figure 10 and scales as a function of laser intensity. The data fits well with the power function

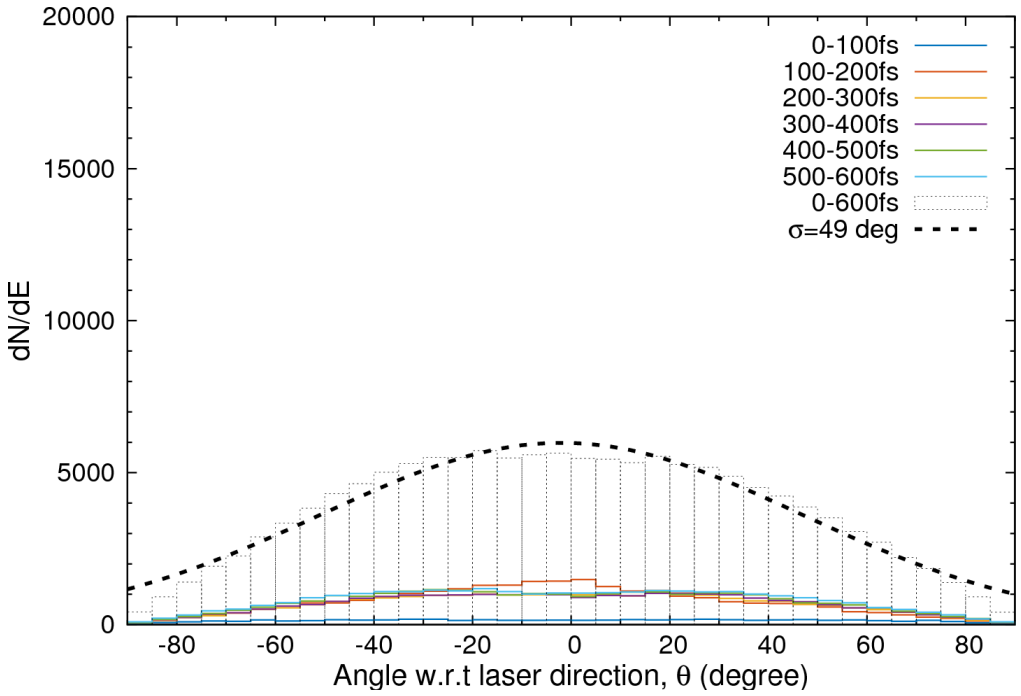

(a) Hot electrons in backward direction for 10^{20} W cm^{-2}.

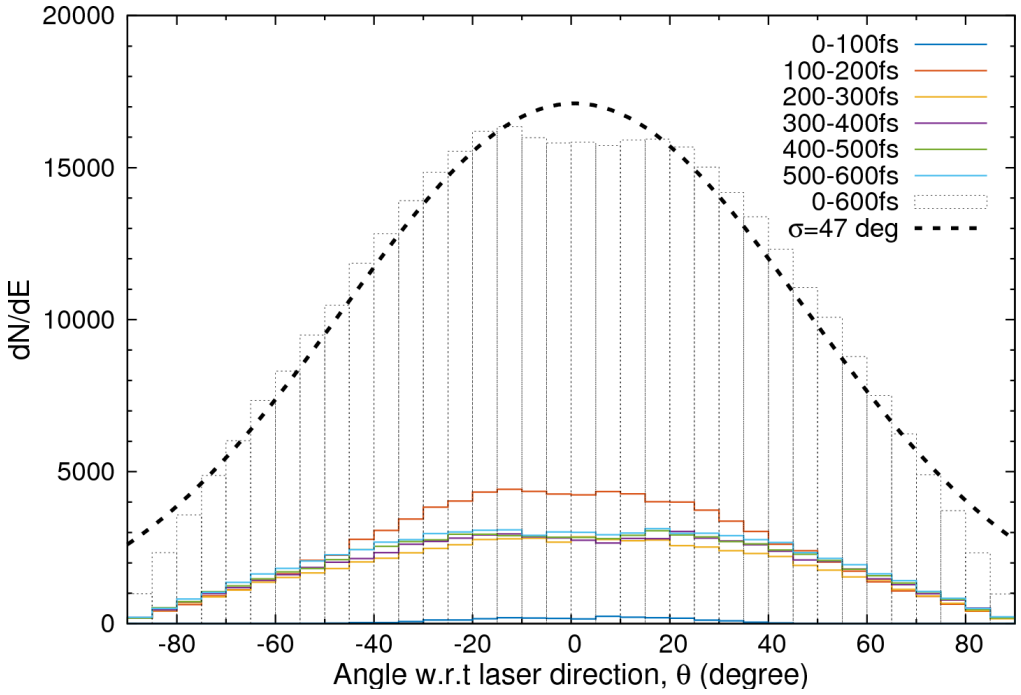

(b) Hot electrons in forward direction for 10^{20} W cm^{-2}

Figure 9: The backward and forward hot electron angular distributions can be fitted with a Gaussian with standard deviation σ: (a) 49° and (b) 47°. A larger population of hot electrons are emitted in the laser's forward direction.

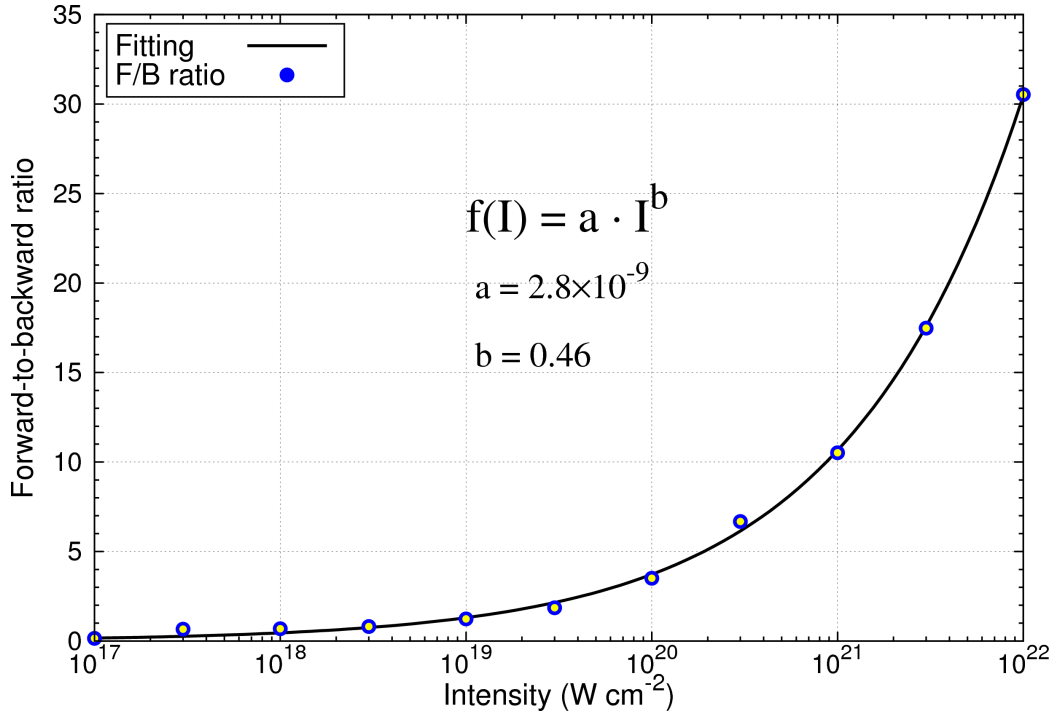

Figure 10: The forward-to-backward ratio of hot electrons as a function of laser intensity from EPOCH simulations. The hot electron emission is increasingly forward-peaked with increasing laser intensity.

in Equation 19 where I is the laser intensity in W cm^{-2}.

$$f(I) = 2.8 \times 10^{-9}\ I^{0.46} \tag{19}$$

As laser intensity increases, the hot electron emission and subsequent bremsstrahlung generated is intuitively increasingly forward-peaked. The forward-to-backward ratio approaches one-to-one between 10^{18} and 10^{19} W cm^{-2}. This does not suggest that the hot electron source is isotropic at these intensities. It only states that the total energy of hot electrons emitted in the forward and backward directions is the same.

3.3.3 Laser-to-electron conversion efficiency

Only a fraction of the laser pulse energy from a high-intensity laser beam is absorbed by the hot electrons in the plasma. Work by Fuchs *et al.* (2006) determined the laser-to-electron conversion efficiency (η) as a function of laser intensity (W cm^{-2}) to

be as given in Equation 20 with a maximum of 50%.[21]

$$\eta = 1.2 \times 10^{-15}\ I^{0.74} \tag{20}$$

Experiments at different facilities have measured laser-to-electron energy conversion efficiencies between 10 and 50% at 10^{20} W cm^{-2}.[33,46,29] For intensities greater than 10^{20} W cm^{-2}, Ping *et al.* (2008) measured conversion efficiencies upwards of 60–90% for different laser incidence angles.[49]

This wide range of reported energy conversion efficiencies in literature led Qiu *et al.* (2011) to develop a simple model of the laser-to-electron conversion efficiency for SLAC's Radiation Protection (RP) group to estimate the bremsstrahlung dose yields from laser-solid experiments. The model conservatively used an η of 30% for laser intensities below 10^{19} W cm^{-2} and 50% above 10^{19} W cm^{-2} for dose calculations.[51]

Calculations in EPOCH improve upon this simple model by taking the ratio between the total energy of all hot electrons and the total laser pulse energy as given in Equation 11 where E_{laser} is the total laser pulse energy and n is the number of macro-particles with weight (w) and energy (E). As a reminder, the weight of a macro-particle in a PIC simulation is the number of physical particles it represents as it is impossible to simulate every single electron due to computational limits.

$$\eta = \frac{1}{E_{\text{laser}}} \sum_{j=1}^{N} n_j \times w_j \times E_j \tag{21}$$

Figure 11 compares the η calculated using EPOCH as a function of laser intensity with the scaling by Fuchs *et al.* (2006) and the radiation protection model proposed by Qiu *et al.* (2011). At lower laser intensities around 10^{17} W cm^{-2}, the previous model was too conservative in estimating an η of 0.3, while at higher laser intensities, the η calculated in this work is higher by about 20%.

Similar to the hot electron temperature T_h, the conversion efficiency will vary depending on the density ramp of the pre-plasma, which is characterized by the plasma scale length L_s (Equation 9). The previous η values correspond to the optimal

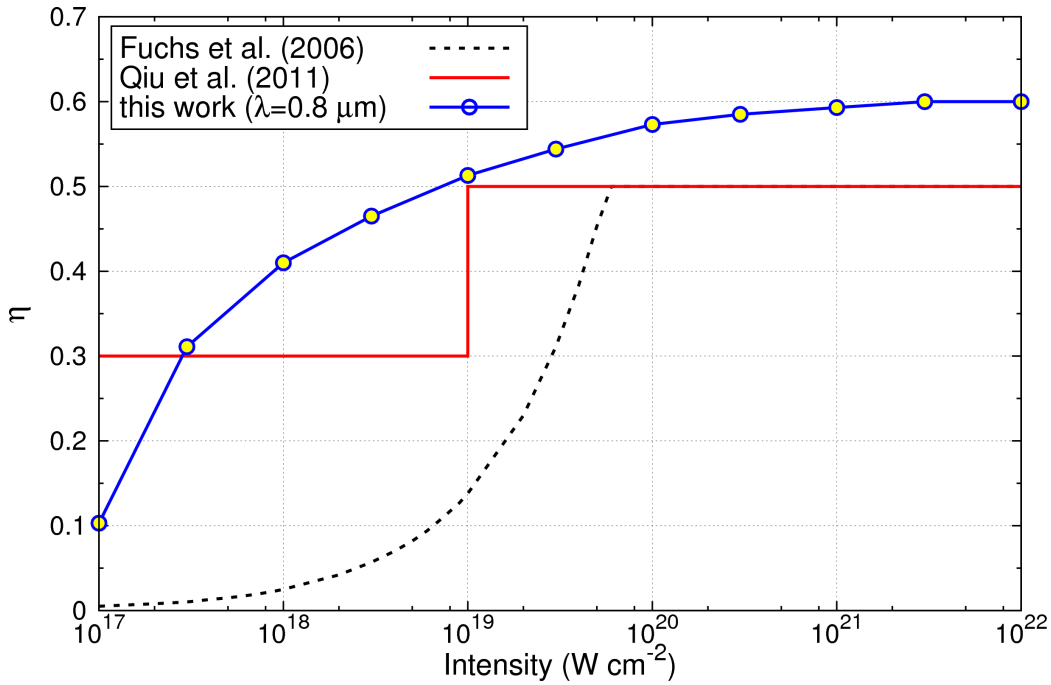

Figure 11: Laser-to-electron energy conversion efficiencies as a function of laser intensity calculated from EPOCH simulations and compared with two other models.[21,51]

T_h from Figure 7. By not optimizing and setting a constant L_s of 1.2 μm, the laser-to-electron heating is less efficient at laser intensities $< 10^{19}$ W cm^{-2} and gives the result shown in Figure 12. The un-optimized η values are lower at laser intensities between 10^{17} and 10^{19} W cm^{-2}, and these laser intensities also correspond with the ones earlier where a non-optimal L_s resulted in lower hot electron temperatures. At higher laser intensities above 10^{19} W cm^{-2}, the optimal L_s was also 1.2 μm, which resulted in the same values.

The conclusion is that the laser-to-electron energy conversion efficiency η is not so easily characterized theoretically or experimentally with one simple model. Nevertheless, from a radiation protection point of view, the EPOCH calculations demonstrated here provide a more reasonable estimation of η below 10^{19} W cm^{-2} (not a step function) and a slightly more conservative estimate at higher laser intensities than previous methods.

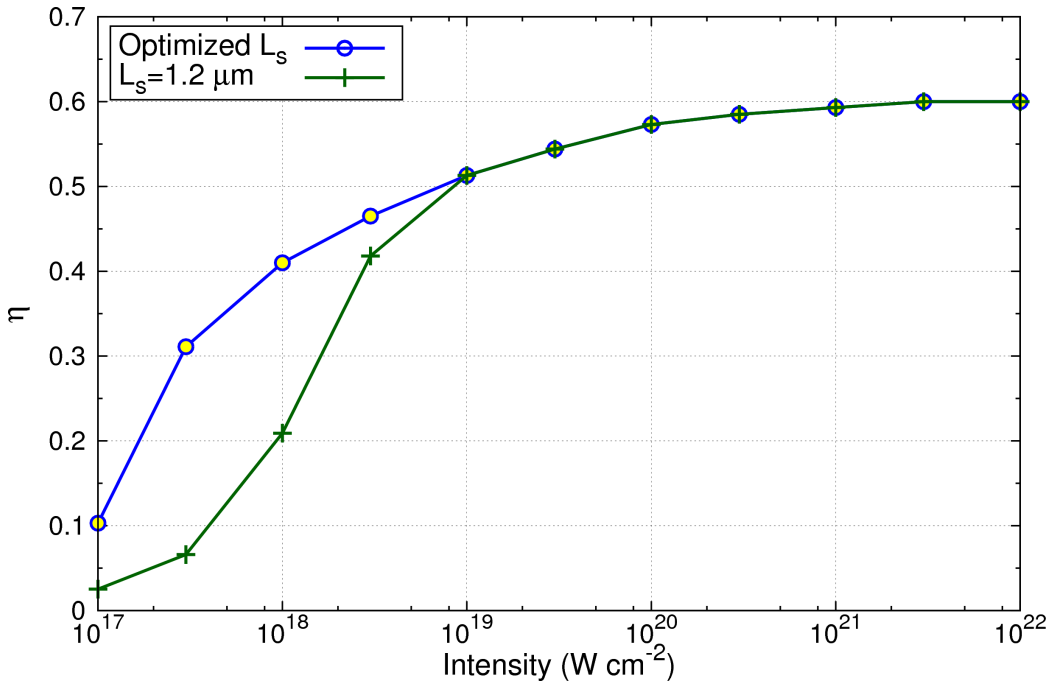

Figure 12: Laser-to-electron energy conversion efficiencies as a function of laser intensity calculated from EPOCH simulations with an optimized plasma scale length L_s and an unoptimized L_s set at 1.2 μm.

3.3.4 Plasma scale length sensitivity study

The plasma scale length initialized in the EPOCH simulation (Figure 13) can affect the heating of the plasma by the laser and the energy of the hot electrons. The earlier sections on the T_h of hot electron energy distribution (Figure 8) and laser-to-electron energy conversion efficiency η (Figure 12) demonstrated the importance of optimizing L_s, especially for laser intensities $< 10^{19}$ W cm^{-2}. The T_h and η that results in the highest bremsstrahlung dose is wanted for radiation protection. A sensitivity study was performed with EPOCH to characterize the effect of plasma scale length L_s on the hot electron temperature T_h and the laser-to-electron conversion efficiency η.

Recall that the scale length L_s of a plasma density ramp is the distance at which the density drops to $^1/_e$ of its peak value (Equation 9). A larger scale length corresponds to a shallow electron density gradient, whereas a smaller one corresponds to

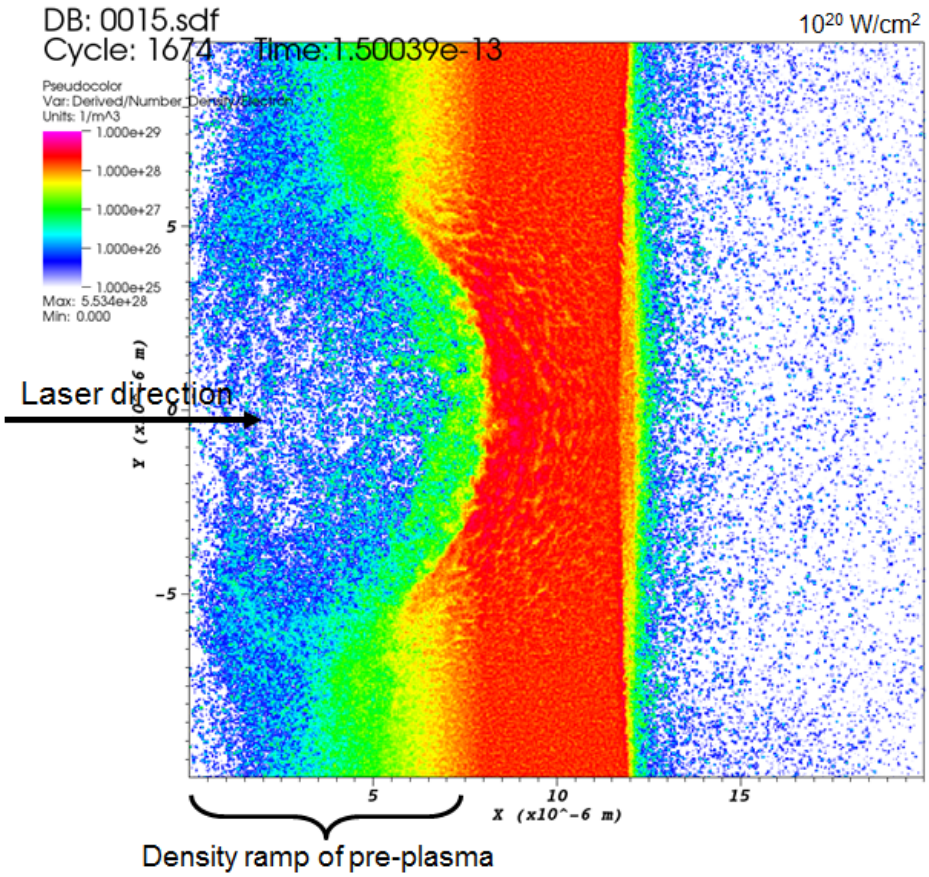

Figure 13: Snapshot of the electron density per unit grid during an EPOCH simulation with a laser intensity of 10^{20} W cm^{-2}. The pre-plasma from 0 to 8 μm is initialized with a plasma scale length L_s from Equation 9.

a steeper one. As seen earlier in Figure 3, this parameter is known to affect the dominant hot electron heating mechanism during laser-solid interactions. One specific example at 10^{19} W cm^{-2} is demonstrated here.

Figure 14 plots the hot electron temperature T_h for an EPOCH simulation with a laser intensity of 10^{19} W cm^{-2} as a function of the plasma scale length given as a ratio (L_s/λ) of the laser wavelength (0.8 μm). Similarly for 10^{19} W cm^{-2}, Figure 15 plots the corresponding laser-to-electron energy conversion efficiencies η for the same plasma scale length ratios. The values of T_h and η can vary significantly depending on L_s.

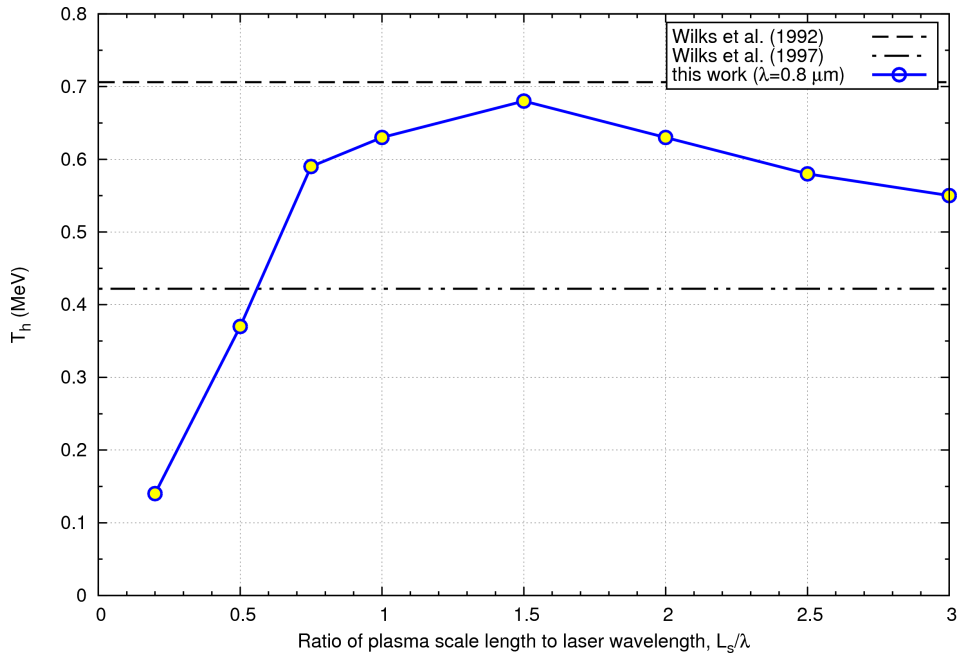

Figure 14: Hot electron temperature as a function of the ratio L_s/λ from EPOCH simulations with a laser intensity of 10^{19} W cm^{-2} and laser wavelength of 0.8 μm. Also provided are two analytical estimation of T_h from literature.[59,60]

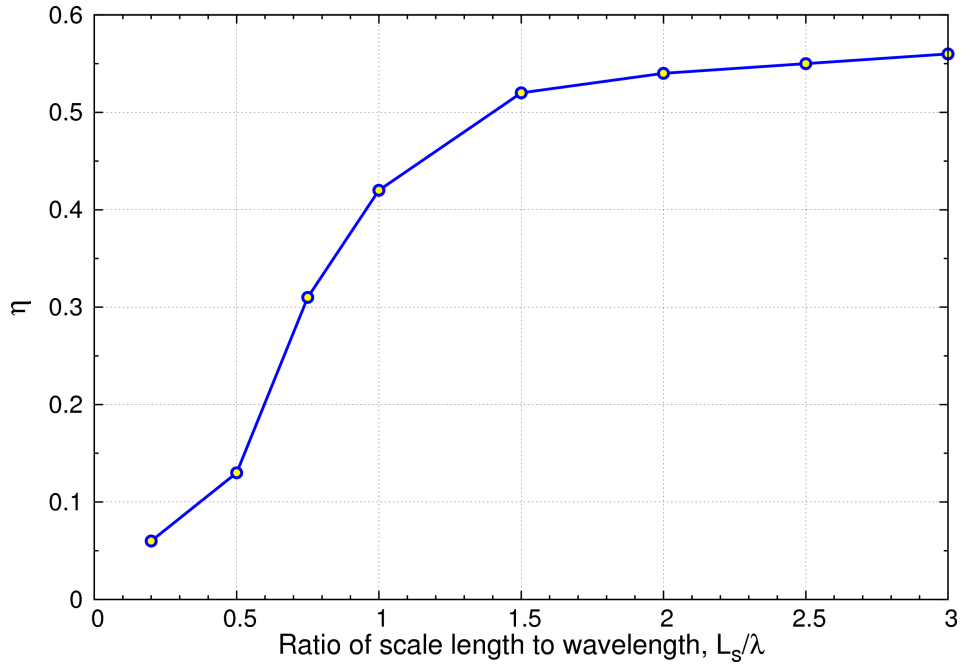

Figure 15: Laser-to-electron conversion efficiency as a function of the ratio L_s/λ from EPOCH simulations with a laser intensity of 10^{19} W cm^{-2} and laser wavelength of 0.8 μm.

From Figure 14, T_h peaks at 0.68 MeV for a L_s/λ ratio of 1.5 and drops to as a low as 0.14 MeV for smaller ratios and 0.55 MeV for higher ratios. Ponderomotive scaling laws from work by Wilks *et al.* (1992, 1997) calculate a T_h of 0.71 and 0.42 MeV for a laser with intensity of 10^{19} W cm^{-2} and wavelength of 0.8 μm. The T_h values calculated in EPOCH are all within this range except for one data point.

In Figure 15, the laser-to-electron energy conversion efficiency η increases as the plasma scale length ratio increases (density gradient grows shallower) from as low as 6% for a ratio of 0.2 and plateauing at about 55% for higher ratios. The η of 0.52 corresponds to the maximum T_h of 0.68 MeV from earlier, so the peak values of T_h and η do not always occur for the same plasma scale length ratio.

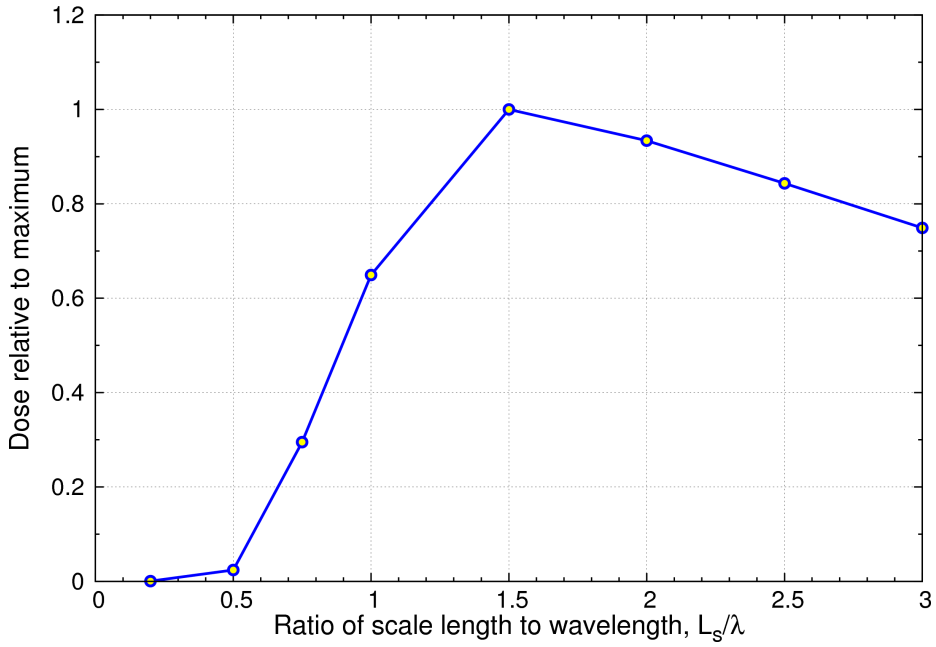

Figure 16: FLUKA calculations show that the maximum bremsstrahlung dose yield occurs at L_s/λ of 1.5 using the EPOCH hot electron source terms from the L_s sensitivity study. For all simulations, the laser intensity was 10^{19} W cm^{-2} with a wavelength of 0.8 μm.

Calculations with the radiation transport code FLUKA were performed to find which hot electron source from Figures 14 and 15 generates the most bremsstrahlung dose yield when interacting with a Cu foil. The results from FLUKA are plotted

in Figure 16 where the Y-axis is the generated bremsstrahlung dose yield relative to the maximum. For a laser with intensity of 10^{19} W cm^{-2}, the peak bremsstrahlung yield occurs at L_s/λ of 1.5 where T_h was the maximum even though η was not at its highest value. The 'hardness' of hot electron source's energy spectrum (Maxwellian with slope of T_h) contributes more to the yield of bremsstrahlung photons than the laser-to-electron energy conversion efficiency (η).

All previously shown results for the hot electron source term in this chapter were calculated for plasma scale lengths that yielded the optimal hot electron heating and also resulted in optimal bremsstrahlung dose generation at each laser intensity. For radiation protection, this provides a conservative hot electron source term when performing bremsstrahlung dose yield calculations.

CHAPTER IV

CALCULATION OF BREMSSTRAHLUNG DOSE YIELD FROM HOT ELECTRONS

4.1 FLUKA: radiation transport and interaction code

FLUKA is a Monte Carlo radiation transport and interaction code that has modern physics models for about sixty different types of particles. The code can simulate particle propagation, interaction, and generation in matter. Furthermore, the FLUKA input supports combinatorial geometry and allows for the simulation of complex geometries such as the MEC target vacuum chamber in Figure 17. For the purposes of this dissertation, FLUKA was used to perform the generation of bremsstrahlung photons from a hot electron source term (results from EPOCH) interacting with the target material or target chamber wall and to subsequently calculate the ambient dose equivalent of bremsstrahlung photons.

FLUKA uses an original transport algorithm for charged particles (such as electrons) with complete multiple Coulomb scattering treatment, and variations with energy of the discrete event cross-sections and of the continuous energy loss in each transport step are taken into account exactly.[18] Differences in the transport of electrons and positrons are also taken into account with regards to both stopping power and bremsstrahlung generation.[34] FLUKA uses bremsstrahlung differential cross sections from Seltzer and Berger,[52,53] and the angular distribution of bremsstrahlung photons is sampled accurately.

In this study, the bremsstrahlung dose yield (mSv J^{-1}) from laser-solid interactions is defined in this dissertation as the ambient dose equivalent (mSv) of bremsstrahlung photons from hot electrons normalized to the laser pulse energy (J) on target.[10,17]

The bremsstrahlung dose yield is the key parameter for estimating ionizing radiation hazard and will be related to laser-optics parameters via laser intensity (W cm^{-2}).

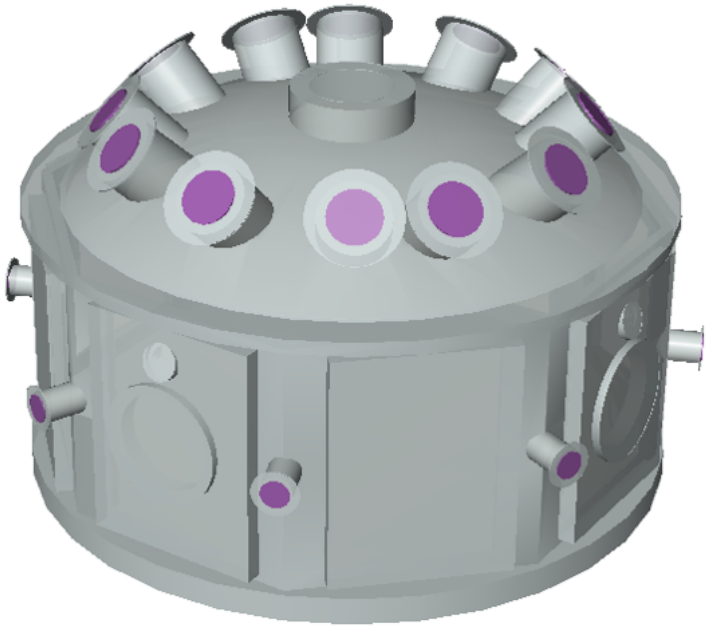

Figure 17: The fully simulated 3D geometry in FLUKA of the target vacuum chamber located at the MEC laser facility at SLAC. The target chamber has a radius of 1 m and aluminum walls with about 2.54 cm thickness. During an experiment, the large number of viewports around the outside give the experimenters' instruments access to the laser-matter interactions taking place within the vacuum chamber.

4.1.1 FLUKA methodology

The geometry for FLUKA simulations consisted of a 2 cm × 2 cm Cu foil (common 'medium-Z' target for laser-solid experiments) with thickness equal to one continuous-slowing-down approximation (CSDA) range for an electron with energy of $1.5 \times T_h$, which is the mean energy of the Maxwellian distribution from Equation 11. The CSDA range is a very close approximation of the average path length traveled by a charged particle (electron) as it slows down to rest in a medium (Cu).

The Cu foil was located inside vacuum at the center of a target chamber with an

Al wall thickness of 2.54 cm Al and a radius of 1 meter. High-intensity laser interactions with solid targets is a micron-scale surface effect, so the hot electrons were emitted 10 μm inside the Cu foil. The ambient dose equivalent (mSv) of bremsstrahlung photons from hot electrons interacting with the Cu and Al chamber wall was calculated outside the target chamber.

As a reminder, the hot electron source term as a function of laser intensity was determined in the previous chapter with EPOCH: Maxwellian energy distribution starting with temperature T_h (Figure 7), Gaussian angular distribution with σ of 45° (Figure 9), and forward-to-backward ratio (Figure 10). Dose calculations in FLUKA were normalized with the laser-to-electron energy conversion efficiency η (Figure 11). An example of the FLUKA input code used in this dissertation is provided in Appendix B.

4.2 Bremsstrahlung dose yield from hot electrons

FLUKA used the hot electron source term determined by EPOCH to calculate the bremsstrahlung dose yield for high-intensity laser-solid interactions. The bremsstrahlung dose yield at 1 meter (mSv J^{-1}) is calculated as a function of laser intensity and is defined as the ambient dose equivalent (mSv) of bremsstrahlung photons from hot electrons normalized to the laser pulse energy (J) on target. The bremsstrahlung dose yield is also given as a function of angle: 0°, 45°, 90°, and 180°. Systematic calculations in FLUKA covered the laser intensity range between 10^{17} and 10^{22} W cm^{-2}.

4.2.1 Sensitivity of bremsstrahlung dose yield to target parameters

Experiments with high-intensity laser beams utilize a wide assortment of target materials with varying thicknesses. Depending on the experiments' scientific interests, targets can range from low-Z plastics up to high-Z metal foils such as Au and Ta. Furthermore, foil thicknesses can span several orders of magnitude from micrometers to millimeters. Therefore, a target sensitivity study was performed with FLUKA to

characterize how the laser target's Z and thickness affect the bremsstrahlung dose yield. A wide variety of target types were chosen for the study: Mylar (plastic with Z_{eff} of ~6.7), Al (metal with low-Z of 13), Cu (metal with mid-Z of 29), and Ta (metal with high-Z of 73).

Figure 18 plots the effect of Z and material thickness in cm on the bremsstrahlung dose yield generated from hot electrons interacting with the target for a laser intensity of 10^{20} W cm^{-2}. For each data point, FLUKA calculated the ambient dose equivalent of photons at 1 m in the 0° direction relative to laser axis. The ratios of these bremsstrahlung doses to the maximum value for Cu (common medium-Z target) were calculated for easy comparison. The maximum bremsstrahlung dose from a Cu target for 10^{20} W cm^{-2} occurs at 2.5 mm, which is used as the 'reference' dose yield for this target sensitivity study. For example from Figure 18, the peak dose yield from an Al target occurs at 7.3 mm and is a factor of 0.6 lower than the reference Cu dose yield.

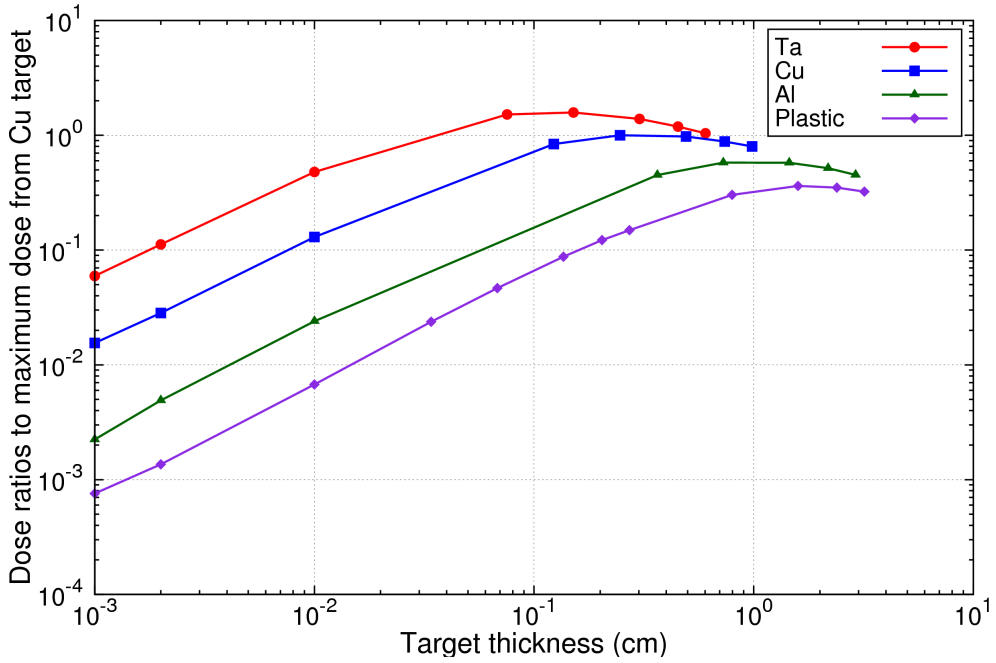

Figure 18: Ratio of bremsstrahlung dose yields generated from hot electrons interacting with the target itself for a laser intensity of 10^{20} W cm^{-2}.

The bremsstrahlung dose yield between different materials scales approximately with $\sqrt{Z}$, and as expected, the Ta target gives the highest dose yield due to its high Z number. In Figure 18, the highest bremsstrahlung dose yields occur for the targets at different thicknesses: 1.5 mm Ta, 2.5 mm Cu, 7.3 mm Al, and 8 mm plastic for laser intensity of 10^{20} W cm^{-2}. For increasing target thicknesses, the dose yields begin to decrease due to self-shielding of the bremsstrahlung by the target itself. The thicknesses that give the highest bremsstrahlung yield all correspond to about 1×CSDA (continuous-slowing-down approximation) range in each material of an electron with energy equal to the average energy of the Maxwellian hot electron distribution. For example, the average energy of the Maxwellian energy distribution for 10^{20} W cm^{-2} is $1.5 \times T_h$ or 1.5×2.1 MeV (3.15 MeV). From the National Institute of Standards and Technology's (NIST) ESTAR database, an electron with energy of 3.15 MeV gives a CSDA range in Cu of about 2.2 mm.[9] The CSDA range is a very close approximation of the average path length traveled by a charged particle as it slows down to rest in a material.

Laser-solid experiments (such as ones at MEC) sometimes use foils from 10 to 20 μm. However, if the target is very thin, many hot electrons will penetrate the target and generate bremsstrahlung with the chamber wall downstream (1 m away from target location for the MEC target chamber). Figure 19 plots the FLUKA-calculated bremsstrahlung dose yields normalized to a distance of 1 m (from the hot electron source location) generated by hot electrons escaping the target material and interacting with a 2.54 cm-thick Al chamber wall located at 1 m from the center of the target chamber. In contrast to Figure 18, bremsstrahlung dose from the Al wall is higher for low-Z materials. Low-Z targets are less effective in attenuating hot electrons than high-Z targets, so more hot electrons escape the target and generate bremsstrahlung at the Al wall.

There is a trade-off between the bremsstrahlung dose yields generated from the

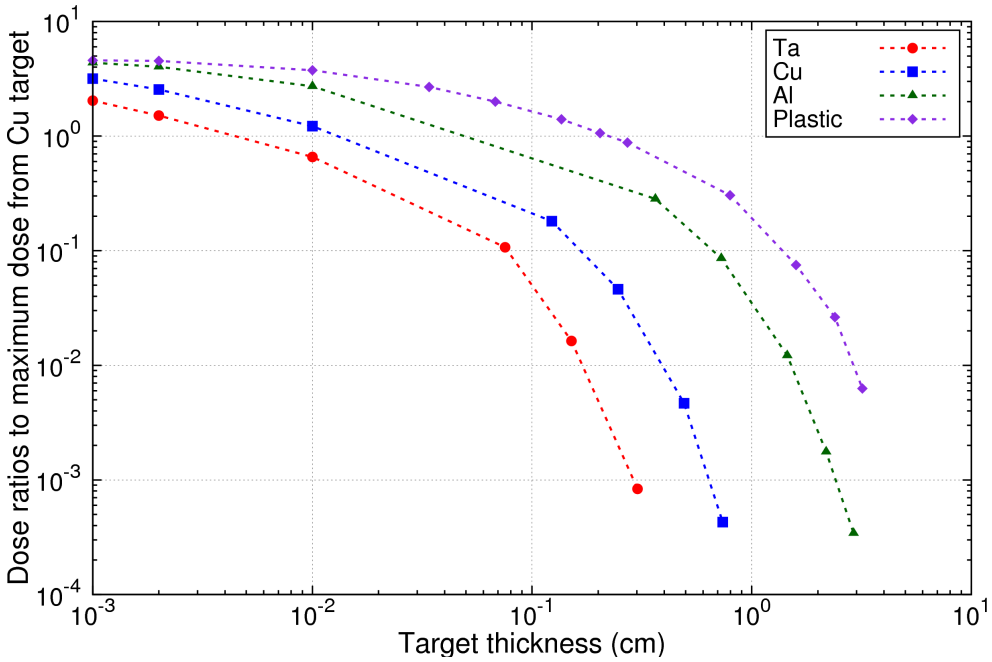

Figure 19: Ratio of bremsstrahlung dose yields generated from hot electrons escaping the target and interacting with the Al target chamber wall. Ratio of bremsstrahlung dose yields from chamber wall for a laser intensity of 10^{20} W cm^{-2}.

target and from the Al chamber wall. The dose yields from the target decrease with thinner targets because hot electrons are escaping with less and less interactions. On the other hand, the dose yields from the wall increase because the hot electrons are now interacting with the chamber wall. Depending on the dimensions of the target chamber, the dose outside the target chamber may actually increase for very thin targets because the primary location of bremsstrahlung generation is at the chamber wall itself and closer to the outside environment where personnel could be.

For example, the bremsstrahlung dose yield from the Cu target itself with thickness of 10^{-3} cm (or 10 μm) decreases by a factor of $^1/_{100}$ from its peak value at 2.5 mm, but the dose yield outside the target chamber increases by a factor of about 2–3 because bremsstrahlung is now generated closer to outside the target chamber. Additional FLUKA calculations characterized the target sensitivity for other laser intensities between 10^{17} and 10^{22} W cm^{-2}, and the conclusions are similar to the example presented here for 10^{20} W cm^{-2}. For calculations of bremsstrahlung source

term from laser-solid interactions in future sections of this dissertation, a Cu target with thickness of 1×CSDA range corresponding to each laser intensity is used to give the highest bremsstrahlung dose yield from the target. For different target types, the dose yield can be scaled with $\sqrt{Z_{\text{solid}}}/\sqrt{Z_{\text{Cu}}}$.

4.2.2 Components of bremsstrahlung source term

Hot electrons will generate bremsstrahlung photons when they interact with the target material at the center of the chamber. Some hot electrons such as the ones in the high energy tail of the Maxwellian spectrum will escape the target, interact with the target chamber wall, and generate additional bremsstrahlung. This scenario will occur for both the forward and backward streaming hot electrons as characterized earlier with EPOCH. The sum of all these components together is the bremsstrahlung source term for high-intensity laser-solid interactions.

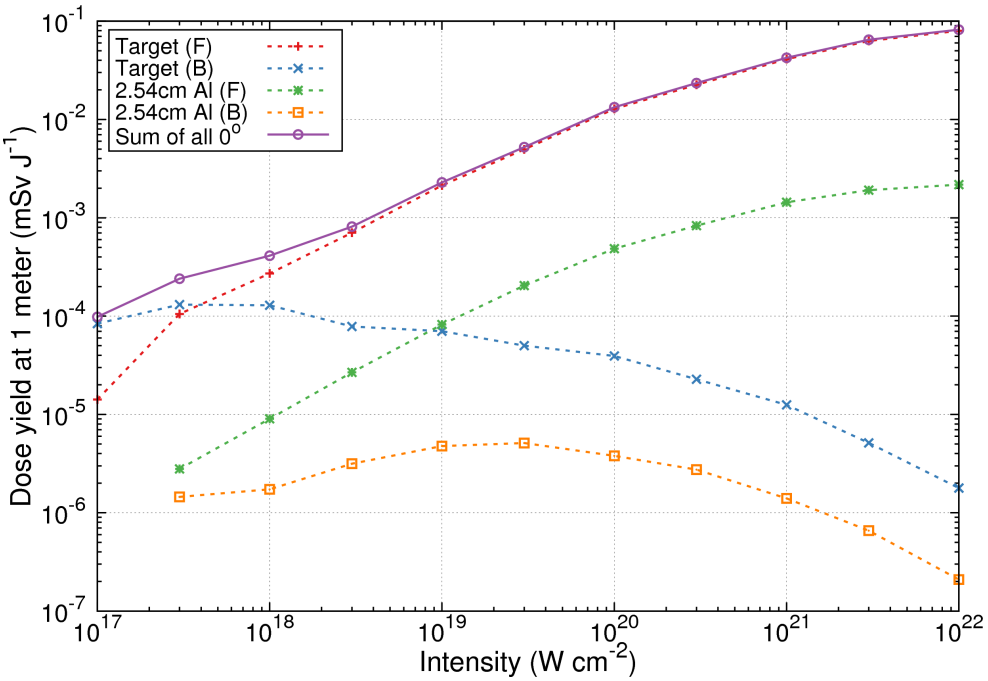

Figure 20: 0° bremsstrahlung dose yield components at 1 meter as a function of laser intensity.

The forward and backward cones of hot electrons will produce bremsstrahlung anisotropically in 4π. Figure 20 gives the components of the bremsstrahlung dose yield in the 0° (forward) direction relative to the laser direction, which were calculated with FLUKA using EPOCH's hot electron source terms at each laser intensity.

In the legend, (F) and (B) indicate dose yields from the forward and backward hot electrons, respectively. The 'Target' label indicates the bremsstrahlung dose was generated from hot electrons interacting with a 1×CSDA Cu foil (corresponding to $1.5 \times T_h$ for each laser intensity). The '2.54 cm Al' label is the bremsstrahlung dose generated from hot electrons that escape the target and that inevitably interact with a target chamber wall with an assumed thickness of 2.54 cm Al. Similarly, Figures 21 and 22 plot the bremsstrahlung dose yield components at 1 m in the 90° (lateral) and 180° (backward) directions.

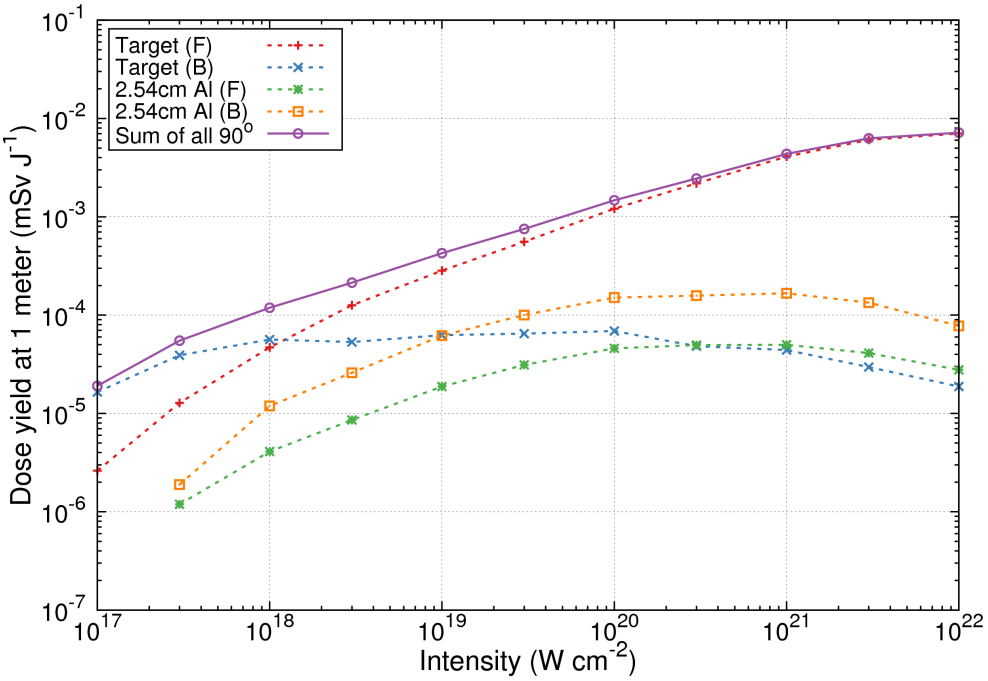

Figure 21: 90° bremsstrahlung dose yield components at 1 meter as a function of laser intensity.

The dominant source of bremsstrahlung for the 0° direction in Figure 20 is from forward hot electrons and the Cu target, except at laser intensities below 10^{18} W cm^{-2},

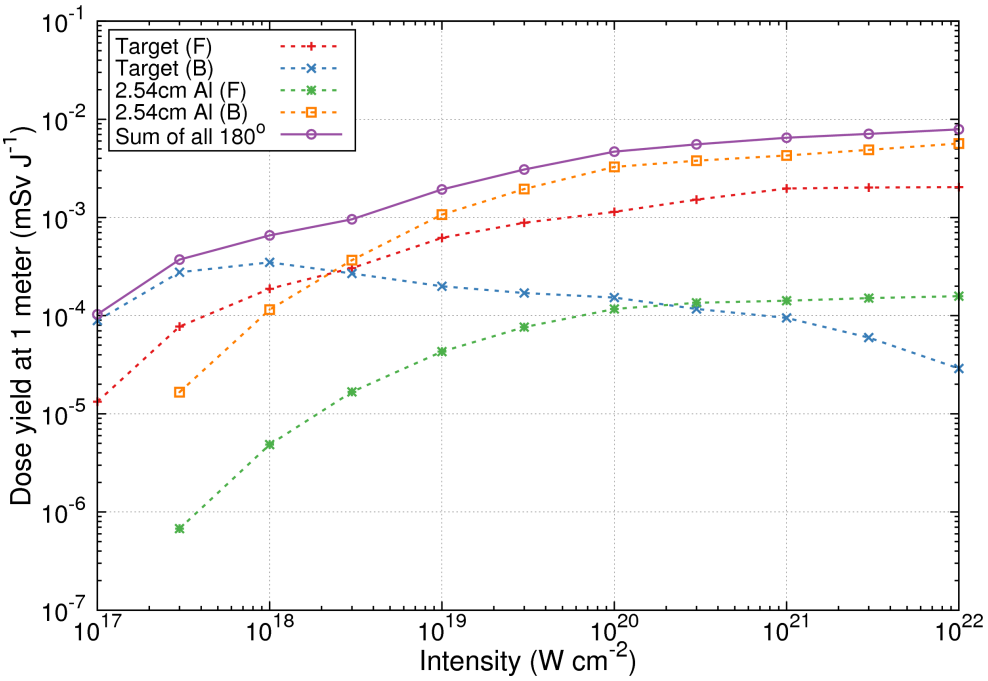

Figure 22: 180° bremsstrahlung dose yield components at 1 meter as a function of laser intensity.

where the backscatter from backward hot electrons is dominant. This is because at lower intensities, the hot electron yield is greater in the backwards direction as shown earlier in Figure 10. The 0° bremsstrahlung generated from the Al wall are at least an order of magnitude lower than from the target.

Unlike the 0° dose yield, the 180° dose yield in Figure 22 is mostly from backward hot electrons that escape the Cu target and interact with the 2.54 cm Al wall. In the FLUKA calculations, backward hot electrons are simulated just inside the backside of the Cu at 10 μm, so a large fraction of the hot electrons in the Maxwellian distribution will interact with the Al wall and generate bremsstrahlung because their CSDA range in Cu is greater than 10 μm.

The 90° dose yield in Figure 21 is dominated by side-scattered bremsstrahlung from forward hot electrons interacting with the Cu target. Similar to the case for the 0° dose yield, the backward hot electrons contribute more to the dose at 90° below about 10^{18} W cm^{-2}. These bremsstrahlung dose yield curves in the 0°, 90°,

and 180° directions represent the bremsstrahlung source term for high-intensity laser-solid interactions.

4.2.3 Bremsstrahlung dose yield from laser-solid interactions

The previous radiation protection model at SLAC for estimating the bremsstrahlung dose yields from laser-solid interactions was based on work by Qiu *et al.* (2011) who expanded the model developed by Hayashi *et al.* (2006) to include laser intensities below 10^{19} W cm^{-2}. Both used conservative assumptions for the hot electron source term to perform dose calculations.[51,30]

Figure 23 plots the 0° models previously used at SLAC for estimating the bremsstrahlung dose yield from laser-solid interactions. The Qiu model (adjusted) also applied factors of $1/3$ at 10^{19} W cm^{-2} and $1/10$ at $> 10^{20}$ W cm^{-2} after radiation measurements at SLAC's MEC and Lawrence Livermore National Laboratory's (LLNL) Titan laser facilities suggested the work performed by Hayashi was too conservative. Additional information on the previous radiation protection models are detailed in elsewhere.[51,6,7,41,40] Comparison of these previous models is also made to the 0° bremsstrahlung source term (developed from EPOCH and FLUKA calculations) from the previous section.

The 0° bremsstrahlung dose yield curve from this work is between a factor of 3 to 10 lower than the Qiu model (adjusted) at laser intensities greater than 10^{19} W cm^{-2}. It intersects the previously developed adjusted model at about 10^{18} W cm^{-2} and is about a factor of 2 greater at 10^{17} W cm^{-2}. The revised model is much smoother than the previous models because no 'sharp' changes or jumps occur in the source term as before.[51] The curve also appears to follow the gradual increase commonly seen in bremsstrahlung radiation yield curves as a function of electron energy.

The bremsstrahlung dose yield calculated in this work is lower than the previous

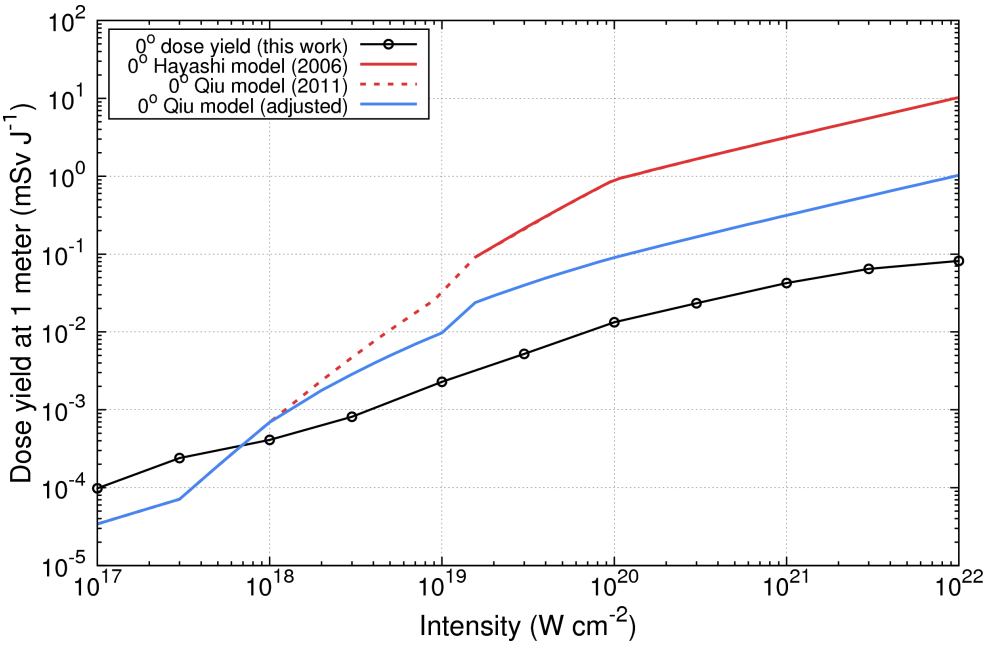

Figure 23: All dose yield models are unshielded and for the 0° direction at 1 meter.

models at the higher laser intensities due to not using several conservative assumptions. The Hayashi and Qiu models assumed a relativistic Maxwellian energy distribution for the hot electrons with a mean energy of $3 \times T_h$, which is a harder energy spectrum than the Maxwellian distribution ($1.5 \times T_h$). Recall, the Maxwellian distribution was used to fit EPOCH's hot electron energy spectrum in this dissertation. The previous models assumed the hot electrons are emitted as a pencil beam, but in reality the hot electrons have an angular distribution and are emitted an-isotropically in 4π. Furthermore, the previous models used a Ta target for bremsstrahlung generation (higher yield than Cu used in this work). The work in this dissertation addresses these conservative assumptions with EPOCH simulations of laser-plasma interactions and several sensitivity studies.

Figure 24 plots the sum of bremsstrahlung source terms in the 0°, 45°, 90°, and 180° directions from the previous section as a function of laser intensity between 10^{17} to 10^{22} W cm^{-2}. These curves were calculated from FLUKA using EPOCH's hot electron source term for estimating the bremsstrahlung dose yield (mSv J^{-1})

generated from laser-solid interactions. For radiation protection design, the maximum dose yield (typically occurs at 0°) is recommended because laser optics can direct the path of the beam in any direction.

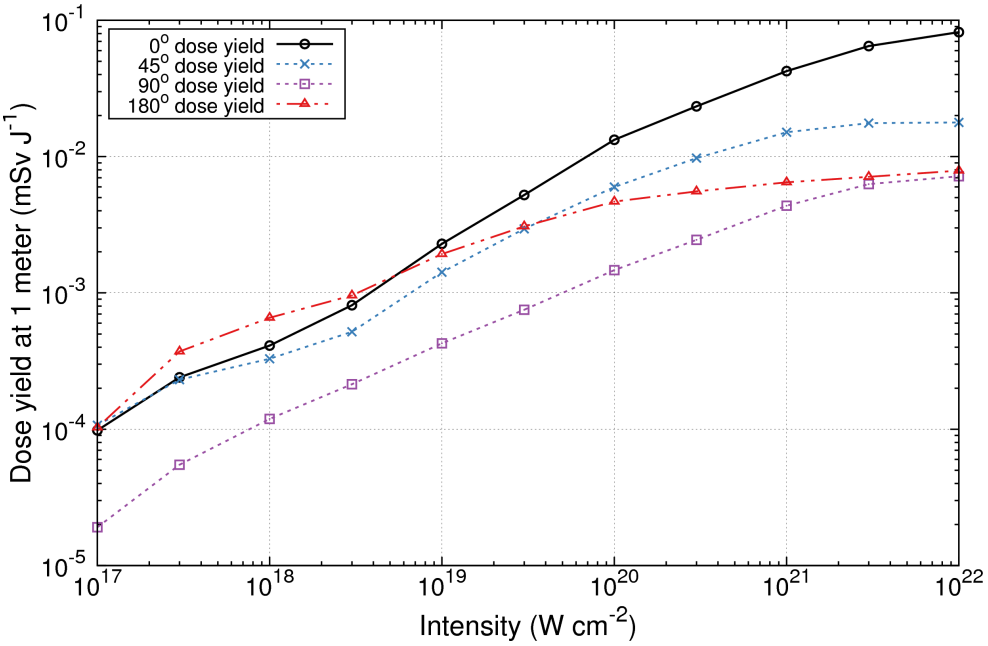

Figure 24: Bremsstrahlung source terms for laser-solid interactions calculated in FLUKA from EPOCH's hot electron source term for 0°, 45°, 90°, and 180° relative to the laser axis.

The dose yield in the 90° direction is consistently about a factor of $^1/_{10}$ compared to the combined dose yields in the 0° and 180° directions (both forward and backward hot electrons contribute to bremsstrahlung in 90°). The dose yield in the 45° direction relative to the laser axis is less than in the 0° at high intensities and converges at low intensities as the bremsstrahlung yield becomes more isotropic.

The dose yield at 1 m in the 180° backward direction is a factor $^1/_{10}$ of the forward 0° direction at laser intensities greater than 10^{20} W cm^{-2}. At 10^{19} W cm^{-2}, the difference is about a factor of 3. At laser intensities around 10^{17} W cm^{-2}, the ratio is one-to-one, which implies the bremsstrahlung dose yield is more isotropic. However, as the laser intensity continues to increase, the dose yield becomes more forward peaked in the 0° direction.

The attenuation of the target chamber needs to be applied to the bremsstrahlung dose yields generated from hot electrons interacting with the target in order to compare to measurement data. Bremsstrahlung dose generated from hot electrons interacting with the an Al wall of thickness of 2.54 cm Al has already accounted for this attenuation. The Al target chamber at MEC laser facility has an approximate wall thickness of 2.54 cm Al. The attenuation factors of 2.54 cm Al for the full range of laser intensities was calculated in FLUKA using the hot electron source term from EPOCH and are plotted in Figure 25.

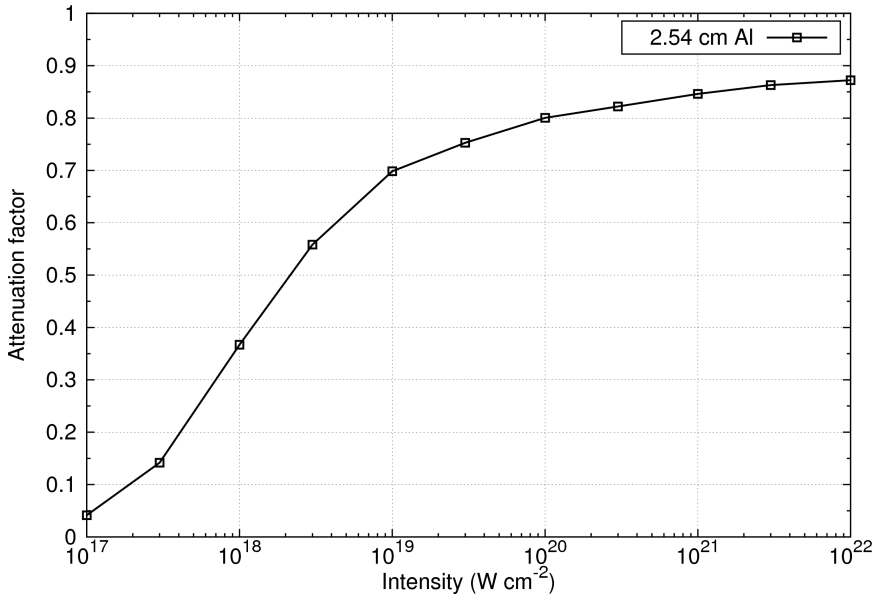

Figure 25: Attenuation factors of 2.54 cm Al for photons generated by a hot electron source term as a function of laser intensity.

With these Al attenuation factors and Figure 24, one can estimate the bremsstrahlung dose yield outside the the target chamber. Figure 26 plots the bremsstrahlung source terms from earlier but now with 2.54 cm of Al shielding from target chamber attenuation. The 2.54 cm Al of the target chamber attenuates the dose yield more at lower laser intensities because the bremsstrahlung energy spectra are softer. Conversely, the attenuation from 2.54 cm Al is increasingly less (and almost negligible) at laser intensities intensities $> 10^{20}$ W cm^{-2}.

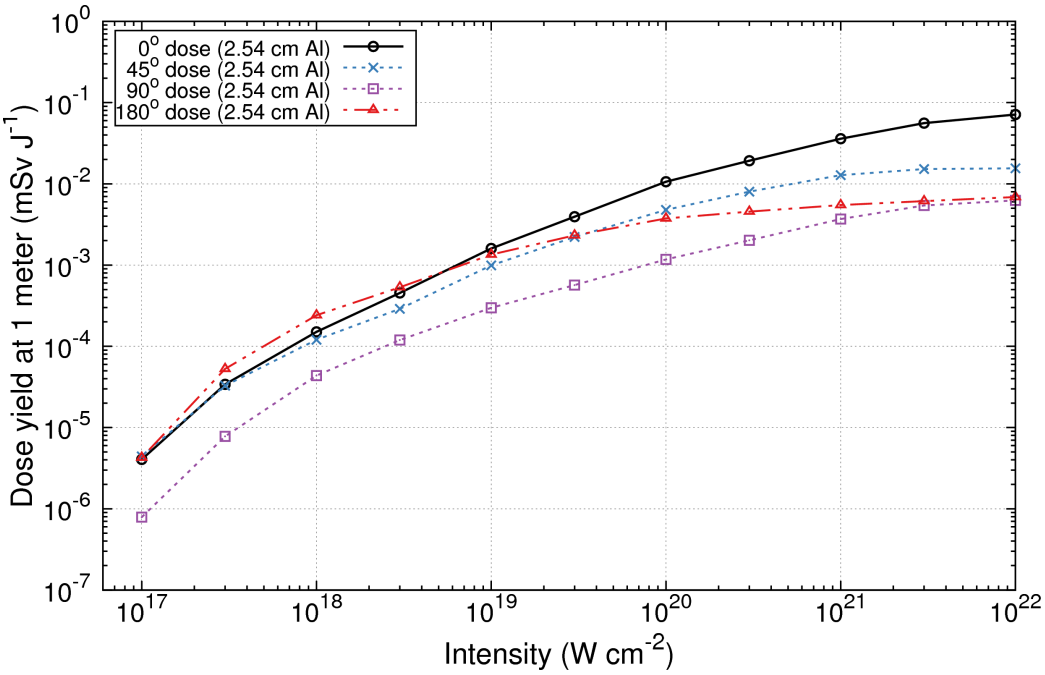

Figure 26: Bremsstrahlung source terms with 2.54 cm Al attenuation factors for laser-solid interactions calculated in FLUKA from EPOCH's hot electron source term for 0°, 45°, 90°, and 180° relative to the laser axis.

The SLAC RP group performed a series of radiation measurements during several high-intensity laser-solid experiments at MEC and one at LLNL's Titan laser facility. The measurement data are plotted in Figure 27 and compared to the bremsstrahlung dose yield curves. Uncertainties in the measurement data for the experiments at SLAC's MEC between 2012 and 2014 are not shown to limit the visual clutter and allow easier comparison to the dose yield curves. The measurement data and error analysis performed during the course of the dissertation and are detailed in the next chapter.[40] The measurements at MEC in 2012 and at Titan are detailed by Bauer *et al.* in literature.[7,6].

The bremsstrahlung dose yield curves in this work in Figure 27 agree well with the trend of the measurement data, especially from about 10^{18} to 10^{20} W cm^{-2}. It is important to understand that the bremsstrahlung dose yield is calculated from EPOCH and FLUKA simulations that use optimal parameters and may not exactly

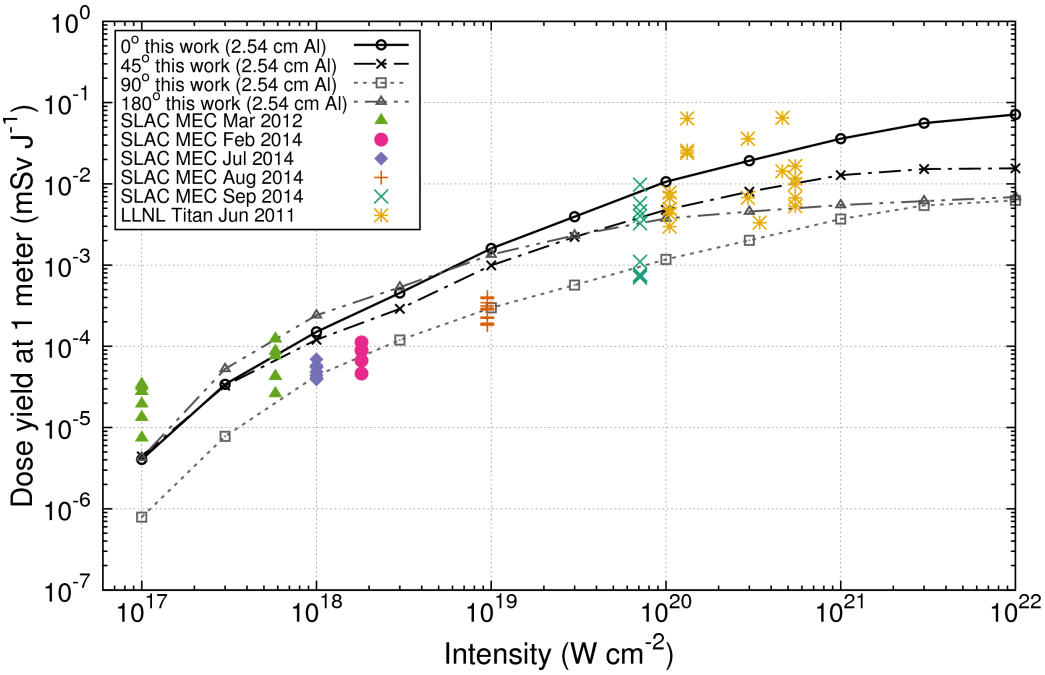

Figure 27: The bremsstrahlung dose yield curves with 2.54 cm Al attenuation from EPOCH and FLUKA calculations agree well with measurement data from SLAC's MEC and LLNL's Titan laser facilities. The measurements were taken outside the target chamber at varying angles and elevation (hence, the vertical spread). Differences between the model and measurements are due to target chamber attenuation, measurement angle, target Z, target thickness, detector sensitivity, and uncertainties in the laser beam characterization.

replicate measurements results. The model does not account for realistic effects of uneven target chamber attenuation, measurement angle, target thickness, detector sensitivity, and uncertainties in the laser beam characterization.

For example, the data at 10^{17} W cm^{-2} in Figure 27 is greater than the curve due to uncertainties in the laser energy on target. For the same measured dose, less energy on target results in a higher dose yield (mSv per J). In addition, the highest dose yields were measured outside the target chamber's 5 mm-thick glass viewports (less attenuation than from 2.54 cm Al).[6]

At laser intensities above 10^{20} W cm^{-2}, some data points from the Titan experiment are greater than the 0° curve, while other points are just at or below. The data from the Titan laser facility were acquired parasitically to another experiment,

meaning the laser and optics parameters were not controlled by the SLAC measurement team, and there was large uncertainty in the laser pulse energy on target in the range of about 50–400 J.[7] Another factor that may have contributed to higher dose yields was the use of Au foils ($Z = 79$), which will have higher bremsstrahlung yield by about a factor of 2 greater than the Cu foils ($Z = 29$).

The bremsstrahlung dose yield curves in this section calculated from FLUKA and EPOCH provide a guideline for radiation hazard analysis for laser-solid interactions between 10^{17} and 10^{22} W cm^{-2}.

4.2.4 Cold electron overestimate

The hot electron source term is implemented as a Maxwellian energy distribution in FLUKA, which means a small 'triangle' of cold electrons are not included (Figure 28). However, the laser-to-electron conversion efficiencies η from Figure 11 are calculated for all electrons, hot and cold. This small triangle of cold electrons may lead to a small overestimate in the bremsstrahlung dose yield during normalization by about 10–15% at any given laser intensity..

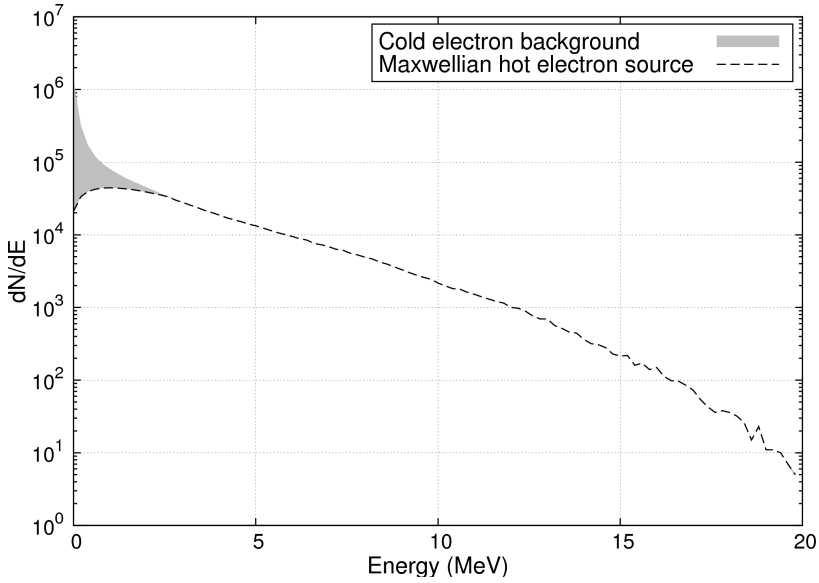

Figure 28: The cold electrons account for about 11% of the total hot electron energy in this EPOCH simulation with a laser intensity of 10^{20} W cm^{-2}.

4.3 FLUKA: bremsstrahlung photon shielding calculations

High-intensity laser-solid experiments may need radiation shielding to mitigate the bremsstrahlung dose generated by hot electrons. A systematic study in FLUKA used the hot electron source term characterized earlier with EPOCH (i.e., Maxwellian energy spectra with T_h derived from laser intensity) to calculate the transmission factors of several common shielding materials. The tenth value layer (TVL) thicknesses can then be derived from the transmission curves for each laser intensity. In this application, TVL is the thickness of the material at which the ambient dose equivalent of the incident radiation (bremsstrahlung photons) is reduced by $1/10$. The materials for this study and their densities are Pyrex glass (2.23 g cm^{-3}), Portland concrete (2.3 g cm^{-3}), aluminum (2.7 g cm^{-3}), iron (7.87 g cm^{-3}), lead (11.34 g cm^{-3}), and tungsten (19.25 g cm^{-3}).

Shielding calculations in FLUKA utilized a spherical geometry in Figure 29. For each laser intensity, the hot electrons with Maxwellian energy distribution and temperature T_h were emitted isotropically from the center of a Cu sphere. The radius of the Cu sphere 'target' was optimized to give the highest bremsstrahlung yield from hot electrons. For example at 10^{20} W cm^{-2}, the optimum radius of the Cu sphere was 2.5 mm, which corresponds to about a 1×CSDA range. A FLUKA particle transport routine ensured that hot electrons that escaped the Cu sphere would no be transported to the shielding material. Thus, only transmission of bremsstrahlung photons was calculated. A spherical shell of the shielding material of interest was located at 10 m (outer radius) from the source point to attenuate the generated bremsstrahlung photons. The 10 m distance was chosen to minimize dose from back-scattered photons. The ambient dose equivalent of bremsstrahlung photons was scored at the outer surface of the shielding shell at 10 m without and with varying thickness of shielding material.

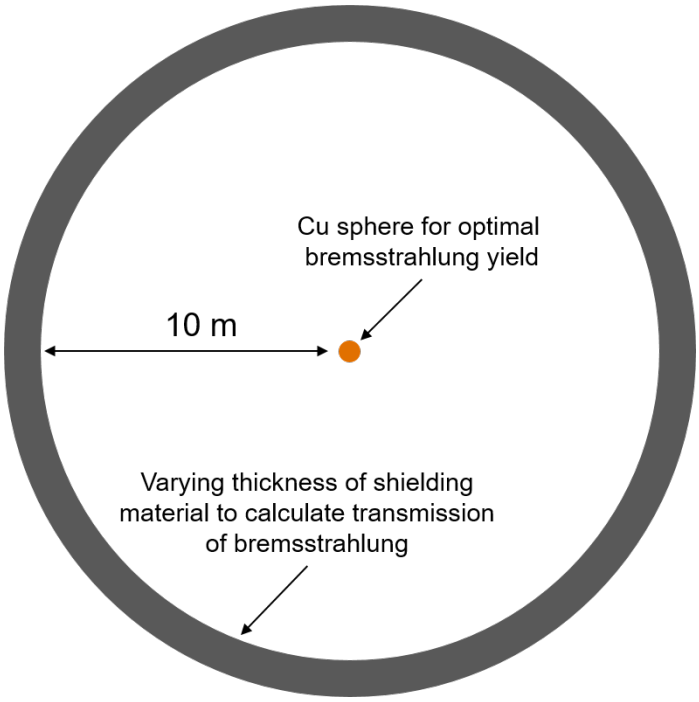

Figure 29: Spherical geometry implemented in FLUKA to calculate transmission of bremsstrahlung photons without and with varying thickness materials.

4.3.1 Bremsstrahlung energy spectra from hot electrons

Figure 30 demonstrates the shift in the bremsstrahlung energy spectra towards higher energies as the laser intensity increases. The units of bremsstrahlung fluence are given per cm^{-2} per primary particle (electron) in the FLUKA simulation. The selected laser intensities are in units of W cm^{-2} and are shown with their associated hot electron temperature T_h (keV or MeV), which characterizes the Maxwellian hot electron energy distribution.

The energy of the hot electrons (and hot electron temperature T_h) increases with laser intensity, and the subsequently generated bremsstrahlung photons also increase in energy. For example, the bremsstrahlung energy spectrum for a laser intensities on the order of 10^{21}–10^{22} W cm^{-2} reach up to about 100 MeV. Therefore, higher bremsstrahlung photon energies will require increasingly more shielding material to attenuate the ambient dose equivalent by a factor of $1/10$, as will be seen in the

following sections. Furthermore, the effect of buildup due to the high energy photons will also cause the first TVL layer to be greater than subsequent TVL layers for higher laser intensities.

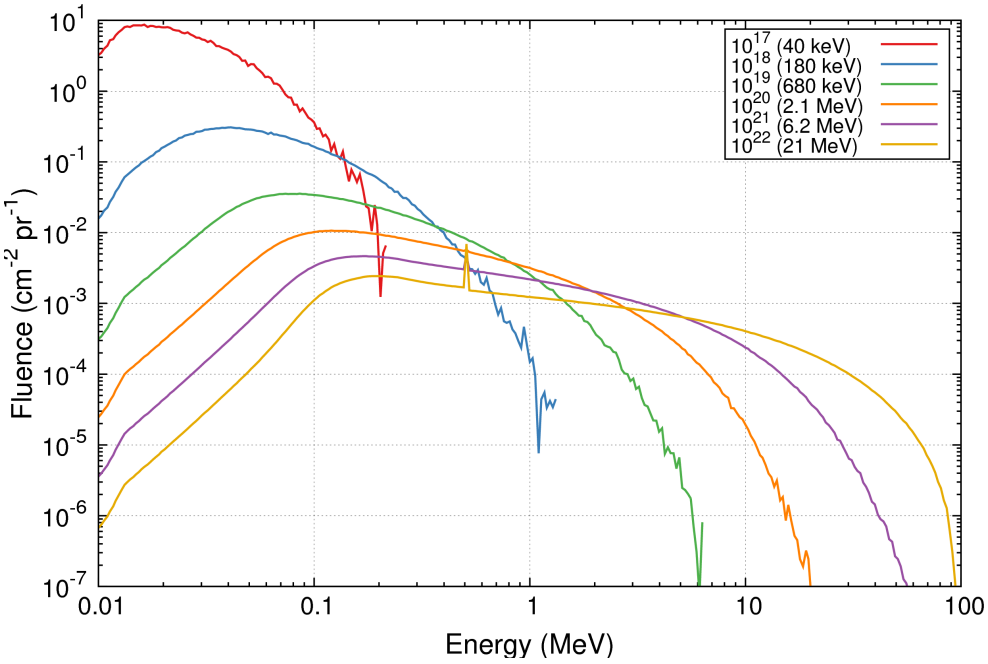

Figure 30: Bremsstrahlung energy spectra generated by hot electrons for specified laser intensities (in W cm^{-2}) and their associated hot electron temperatures T_h. Units of bremsstrahlung fluence are given per primary particle (electron) in the FLUKA simulation.

4.3.2 Transmission factors for bremsstrahlung photons

The ratios between the ambient dose equivalent of photons without and with shielding (and for increasing thicknesses of material) are the transmission factors. The transmission factors for glass, concrete, Al, Fe, Pb, and W as a function of shielding material thickness are shown in Figures 31–36 for selected laser intensities between 10^{17} and 10^{22} W cm^{-2}. At higher laser intensities where hot electron energies are also higher (tens of MeV), bremsstrahlung photons generate build-up in the shielding material. This effect is most clearly seen as a 'kink' in the transmission factor curves usually for 10^{21} and 10^{22} W cm^{-2}.

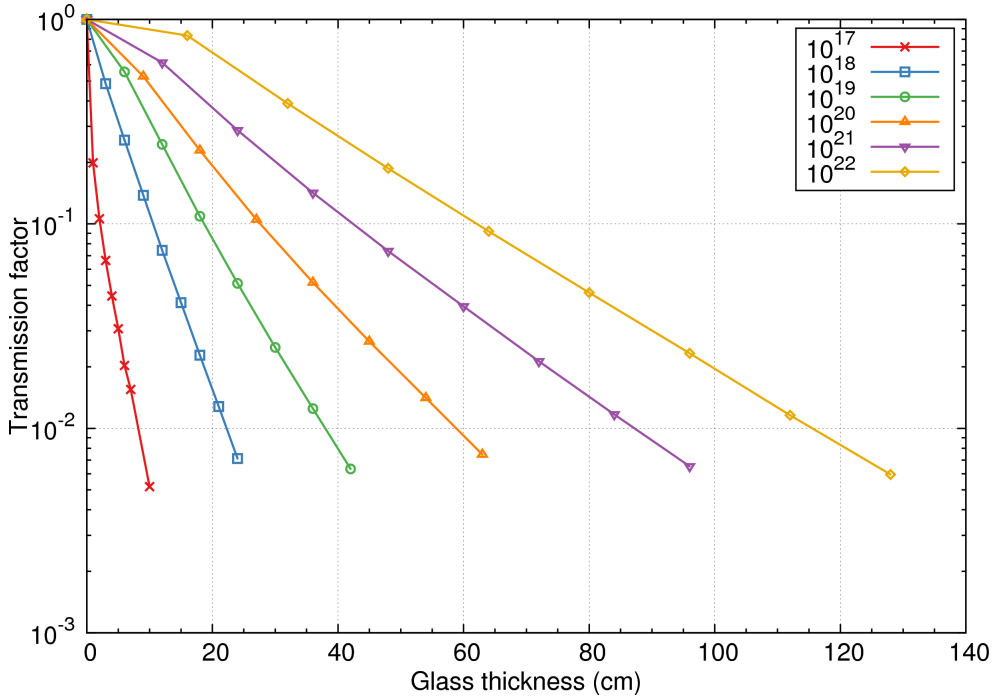

Figure 31: Glass transmission factors as a function of glass thickness for bremsstrahlung photons generated by a hot electron source and for selected laser intensities (W cm^{-2}).

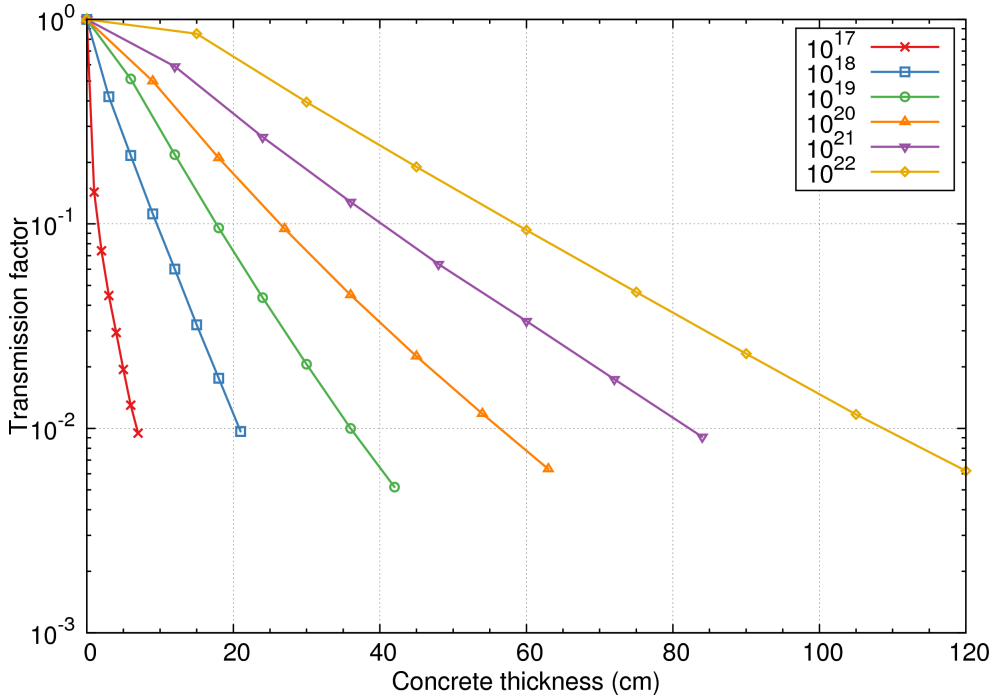

Figure 32: Concrete transmission factors as a function of concrete thickness for bremsstrahlung photons generated by a hot electron source and for selected laser intensities (W cm^{-2}).

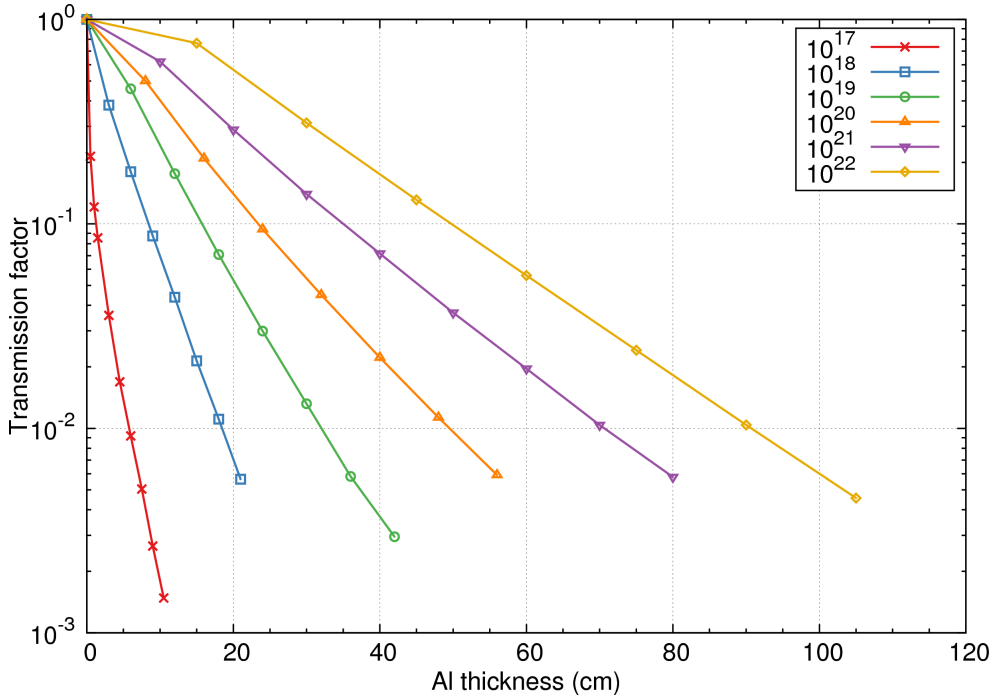

Figure 33: Al transmission factors as a function of Al thickness for bremsstrahlung photons generated by a hot electron source and for selected laser intensities (W cm^{-2}).

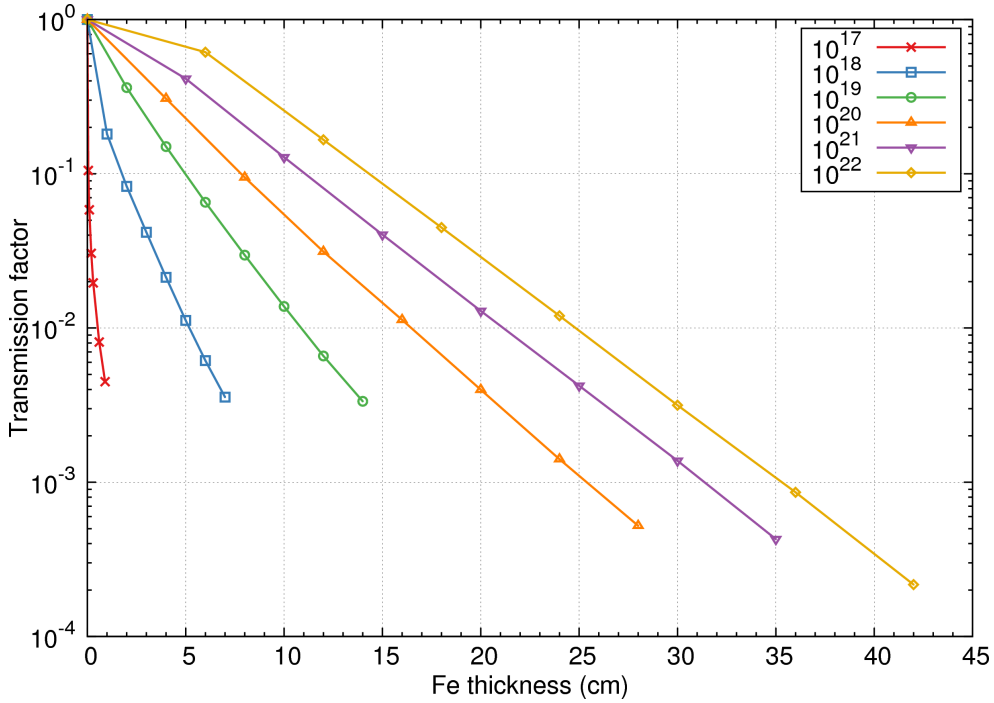

Figure 34: Fe transmission factors as a function of Fe thickness for bremsstrahlung photons generated by a hot electron source and for selected laser intensities (W cm^{-2}).

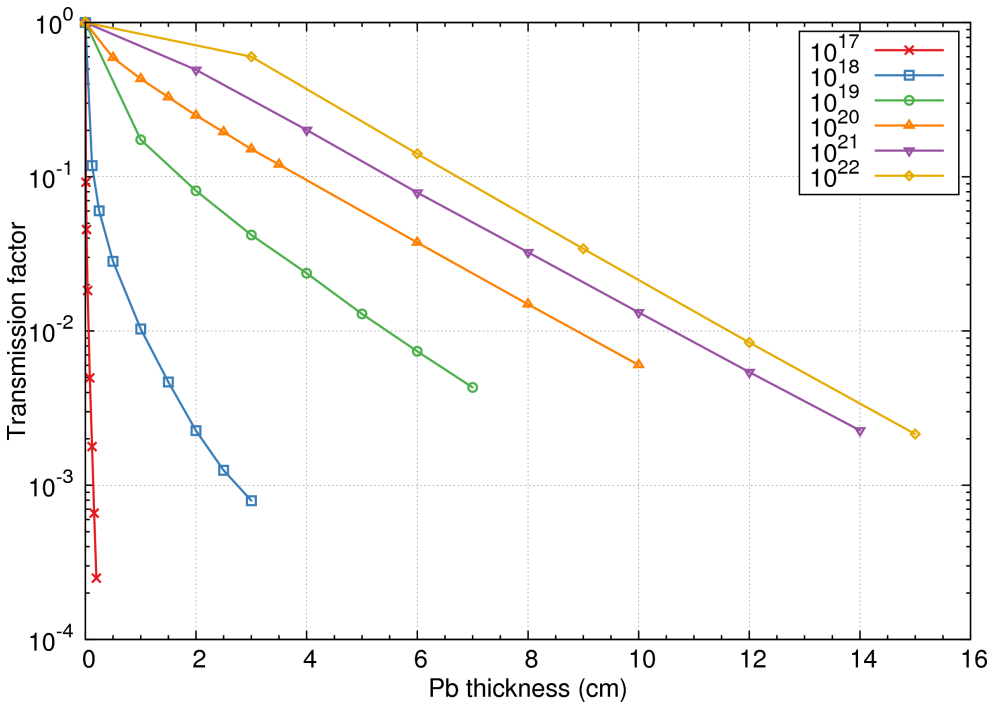

Figure 35: Pb transmission factors as a function of Pb thickness for bremsstrahlung photons generated by a hot electron source and for selected laser intensities (W cm^{-2}).

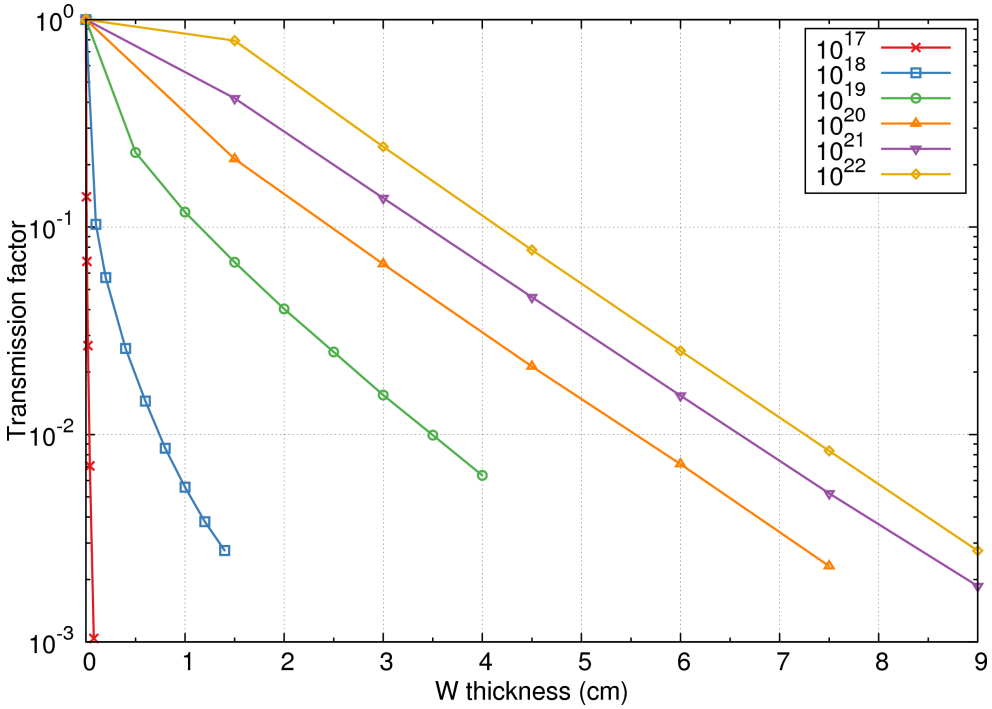

Figure 36: W transmission factors as a function of W thickness for bremsstrahlung photons generated by a hot electron source and for selected laser intensities (W cm^{-2}).

4.3.3 Derivation of tenth value layer thicknesses

A material's tenth value layer (TVL) is the thickness of material at which the intensity (dose) of the radiation (bremsstrahlung photons) entering is reduced by a factor of one tenth. The TVL for the common shielding materials can be derived from the transmission curves for the selected laser intensities. TVL_1 corresponds to the thickness required to reduce the ambient dos equivalent of bremsstrahlung photons by a factor of $1/10$. TVL_2 is the thickness needed for an additional $1/10$ reduction. As seen in Figures 31–36, TVL_2 is also the equilibrium tenth value layer (TVL_e).

Figures 37-42 plot the TVL_1 and TVL_e of glass, concrete, Al, Fe, Pb, and W as a function of laser intensity for bremsstrahlung photons generated by a hot electron source. TVL_e is consistently larger than TVL_1 for the lower Z and lower mass density materials (glass, concrete, and Al) except at around 10^{22} W cm^{-2}. At this intensity, the Maxwellian energy distribution of the hot electron source is described by the a T_h of 21 MeV (Equation 23) and has an average energy of about $1.5 \times T_h$ (32 MeV). As observed in another study,[62] this buildup effect causes TVL_1 to be greater than TVL_e at high laser intensities, and more concrete shielding is required for TVL_1 to reduce the ambient dose equivalent by a factor of $1/10$.

The effect of buildup on TVL_1 and TVL_e is more pronounced for the higher Z materials (Fe, Pb, and W) as can be seen at 10^{21} and 10^{22} W cm^{-2}. The thickness TVL_e plateaus around 10^{20} W cm^{-2} (T_h of 2 MeV), which corresponds to the high-energy limit or 'Compton minimum' of the high energy photons.

As expected, materials with higher Z and higher mass density are more effective for shielding photons, which translates to less material needed to attenuate dose by a factor of $1/10$. Glass, concrete, and Al have very similar values of TVL due to similarity of mass densities. Pb and W also have very similar TVL thicknesses and are the most effective materials in attenuating the dose from bremsstrahlung photons.

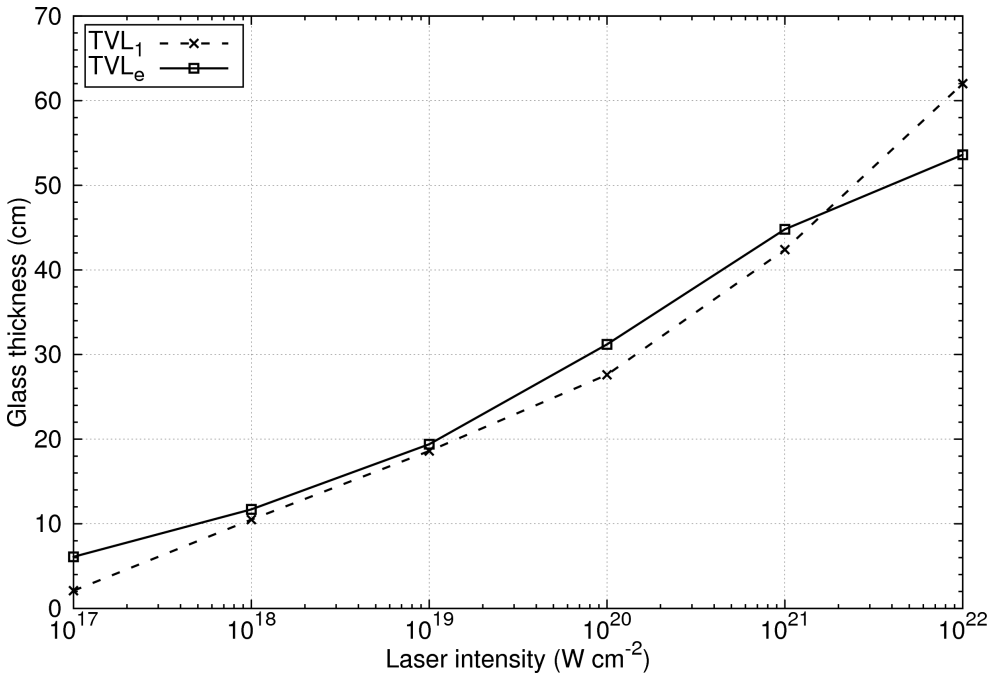

Figure 37: TVL_1 and TVL_e of glass as a function of laser intensity for bremsstrahlung photons generated by a hot electron source.

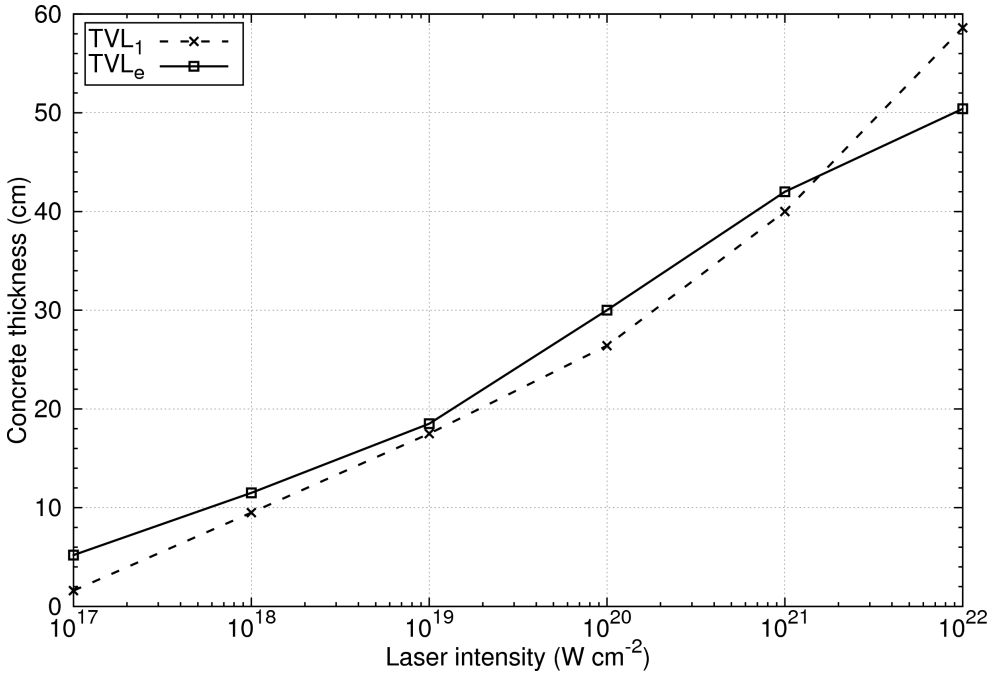

Figure 38: TVL_1 and TVL_e of concrete as a function of laser intensity for bremsstrahlung photons generated by a hot electron source.

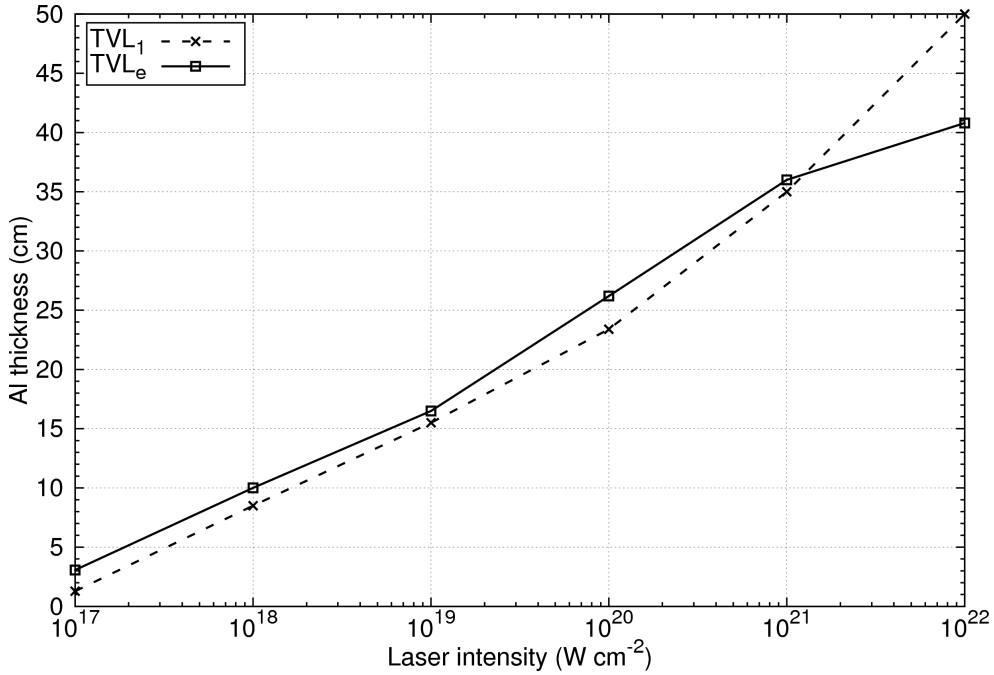

Figure 39: TVL_1 and TVL_e of Al as a function of laser intensity for bremsstrahlung photons generated by a hot electron source.

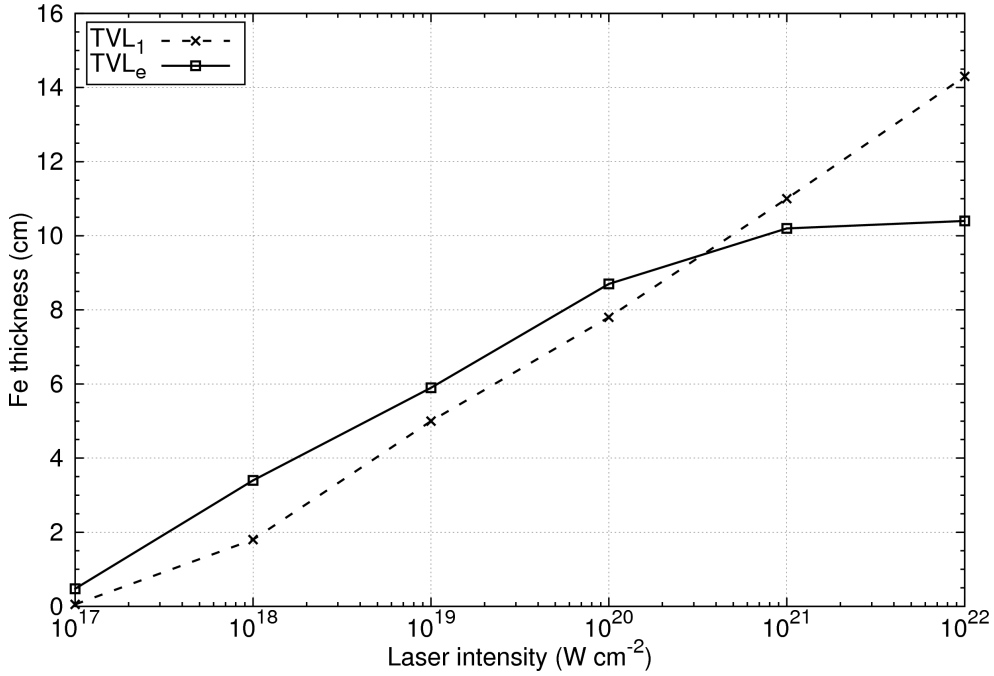

Figure 40: TVL_1 and TVL_e of iron as a function of laser intensity for bremsstrahlung photons generated by a hot electron source.

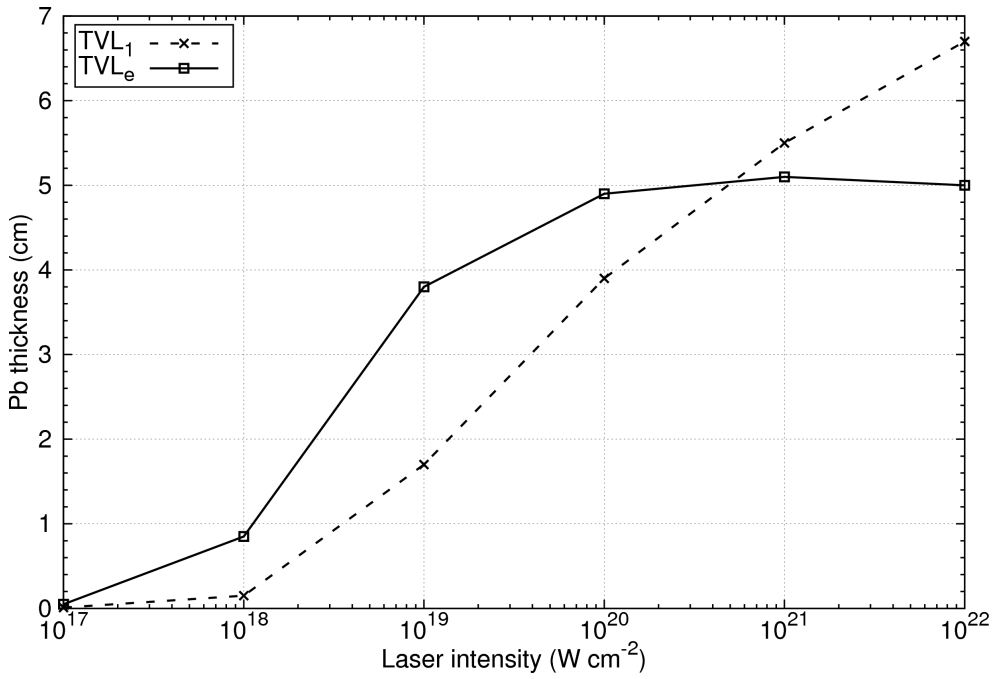

Figure 41: TVL_1 and TVL_e of Pb as a function of laser intensity for bremsstrahlung photons generated by a hot electron source.

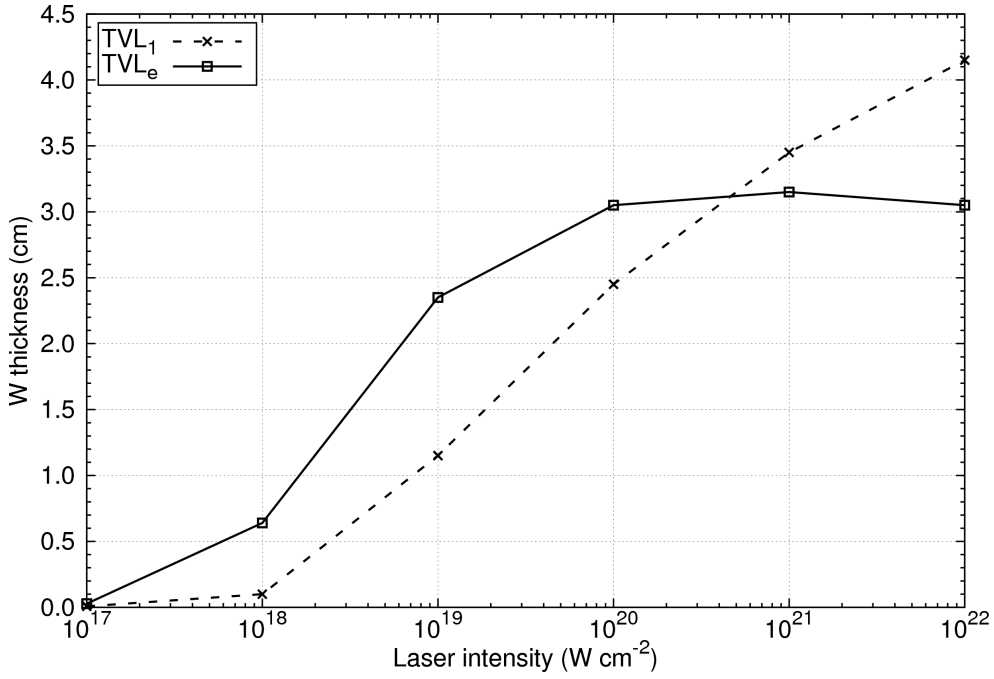

Figure 42: TVL_1 and TVL_e of W as a function laser intensity for bremsstrahlung photons generated by a hot electron source.

The TVL values presented in this section and the bremsstrahlung dose yield curves from earlier in Figure 26 can be used for designing radiation shielding for high-intensity laser-solid experiments. The thickness of TVL_1 can be larger than TVL_e at high laser intensities (higher energies) due to buildup. Radiation protection programs should account for this by using the TVL_1 thickness for the first TVL and by using the TVL_e thickness for each subsequent TVL.

CHAPTER V

LASER-SOLID EXPERIMENTS AT MEC

5.1 Laser beam diagnostics

This chapter of the dissertation covers the radiation dose measurements performed during laser-solid experiments at the MEC laser facility at SLAC. Proper characterization of the laser system's parameters is necessary to properly relate the parameters to experimentally measured bremsstrahlung dose yields. The information provided in this section about the laser diagnostics at MEC was compiled based on input received from MEC's laser scientists, review of experimental logbooks, and additional notes from meetings with MEC staff.

The laser-solid experiment at MEC during February 2014 will be used as an example of the laser diagnostic process. This was a commissioning experiment for MEC to operate at 25 TW, which was an upgrade over the previous system. The laser system for this experiment was a short-pulse Ti:sapphire optical laser operating at a wavelength of 800 nm and a repetition rate of 1 Hz. An off-axis parabolic (OAP) mirror focused the laser to a peak intensity of 1.8×10^{18} W cm^{-2} onto 100 μm-thick Cu foils.

5.1.1 Pulse energy measurement

The pulse energy of the laser beam was measured with a Coherent J50 50M-IR sensor and a Coherent LabMax-TOP meter. During the experiment, the pulse energy after the multi-pass analyzer and before the pulse compressor was measured as 1.5 J ($\pm$5%). The transmission of the compressor was 68% ($\pm$2%), and transmission of all spherical mirrors inside the target chamber was 100%. The reflectivity of the Al-coated OAP focusing mirror was 95% ($\pm$5%). Applying these factors yields a pulse energy of about

1 J being focused on the target.

Over the course of the laser-solid experiment, the Al-coated OAP mirror was progressively damaged by the energy absorbed from the laser pulse. After discussion with MEC personnel, the reflectivity of the OAP mirror may possibly have been as low as 80% (±5%) for 800 nm wavelength light, causing the OAP to absorb a significant portion of energy carried by each laser pulse and burn as a result. The degradation of the OAP mirror during the experiment was observed to halve the bremsstrahlung dose read by active instrumentation and suggests that the reflectivity of the mirror was reduced to about 50–60% as a result of burning. This lesson demonstrates the importance of ensuring laser optics are suitable for operating a laser powers and ensured that this did not occur again during future laser-solid experiments at MEC.

5.1.2 Pulse length measurement

The full width at half maximum (FWHM) pulse length was measured to be 70 ± 5 fs with a Coherent single-shot autocorrelator (SSA) on the day before the experiment. A second pulse length measurement was performed with an APE LX Spider autocorrelator and yielded 68 ± 2 fs. After the experiment, the same Coherent SSA yielded a pulse duration of 70 ± 5 fs. Thus, it was concluded that the pulse length did not change over the course of the experiment. The pre-pulse of laser was also measured, and the contrast ratio between the main pulse and pre-pulse was in the range of 10^6 to 10^8.

5.1.3 Spot size measurement

Laser spot size was determined by imaging the laser beam with an Adimec OPAL-1000 CCD camera. The taken images were of the laser beam with a pulse energy of a few mJ directly on the camera. The energy of the laser was increased incrementally, and no change to the beam was observed. In order to calibrate the CCD camera, the 300 mm last imaging lens in Figure 43 was shifted by set increments ranging from

5–15 μm using a motorized stand.

Shifting the lens also shifted the image taken by the CCD camera by a set amount. By observing how many pixels the image is shifted yielded a pixel calibration for the imaging system of 1.37 μm per pixel. This value agrees very well when the 4× magnification of the laser system is applied to the 5.5 μm per pixel native resolution of the CCD camera which yields 1.375 μm per pixel.

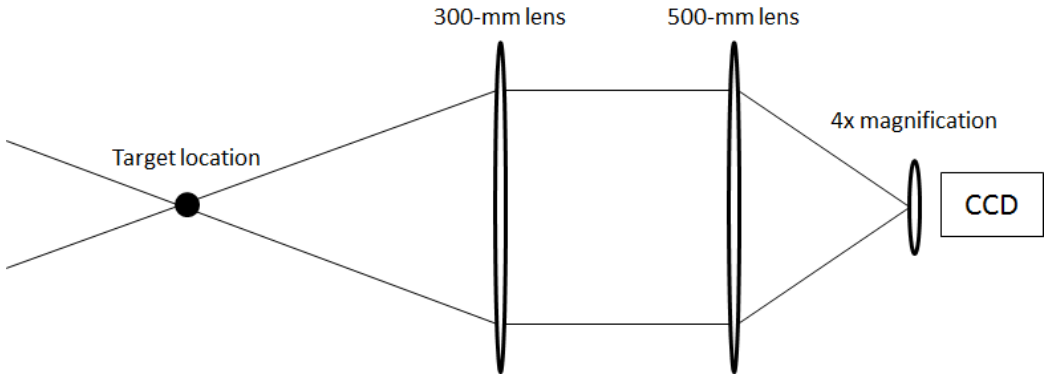

Figure 43: The CCD camera imaging setup used to calibrate the imaging system and determine the spot size of the laser beam.

To determine spot size of the laser beam, a pixel intensity profile was generated using `ImageJ` from a slice of beam image in Figure 44. The FWHM of the observed Gaussian-like peak can be converted to a FWHM spot size using the pixel calibration of 1.37 μm per pixel. The horizontal and vertical FWHM spot sizes were measured during the experiment to be 13 μm × 8 μm respectively. Assuming a Gaussian distribution, the FWHM spot sizes can be converted to $1/e^2$ radius spot sizes with Equation 22. The $1/e^2$ radial spot sizes are necessary values for calculating the peak laser intensity.

$$\omega_{x,y} = 0.8495 \times \mathrm{FWHM}_{x,y} \tag{22}$$

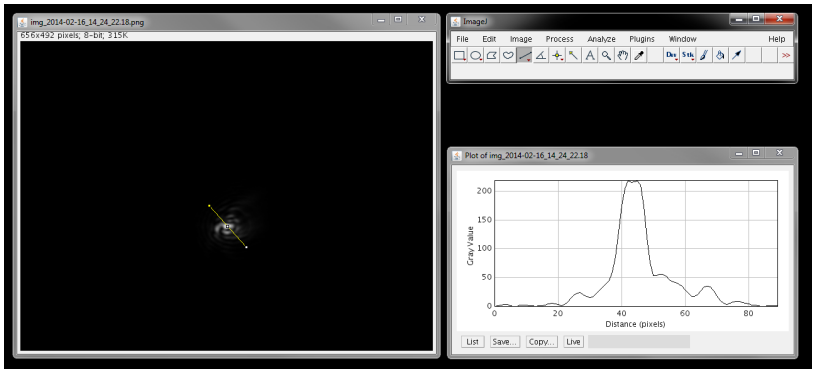

Figure 44: Laser beam intensity profile from the February 2014 laser-solid experiment at MEC that was generated from a diagonal 'slice' of the laser pulse in `ImageJ`.

5.1.4 Peak laser intensity

The peak laser intensity reported by MEC personnel during the experiment was 1.8×10^{18} W cm^{-2}. Calculation of the peak laser intensity assumed the beam to have a Gaussian-like profile where the fraction of energy in the beam's main peak was about 0.19 of the total focused energy. The remaining fraction of the laser's total energy was found under the artifact peaks surrounding the main peak. A 3D projection of the beam is shown in Figure 45.

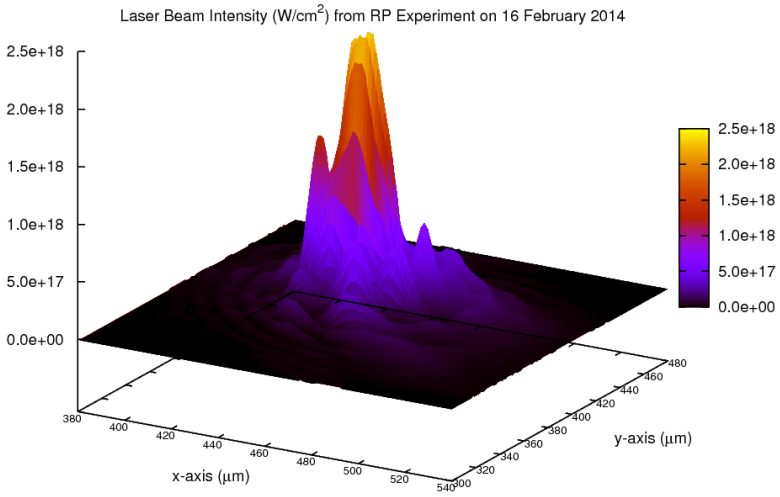

Figure 45: A 3D projection of a laser pulse from the February 2014 laser-solid experiment at MEC. Notice that fractions of the total focused energy are found under the artifact peaks surrounding the main peak.

With the laser parameters reported by MEC laser scientists during the experiment, the peak laser intensity was calculated to be 1.8×10^{18} W cm^{-2}. As this was the MEC commissioning experiment for 25 TW operation, future laser-solid experiments improved upon the laser intensity by focusing more of the total energy under the main peak as will be seen in later sections.

5.2 Radiation dose measurements

A combination of passive and active detectors were used to measure the radiation doses generated from laser-solid interactions during experiments at MEC. Passive instruments performed integrated dose measurements during laser shots on targets, while active instruments consisted of radiation detectors that recorded the change of radiation dose levels over time. These instruments were deployed inside the target vacuum chamber, around the outside of the chamber, and around the MEC facility.

The passive dosimeters included Arrow-Tech Model 2 pocket ion chambers with a full scale range of 0–20 μSv or 0–2 mSv, Mirion Technologies (MGP) RADOS RAD-60 electronic dosimeters, and Landauer nanoDot dosimeters. Only the nanoDot dosimeters were approved for use inside the MEC target vacuum chamber due to concerns of out-gassing. The nanoDots were expected to record high absorbed dose (mGy) values from the mixed field of electrons and photons inside the target chamber. The 0.02 and 2 mSv PICs and RADOS were deployed around the outside of the target chamber to measure the ambient dose equivalent of bremsstrahlung photons (μSv) that escaped the target chamber.

Active instruments included Victoreen 451P hand-held ion chambers, HPI-6031 styrofoam-walled ion chambers, PTW-7262 pressurized argon ion chambers, and polyethylene-moderated BF_3 neutron detectors. Two HPI ion chambers (designated HPI-01 and HPI-02) were positioned directly outside the target chamber. One PTW ion chambers (PTW-01) was located inside the control room of the MEC laser facility,

which is located on the second floor above the the hutch. A second (PTW-02) was located at the steel roll-up door outside the hutch. The Victoreen meters and BF_3 detectors were deployed at various angles and distances around the outside of the target chamber. The active instruments provided real-time dose monitoring information (μSv h^{-1}) during the laser-solid experiments.

5.2.1 Target chamber configuration

The target chamber located at the MEC laser facility has a radius of about 1 m and is constructed from Al. The target chamber is pumped down to vacuum conditions prior to laser shots on target in order to achieve high laser intensities. A plane-view of the target chamber is shown in Figure 46. The chamber's wall thickness varies around but is typically 2.54 cm-thick, and the chamber doors have variable thickness of about 5.08–6.24 cm thickness. Glass viewports are located around the target chamber at its flanges to give experimenters access to the inside of the chamber with their diagnostics. The unfocused short-pulse laser enters the target vacuum chamber from the left and is directed with a series of mirrors to an OAP focusing mirror. The laser beam is focused to a high-intensity and interacts with the target material at the center of the target chamber. The lenses and mirrors located downstream of the laser-matter interaction point were used before the start of the experiment for characterizing laser beam parameters.

The MEC's short-pulse laser system can operate at repetitions rates of 1 Hz and 5 Hz, so a target rastering system at the center of the chamber ensures each laser shot interacts with fresh target material. Furthermore, as seen in Figure 46, two 12 cm thick steel shields were deployed inside the MEC target chamber in the forward and backward directions of the laser beam to evaluate their effectiveness at shielding the generated ionizing radiation.

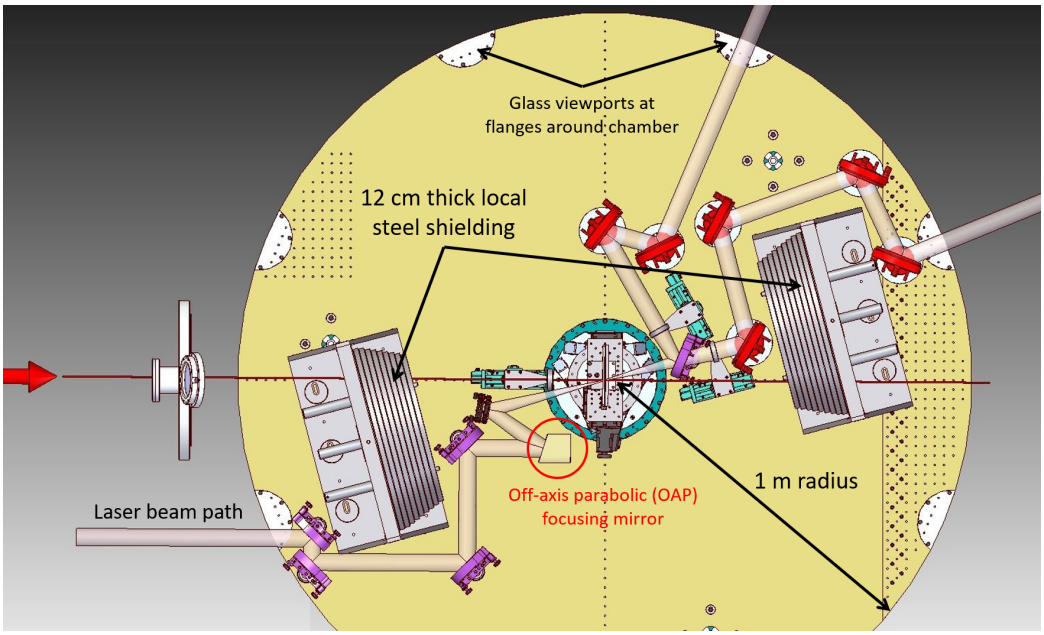

Figure 46: Inside view of the laser-optic setup of the MEC target vacuum chamber during the February 2014 laser-solid experiment. The OAP focuses the laser beam to micrometer spot sizes onto the 100 μm Cu target at the center of the target chamber.

5.2.2 Overview of laser-solid experiments

Radiation measurements were performed during four high-intensity laser-solid experiments at the MEC in 2014. Each experiment utilized the MEC's Ti:sapphire short-pulse laser system with wavelength of 0.8 μm, 1 J pulse energy, and 40 fs FWHM pulse length. This provided a laser beam with a peak power of 25 TW, and laser intensities between 10^{17} and 10^{20} W cm^{-2}. Table 2 gives an overview of the laser beam parameters from the four laser-solid experiments at MEC in 2014. The highest peak intensity achieved was 7.1×10^{19} W cm^{-2}. The uncertainty in the achieved peak intensities were calculated to be 38% for the February experiment, 22% for July, 21% for August, and 29% for September.

Table 3 provides a comprehensive list of the solid foils and their respective thicknesses that were used as targets during the four laser-solid experiments at MEC in 2014. The number of laser shots on each target is also provided. During an experiment, several different target materials may be used, which involves releasing the

Table 2: Laser beam parameters for four laser-solid experiments at MEC in 2014.

Experiment	Pulse energy (J)	Pulse length (fs)	Fraction of energy in peak	Peak power (TW)	$1/e^2$ spot size (μm $\times$ μm)	Peak intensity (W cm^{-2})
Feb 2014	1.0	70	0.19	2.8	13×8	1.8×10^{18}
Jul 2014	0.7	50	0.77	10.7	37×19	1.0×10^{18}
Aug 2014	0.7	50	0.44	6.1	9×5	1.0×10^{19}
Sep 2014	0.5	50	0.63	6.3	3×2	7.1×10^{19}

vacuum on the target chamber and swapping targets on the rastering system.

Table 3: Target types and thicknesses for the four laser-solid experiments at MEC in 2014. The number of laser shots taken on each target configuration is also provided.

Intensity (W cm^{-2})	Target material	Thickness (μm)	Number of laser shots
1.8×10^{18}	Cu	100	540
1.0×10^{18}	Cu+Kapton	5+30	550
	Ni	15	275
	Cu	100	655
1.0×10^{19}	Cu	100	340
	Ni	15	220
7.1×10^{19}	Al	15 & 10	70 & 66
	Au	5	22
	Cu	5	26
	CH_3	4 & 2.5	6 & 37

5.3 Dose inside target chamber

The small 1 cm $\times$ 1 cm passive nanoDot dosimeters from Landauer were deployed inside the target vacuum chamber during laser-solid experiments. The dosimeters were set at 30 cm distances radially around the laser-target interaction location and care was taken to ensure they had direct line-of-sight for each experiment configuration. These nanoDot dosimeters measured the dose in mGy from a mixed field of hot electrons and bremsstrahlung photons.

The nanoDot measurement results presented here are based on a Kr-85 shallow dose calibration factor that accounts for the high-fluence electron field inside the

target chamber. The doses measured inside the target chamber are high on the order of tens of mGy per laser shot. However, the majority of this dose is dominated by electron dose, which is attenuated by the Al walls of the target chamber.

5.3.1 February 2014, 1.8×10^{18} W cm^{-2}

Figure 47 shows the dose per shot measured by nanoDots during the February 2014 laser-solid experiment at MEC with peak intensity of 1.8×10^{18} W cm^{-2}. The laser-target interaction point is at the center of the radial plot, and the direction of the laser beam (or laser axis) is indicated. The focused laser beam was incident on the Cu foil at an angle of 15° relative to target normal. The dose has been normalized to the total number of laser shots delivered onto the 100 μm Cu foil, and the maximum measured dose per shot is about 12 mGy per shot in the laser backward direction and 1.7 mGy per shot in the forward direction.

The radial dose profile indicates that the mixed field of electrons and bremsstrahlung photons is primarily directed in the forward and backward laser axis directions. Two possible factors may contribute to the difference between the measured forward and backward dose: target thickness and laser intensity. Studies at other facilities have shown that the dose is dominantly in the forward direction.[49] However, these studies utilize filters to measure only electrons of 100 keV and greater, or they use a very high laser intensity between 10^{19} and 10^{20} W cm^{-2}. The measurements here include dose from low energy electrons along with high energy, and the laser intensity is also comparatively low at 1.8×10^{18} W cm^{-2}. In addition, the 100 μm-thick Cu foil in this experiment is considered thick for low energy electrons. This shows the complexity of energy and angular distributions of hot electrons and their implications on the bremsstrahlung photon doses that escape outside target chamber.

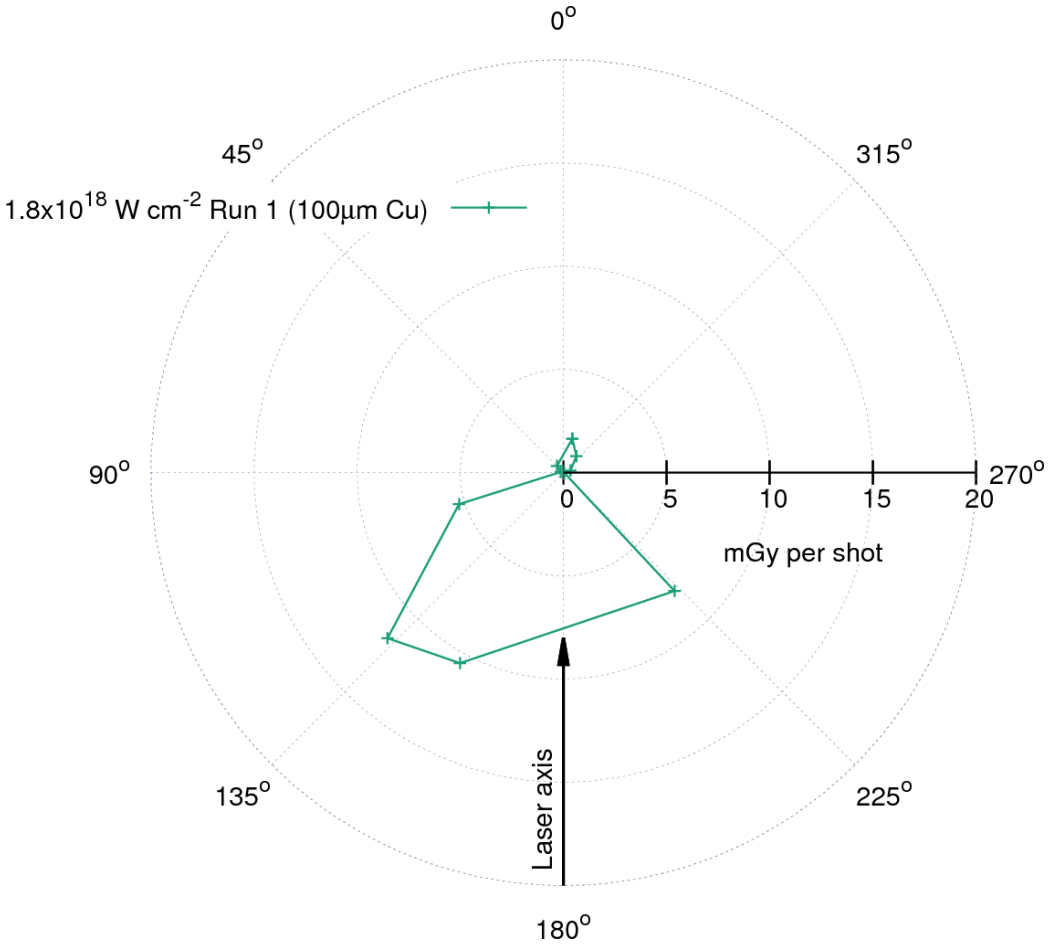

Figure 47: Dose (mGy) per shot at 30 cm inside the target chamber from 540 laser shots with peak intensity of 1.8×10^{18} W cm^{-2} on a 100 μm Cu foil during the February 2014 laser-solid experiment at MEC.

5.3.2 July 2014, 1×10^{18} W cm^{-2}

The laser-solid experiment at MEC during July 2014 utilized three different solid target types with a peak laser intensity of 1×10^{18} W cm^{-2}. The laser beam was incident at 90° to the target for all shots. Two of the targets were Cu foils of different thicknesses. A 5 μm thick Cu foil with 30 μm Kapton backing was used to characterize dose with very thin targets. The Kapton backing supported the Cu foil to prevent warping from sustained laser shots on target. A 100 μm thick Cu foil was also used to compare with results from the measurement in February 2014.

The third solid target type was a 15 μm-thick Ni nanowire target provided by

R.S. Marjoribanks from Lawrence Livermore National Laboratory (LLNL). Figure 48 shows a visual example of a nanowire target from an experiment outside SLAC but similar to the one used at MEC.

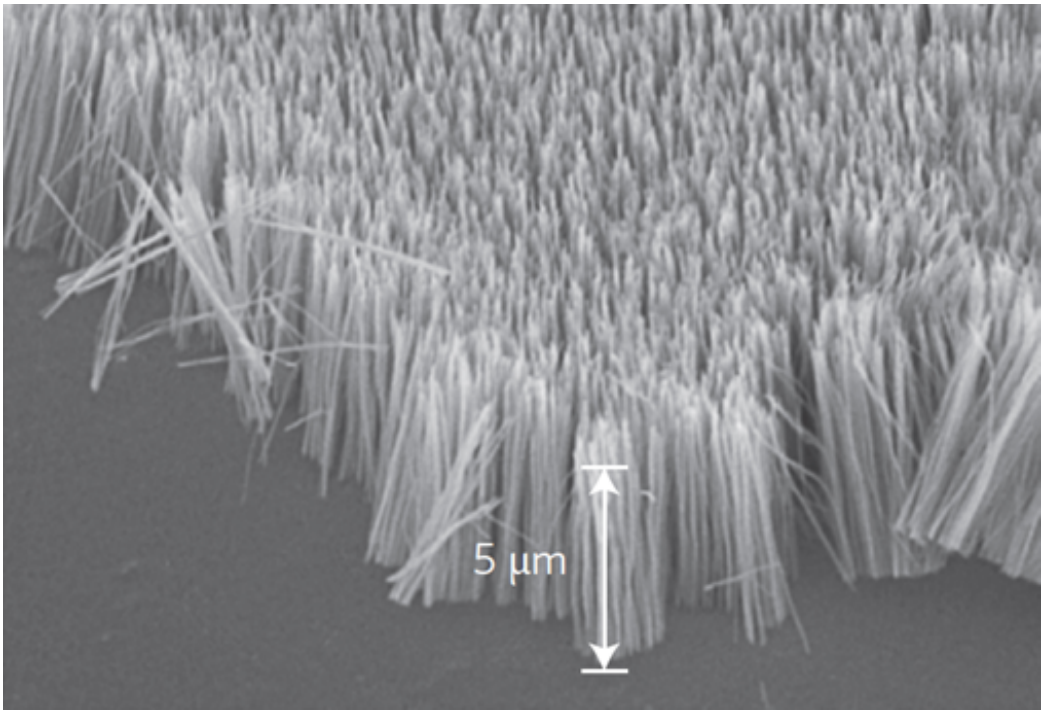

Figure 48: Example of the Ni nanowire used during the July 2014 laser-solid experiment at MEC. The target used during the experiments at MEC had a thickness of 15 μm. Image from Purvis *et al.* (2013).[50]

It has been observed at these other facilities that nanowire targets offer very high laser energy to plasma hot electron energy conversion of around 95% and can even achieve nearly 100 times greater electron densities than typical solid targets.[50,36] This unique target was use to evaluate if it would potentially generate a higher bremsstrahlung dose hazard than regular solid targets.

Figure 49 shows the dose per shot measured by nanoDots during the July 2014 laser-solid experiment at MEC with peak intensity of 10^{18} W cm^{-2}. Several hundred laser shots were taken on each solid target and constituted different experiment runs: 550 shots on 5 μm Cu, 275 shots on 15 μm Ni nanowire, and 655 shots on 100 μm Cu. The peak dose per shot was measured to be about 15 mGy per shot in the backward

laser direction. In the forward laser direction, Runs 1 and 2 with the thinner solid targets (5 μm Cu and 15 μm Ni) measured in the range of 5–7 mGy per shot, while Run 3 with the thicker 100 μm Cu foil measured about 2 mGy per shot.

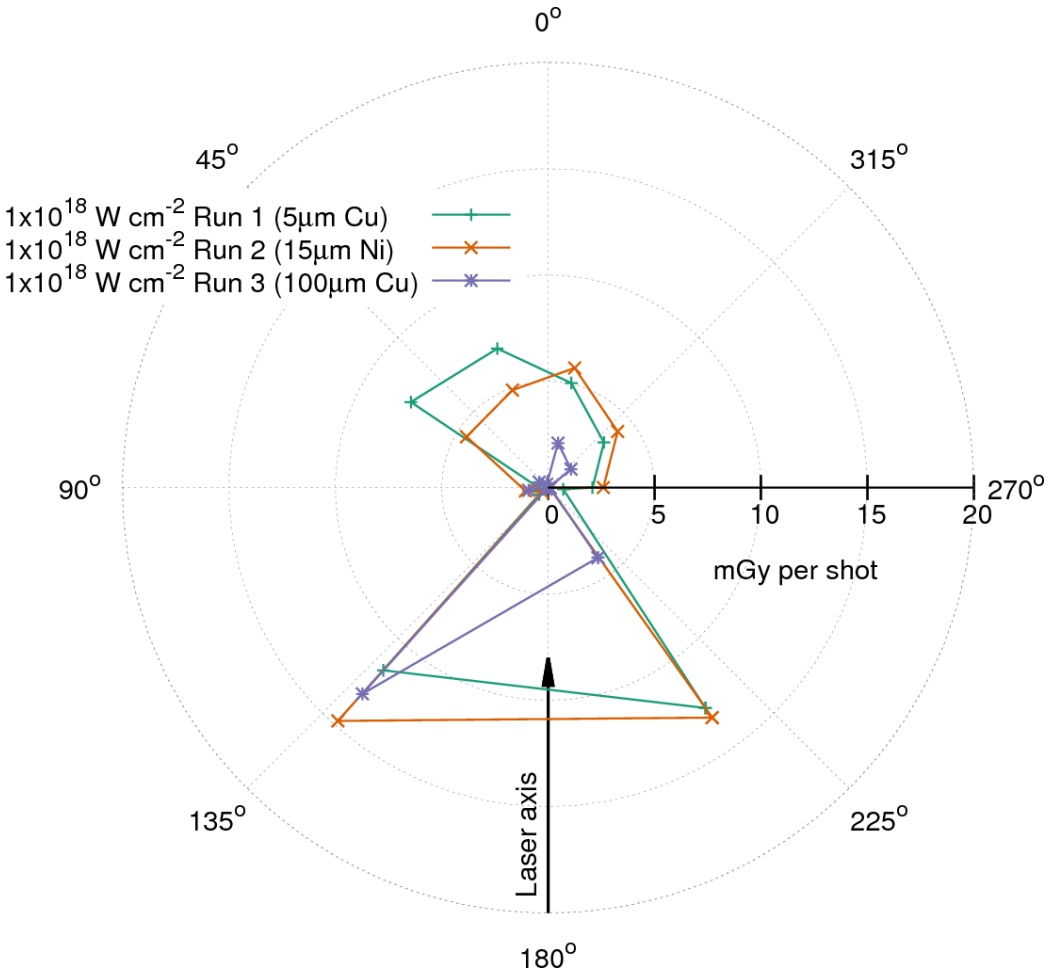

Figure 49: Dose (mGy) per shot at 30 cm inside the target chamber from a laser with peak intensity of 1×10^{18} W cm^{-2} on Cu and Ni foils during the July 2014 laser-solid experiment at MEC. The dosimeter at about 225° was blocked before run 3 by an Al shield that was inserted to protect the OAP mirror.

The profiles for 5 μm Cu foil and 15 μm Ni nanowire agree in the forward direction. On the other hand, the 100 μm Cu foil is thick compared to the 5 and 15 μm foils. The hot electron temperature at 10^{18} W cm^{-2} is in the range of 100–200 keV, so a larger fraction of the electron dose is attenuated by 100 μm of Cu. Therefore, the

dose profile is noticeably smaller in magnitude in the forward direction due to self-shielding effect of the thicker 100 μm Cu foil. This corresponds very well with the radial dose profile from the February 2014 measurement in Figure 47.

In the laser backward direction, all three radial distributions agree very well and are nearly symmetric, except for the one data point at about 225° for Run 3 with the 100 μm Cu foil. Between Runs 2 and 3, MEC scientists placed an Al screen to protect the OAP focusing mirror from being coated by target material debris. The Al screen successfully protected the optic but inadvertently blocked the line-of-sight of the nanoDot at 225° from the laser interaction point. From symmetry, the screen attenuated the electron-dominated dose by a factor of 1/3. For all three solid targets, much less dose was measured in the laser lateral (90° and 270°) directions compared to forward and backward directions, and this demonstrates again that the hot electron emission is also primarily in the forward and backward directions.

5.3.3 August 2014, 1×10^{19} W cm^{-2}

Similar to July 2014, the radiation measurements in August 2014 used a 100 μm Cu foil and the 15 μm Ni nanowire target. A total of 340 laser shots were taken on the 100 μm Cu foil and 220 shots on the Ni nanowire. To prevent damage to optical components from laser back-reflection off the target material, the target was oriented such that the laser was incident at 15° to target normal.

Figure 50 shows the dose per shot at 30 cm measured by nanoDot dosimeters during the August 2014 laser-solid experiment at MEC with peak intensity of 1×10^{19} W cm^{-2}. Between the two target types, the dose per shot measured is quite similar except for two locations, and these two locations (one at 315° and another at 190°) only differ by a factor of 2. The dose is slightly peaked up to 12 mGy per shot in the laser forward direction, and a large amount of dose per shot up to 40 mGy per shot was measured in the laser backward direction. In contrast to the radial

doses presented earlier, a significant amount of dose of around 10 mGy per shot was measured in the lateral directions.

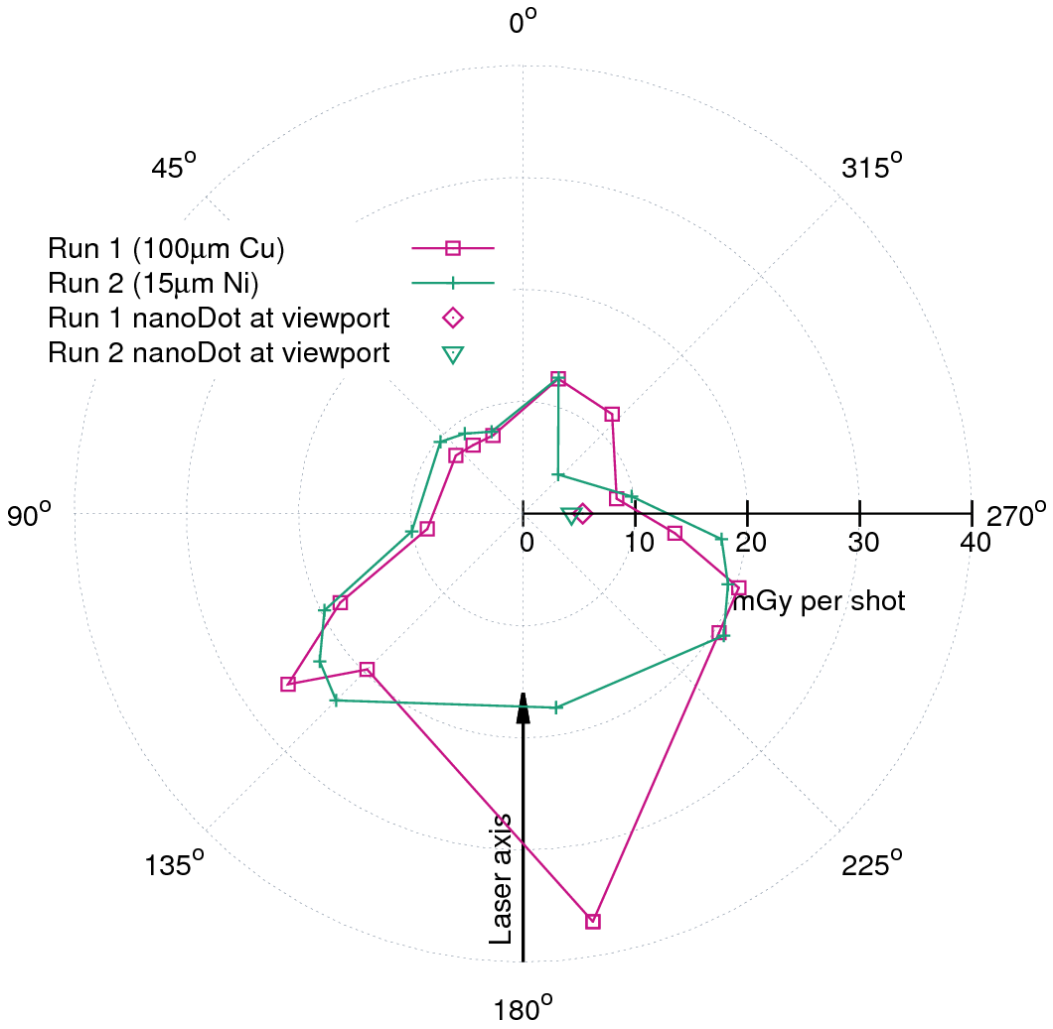

Figure 50: Dose (mGy) per shot at 30 cm inside the target chamber from a laser with peak intensity of 1×10^{19} W cm^{-2} on Cu and Ni foils during the August 2014 laser-solid experiment at MEC. A nanoDot was deployed during each run outside the target chamber at a very thin diamond viewport, and the dose was normalized to a distance of 30 cm.

The self-shielding effect due to target thickness is significantly less pronounced than earlier in Figure 49. At a laser intensity of 10^{19} W cm^{-2}, the average energy of the hot electrons' Maxwellian energy distribution is about 1.0 MeV (1.5×0.68 MeV), so attenuation of these hot electrons by the micrometer-thick targets is less than at lower laser intensities. Therefore, the dose per shot recorded in the forward laser

direction is very similar.

During each run of the August 2014 experiment, an additional nanoDot dosimeter was deployed outside a diamond view port at 270°. Similar to the dosimeters inside the chamber, it measured the integrated dose for each run. The diamond viewport had a radius of 1 cm and thickness of 100 μm. Assuming the 100 μm-thick diamond provides no shielding, the integrated dose can be normalized to laser shots in a run and to a distance of 30 cm inside the chamber. This normalized dose per shot agrees well within a factor of 2 with the other measurements in Figure 50.

5.3.4 September 2014, 7.1×10^{19} W cm^{-2}

During the September 2014 laser-solid experiment at MEC, the experimenters focused the laser to a peak intensity of 7.1×10^{19} W cm^{-2} onto an assortment of solid foils over multiple runs. Furthermore, experimenters also attempted to deliver laser shots onto a jet of liquid H_2 (LH_2) for the first time at SLAC. A summary of the runs, the target types, and number of laser shots are summarized in Table 4. Due to great difficulty in hitting the 5 μm diameter LH_2, there were few successful shots on the liquid target, and the number was not tracked.

Table 4: Laser target materials and the number of laser shots delivered for each run of the September 2014 laser-solid experiment at MEC.

Run #	Run 1	Run 2	Run 3	Run 4
Target type (# shots)	15 μm Al (70)	LH_2 jet (not tracked) 5 μm Au (22) 5 μm Cu (26) 4 μm CH_3 (6)	10 μm Al (66)	2.5 μm CH_3 (37) LH_2 jet (not tracked)

Figure 51 shows the radial profile of the dose per shot at 30 cm inside the target chamber during the September 2014 experiment at MEC for the four runs. The laser beam was incident on the solid foils at 45° relative to target normal. Because the number of successful shots on the LH_2 were untracked, the normalization of the measured doses from the nanoDots assumed no successful shots onto the liquid target.

The target configuration inside the MEC chamber also allowed for seamless transition between runs 2 and 3, and there was no need to vent the target chamber and swap targets. Therefore, the nanoDots measured the integrated dose from laser shots on several target types during runs 2 and 3.

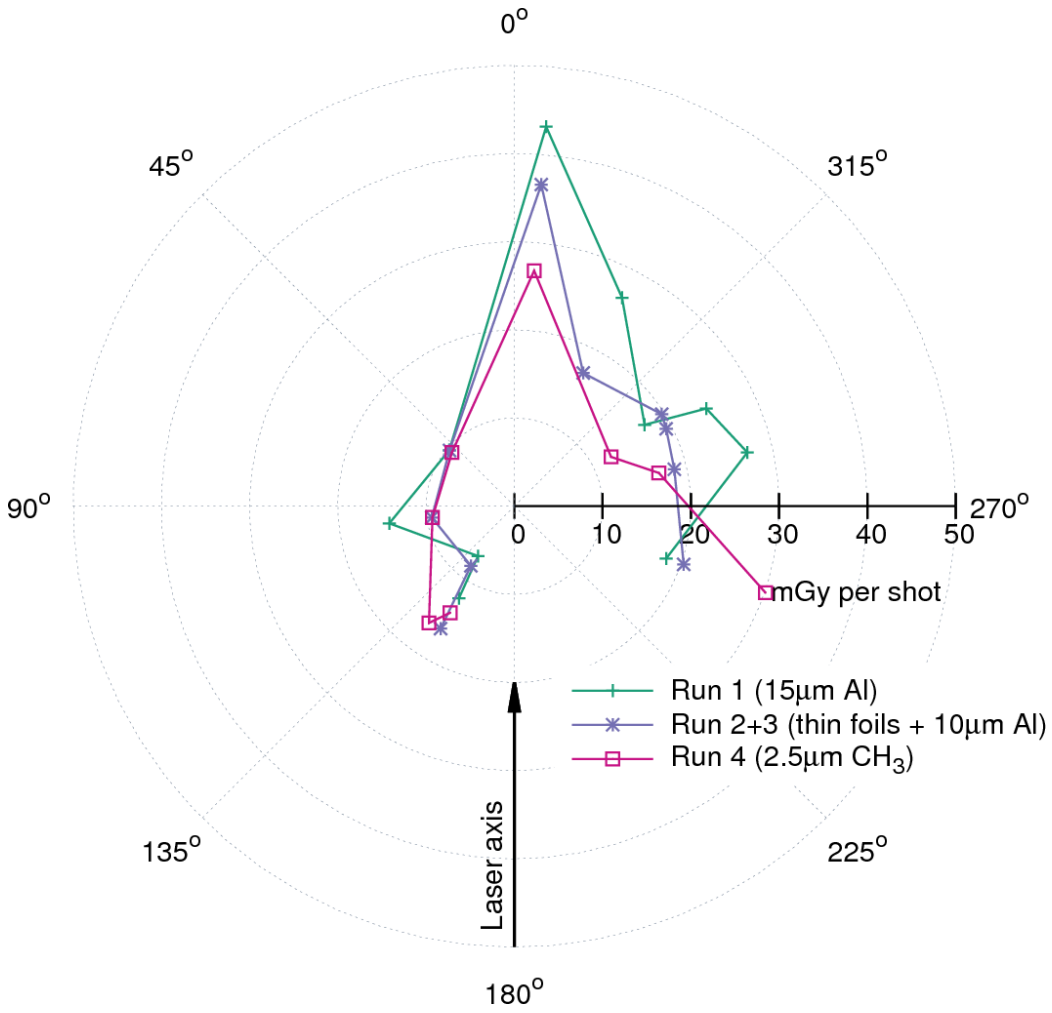

Figure 51: Dose (mGy) per shot at 30 cm inside the target chamber from a laser with peak intensity of 7.1×10^{19} W cm^{-2} on assorted solid foils during the September 2014 laser-solid experiment at MEC.

The radial dose profiles for all four runs agree well in the forward (0°) and lateral (90°) directions. Dosimeters in the forward direction towards 0° measured in the range of 30–40 mGy per shot. Dosimeters in the lateral directions measured between 10–20 mGy per shot, which is about a factor of 2 less than the forward direction.

The solid foil type and thickness had little measurable effect on the dose per shot. At a laser intensity of 7.1×10^{19} W cm^{-2}, the hot electrons are in the range of several MeV in energy, so attenuation by the thin micrometer-thick targets is negligible. This effect was similarly seen earlier in Figure 50 for 10^{19} W cm^{-2}. Dosimeters in the laser backward direction were shielded by laser-optics equipment added into the chamber and are not shown in Figure 51. Although dose information in the backward direction was unavailable, the dose per shot is sharply forward peaked. Comparison with the previous sections demonstrates that the shape and magnitude of the dose profiles depend on the laser intensity with some dependence the target thickness for lower laser intensities around 10^{18} W cm^{-2}.

5.4 Bremsstrahlung dose outside target chamber

Hot electrons generated from laser-solid interactions will interact with the target material and the target chamber walls to generate bremsstrahlung photons. During the laser-solid experiments at MEC in 2014, Victoreen 451P ion chambers were positioned around the outside of the target chamber and recorded in real time the ambient dose equivalent, $H^*(10)$, rate of bremsstrahlung photons as micro-Sieverts per hour (μSv h^{-1}). The ambient dose equivalent rate will be referred to as simply dose rate. Two HPI ion chambers are also permanently deployed at the MEC target chamber to monitor the dose rates.

The ion chambers were deployed in the forward and backward laser directions and at viewports if they were available. If space allowed, ion chambers were also deployed at increasing radiation distances to observe the drop in dose rate over distance. For these active measurements, the laser system at the MEC operated at 1 Hz repetition rate. Dose rates are shown 'as measured' and have not been normalized to any distances. Recall the target vacuum chamber at MEC has a radius of about 1 m.

5.4.1 February 2014, 1.8×10^{18} W cm^{-2}

Figure 52 shows the maximum bremsstrahlung dose rate with background subtracted (2 μSv h^{-1}) measured by active instruments during the February 2014 laser-solid experiment at MEC. The maximum dose rate of 60 μSv h^{-1} was measured by at about 122° relative to the laser forward direction. This angle corresponds well with the peak dose per shot (mGy per shot) measured by the nanoDot dosimeters inside the target chamber in Figure 47.

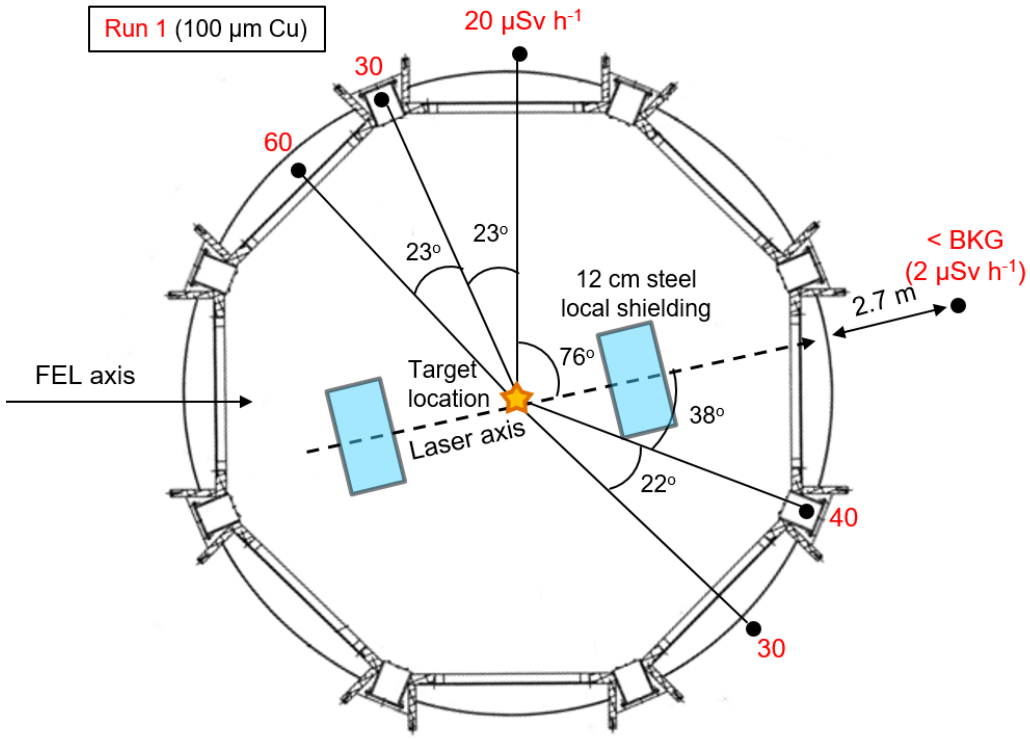

Figure 52: Bremsstrahlung dose rates (μSv h^{-1}) outside the target chamber from a laser with peak intensity of 1.8×10^{18} W cm^{-2} on a 100 μm Cu foil during the February 2014 laser-solid experiment at MEC.

Local shielding constructed from steel plates (12 cm total thickness) was deployed in both the forward and backward laser directions to test their efficacy in mitigating

the generated bremsstrahlung dose. The shielding was designed to attenuate bremsstrahlung generated from laser-solid interactions up to about 10^{20} W cm^{-2}. Thus, the addition of the steel local shielding for this 1.8×10^{18} W cm^{-2} experiment completed attenuated the bremsstrahlung in the forward direction, and the ion chamber measured no signal above background. Other than the shielded location, the bremsstrahlung dose rates measured outside the target chamber in Figure 52 agree well within a factor of 2–3. Differences between the dose rates outside the target chamber may be due to the variation in Al wall thickness and the measurement location's angle with respect to the laser direction.

During the February 2014 experiment, the OAP focusing mirror sustained damage from the high-power laser beam, which decreased its reflectivity and resulted in incrementally less energy (and lower peak intensity) delivered onto the 100 μm Cu foil. As a result, the ion chambers saw an incremental decrease in bremsstrahlung dose rate over the course of the 540 laser shots. Figure 53 shows the decrease in the measurable bremsstrahlung dose rate as a function of time.

The left bunch represents 140 shots, and right bunch represents 400 shots for a total of 540 laser shots on the Cu target with a starting peak intensity of 1.8×10^{18} W cm^{-2}. The drop in dose rates is linked with the progressive damage of the Al-coated OAP focusing mirror. In addition, the sudden dips in the dose rate are due to the target rastering system shifting the copper foil to provide a fresh row of material for laser shots. For future laser-solid experiments at MEC, the experimenters ensured the focusing mirror had the correct properties when paired with the 800 nm wavelength of the laser to sustain peak laser intensity over multiple laser shots.

5.4.2 July 2014, 1×10^{18} W cm^{-2}

The July 2014 laser-solid experiment with peak intensity of 10^{18} W cm^{-2} used three different solid foils: 5 μm Al, 15 μm Ni, and 100 μm Cu. No local shielding was

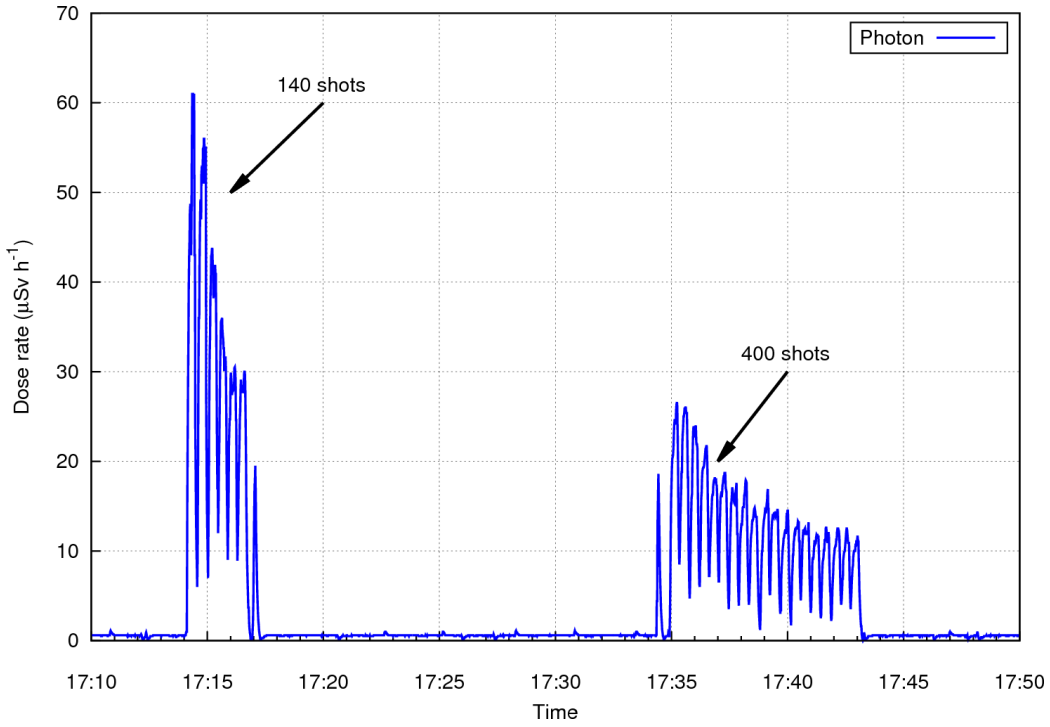

Figure 53: Bremsstrahlung dose rate (μSv h^{-1}) measured outside the target chamber at 1 m from the laser-target interaction point. Damage to focusing mirror during the February 2014 laser-solid experiment at MEC resulted in the incremental decrease in dose rate. Time is given in 24-hour format.

deployed inside the target chamber for this experiment. The bremsstrahlung dose rates measured outside the target chamber with background subtracted are shown in Figure 54. The dose rates measured at the two Al flanges(where viewports are located) at 23° from the forward and backward laser directions agree well. The same is evident at the chamber's doors at 0° and 45°. The bremsstrahlung dose rates of 30–50 μSv h^{-1} at the chamber's flanges are consistently higher by about a factor of 10 than the 4–5 μSv h^{-1} at the chamber doors. The Al wall thickness of the chamber is only 2 cm at the flanges, whereas the Al doors are between 5.08–6.4 cm thick. This difference in Al shielding accounts for the difference between photon dose rates.

The two ion chambers in the 0° forward direction measured about 5 μSv h^{-1} and 1 μSv h^{-1} at 1.4 m and 3.2 m distances from the laser-target interaction point, respectively, and the dose rate at 3.2 m is lower than at 1.4 m by a factor of $^1/_5$.

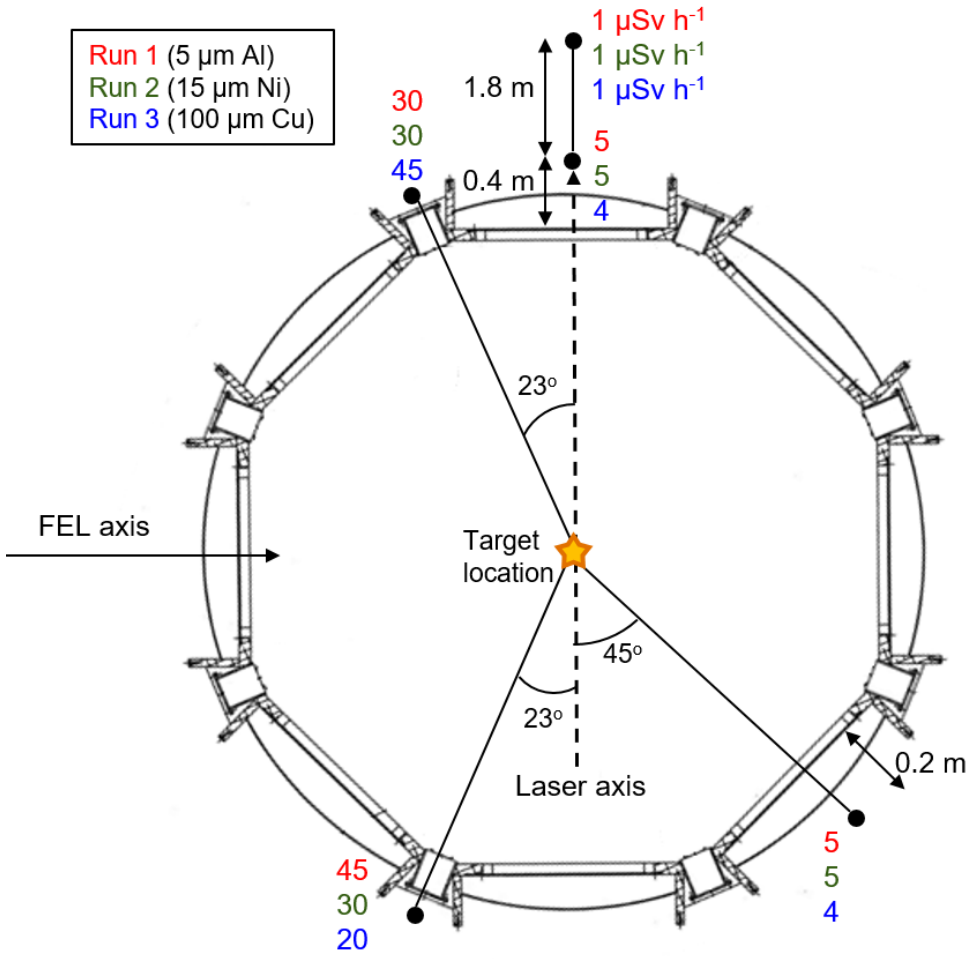

Figure 54: Bremsstrahlung dose rates (μSv h^{-1}) outside the target chamber from a laser with peak intensity of 10^{18} W cm^{-2} on solid foils during the July 2014 laser-solid experiment at MEC.

This behavior at 10^{18} W cm^{-2} operation suggests the photon dose falls off as $1/r^2$ and originates from the center of the target chamber whereas hot electrons interact with the solid target and generate bremsstrahlung.

Dependence on target material type (Cu, Ni, or Al) and target thickness (thick or thin) has little effect on the measured bremsstrahlung dose rates at 10^{18} W cm^{-2} outside the target chamber. No drastically elevated dose rates (within a factor of 2) were measured with the Ni nanowire compared to the Cu foils.

Figure 55 plots the dose rate over time from laser shots on the three target materials. The sudden dips in the dose rates are due to the target rastering system shifting to provide a fresh row of material for laser shots. The bremsstrahlung dose rates from about 20–40 μSv h^{-1} are consistent within a factor of 2 across the three target types although one can argue that dose rates are slightly higher for laser shots onto the thicker 100 μm Cu foil.

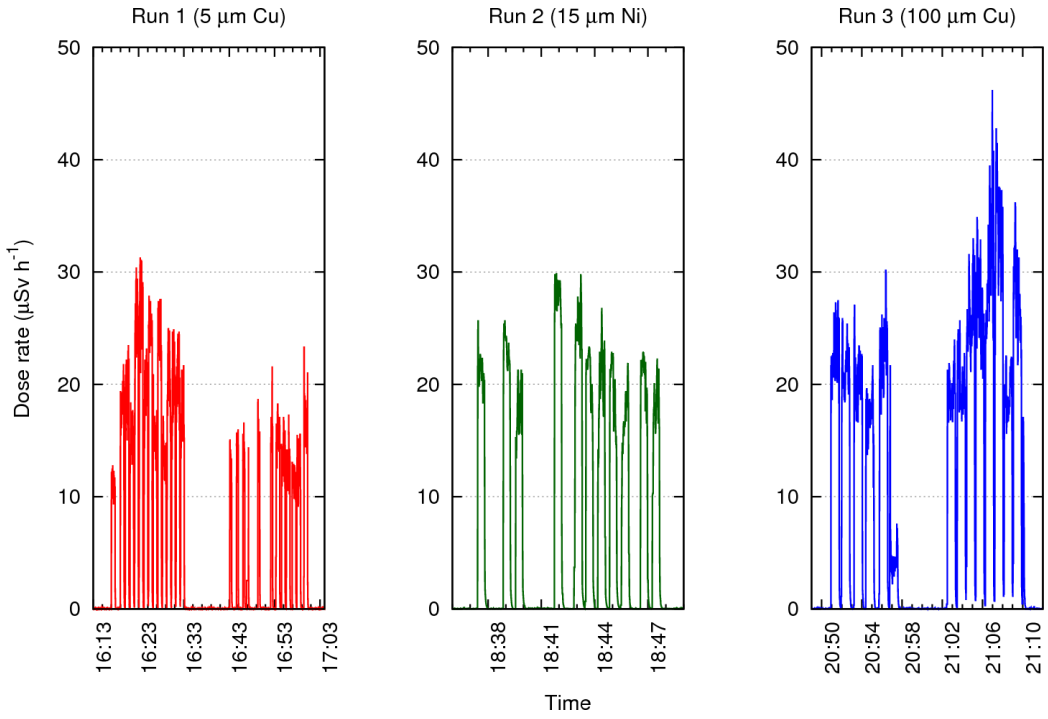

Figure 55: Bremsstrahlung dose rates (μSv h^{-1}) measured outside the target chamber at +23° from the laser forward axis. Dose rates generated from all three target types from the July 2014 experiment with a peak laser intensity of 10^{18} W cm^{-2} are shown for comparison.

5.4.3 August 2014, 1×10^{19} W cm^{-2}

Figure 56 shows the maximum bremsstrahlung dose rates measured by ion chambers outside the MEC target chamber from a laser-solid experiment in August 2014. Angles of particular interest were again those in the forward and backward direction of the laser beam. The peak laser intensity for the experiment was 10^{19} W cm^{-2}, and laser shots were delivered onto a 100 μm Cu foil and a 15 μm Ni nanowire target. As

expected, the dose rates for 10^{19} W cm^{-2} are higher than the previous two experiments (Figures 52 and 54) due to the increase in peak laser intensity by about a factor of 10.

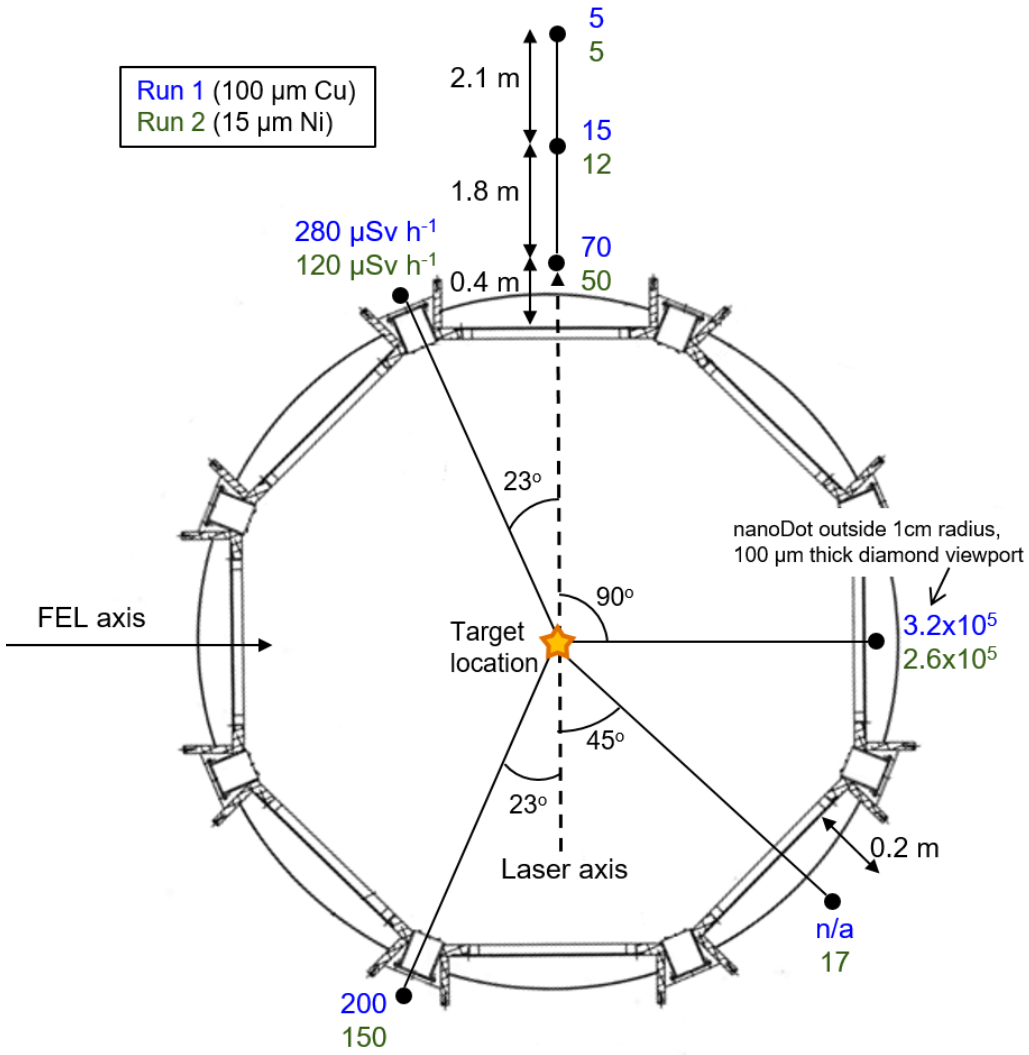

Figure 56: Bremsstrahlung dose rates (μSv h^{-1}) outside the target chamber from a laser with peak intensity of 10^{19} W cm^{-2} on solid foils during the August 2014 laser-solid experiment at MEC. The measurement at the diamond viewport has units of μGy h^{-1} for *absorbed* dose rate.

The bremsstrahlung dose rates are similar at the flanges at 23° in the forward and backward directions, and they are also consistently higher than the dose rates at the chamber's doors at 0° and 45°. Again, the difference in Al thickness between the

flanges (2 cm) and the doors (5.08–6.4 cm) account for the difference in dose rates due to attenuation. In the 0° laser forward direction, the photon dose rates for both runs fall off with distance as $1/r^2$.

Now at 10^{19} W cm^{-2}, the bremsstrahlung dose rates generated from laser shots on 100 μm Cu are consistently higher within about a factor of 2 at all locations than from shots on 15 μm Ni. Since the Cu ($Z = 29$) and Ni ($Z = 28$) targets have similar mass densities, the higher photon dose rate measured for Cu may be because the Cu target is a little more than six times thicker than the Ni target, such that hot electrons produced from laser-solid interactions simply interact with more material and generate more bremsstrahlung in the 100 μm Cu target than in the 15 μm Ni target. This effect may have been seen earlier in Figure 55 for 10^{18} W cm^{-2} but is now more pronounced for 10^{19} W cm^{-2}.

Also indicated in Figure 56 is a measurement made by the nanoDot dosimeter outside a small diamond view port with direct line of sight to the laser-target interaction location. The diamond view port was 100 μm thick with a radius of 1 cm and was located at 90° from the laser axis. Since the total number of shots and the laser repetition rate are known parameters, the integrated dose measured by the passive nanoDot dosimeter can be converted into an absorbed dose rate (μGy h^{-1}). The absorbed dose rate at the diamond viewport is very high because the 100 μm-thick diamond window provides little to no shielding. Recall, the measurement by the nanoDot can also be normalized 30 cm distance, converted to an absorbed dose per shot (mGy per shot) and compared to the measurements inside the target chamber (Figure 50).

Figure 56 shows the maximum photon dose rates measured by the ion chambers. The dose rates from the 15 μm-thick Ni target is consistently less than from the 100 μm Cu. Again, this difference may be due to greater radiation yield of Cu against Ni and also having more material for the hot electrons to interact with.

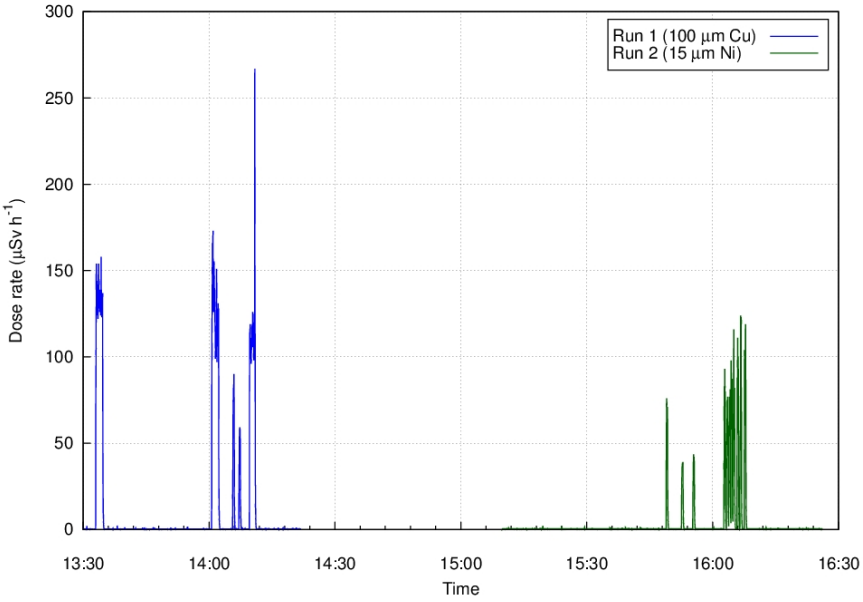

Figure 57: Bremsstrahlung dose rates (μSv h^{-1}) measured outside the target chamber at +23° from the laser forward axis. Dose rates generated from both target types from the August 2014 experiment are shown for comparison.

5.4.4 September 2014, 7.1×10^{19} W cm^{-2}

Radiation dose measurements in September 2014 at MEC were performed concurrent with a high-power laser experiment at 7.1×10^{19} W cm^{-2}. To mitigate the radiation hazard to personnel, two 2.54 cm thick W alloy (70% and 93%) shields were deployed in the forward and backward laser axis directions. Ion chambers were positioned around the target chamber and on its roof. The W shielding blocked the ion chamber in the forward direction of the laser at 6°. The shielding did not affect the other ion chambers. Figure 58 shows the maximum bremsstrahlung dose rates measured by the ion chambers during four experimental runs.

High-intensity laser shots were delivered continuously shots at 1 Hz onto the solid Al targets during Runs 1 and 3. The ion chambers at 90° and 68° measured very high photon dose rates of 2,060 and 2,740 μSv h^{-1} during run 1, and dose rates of 4,390 and 3,910 μSv h^{-1} during Run 3. Although the ion chamber located at 6° was shielded by the 2.54 cm-thick W alloy, it still measured 585 and 116 μSv h^{-1} in the

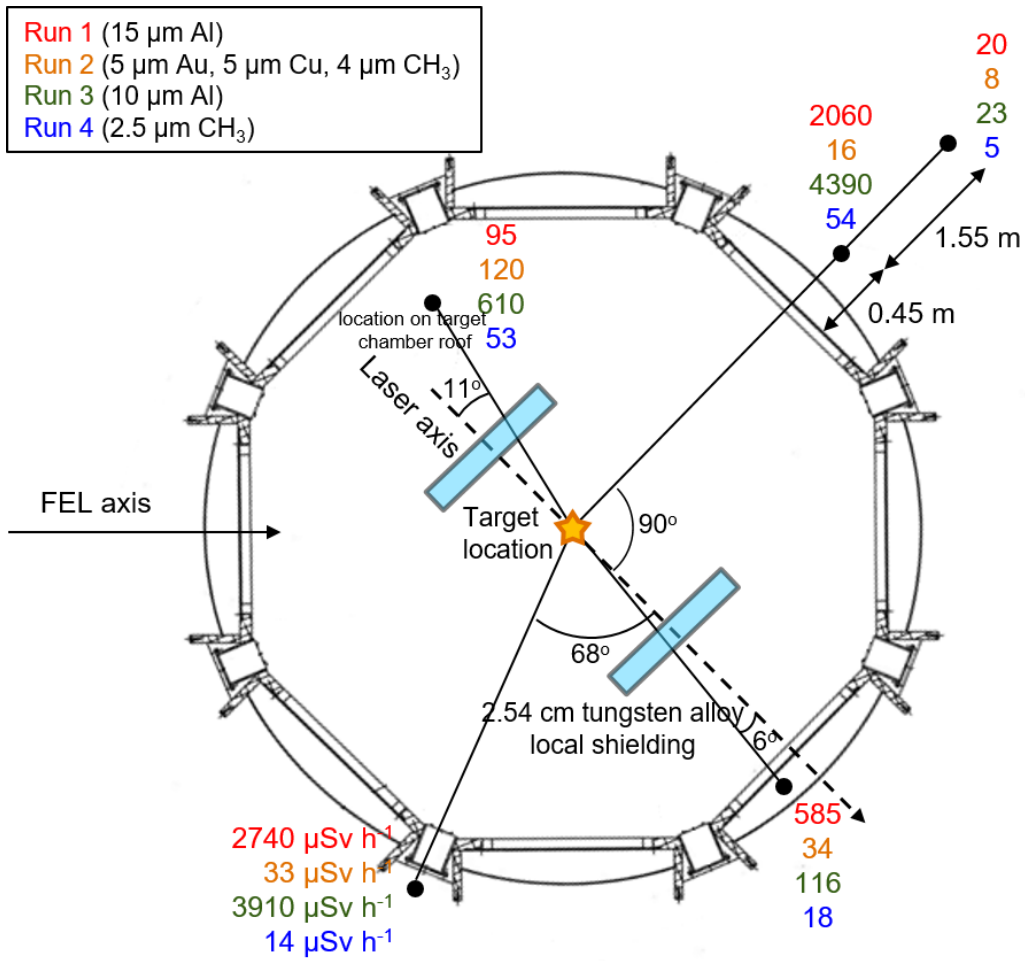

Figure 58: Bremsstrahlung dose rates (μSv h^{-1}) outside the target chamber from a laser with peak intensity of 7.1×10^{19} W cm^{-2} on solid foils during the September 2014 laser-solid experiment at MEC. Tungsten alloy shielding was deployed in the forward and backward laser directions during the experiment to mitigate dose to personnel.

laser forward direction.

Runs 2 and 4 during the September 2014 laser-solid experiment did not utilize the MEC laser's continuous 1 Hz repetition rate. Instead, the laser system delivered single laser shots (frequency separated by up to one or more minutes) onto the solid targets. The ion chambers did not respond well for shot-by-shot detection, and their dose rate readings under-responded during Runs 2 and 4 compared to Runs 1 and 3. For example, the ion chambers at 90° and 68° measured 16 and 33 μSv h^{-1} during run 2 and 54 and 14 μSv h^{-1} during run 4. In contrast, the ion chambers measured

in the thousands of μSv h^{-1} during Runs 1 and 3. The ion chambers also measured about an order of magnitude less dose rate during Runs 2 and 4 in the laser forward direction at 6° even with the 2.54 cm W alloy shielding.

The ion chamber deployed on the roof of the chamber measured a maximum dose rate of 610 μSv h^{-1}, which occurred during continuous laser shots on a 10 μm Al foil. Unlike the other locations around the chamber, the roof did not measure significantly less dose during Run 2. No $1/r^2$ behavior is observed between the ion chambers at 90° at 0.45 m and 1.55 m away from the chamber wall. Instead, the dose appears to drop off by at least a factor of 100 over the 1.55 m distance.

During Runs 2 and 4 of the September 2014 experiment at MEC, experimenters attempted to deliver high-intensity laser shots onto a jet of liquid hydrogen but experienced difficulty in successfully hitting the 5 μm diameter jet. The few successful shots on the LH_2 jet did generate a measurable bremsstrahlung reading in the ion chambers outside the target chamber but were up to a factor of 10 lower than the dose rates from solid targets.

5.4.5 Summary of bremsstrahlung dose yields

Figure 59 summarizes the bremsstrahlung dose yield measurements at SLAC's MEC laser facility taken over the course of this dissertation. In addition, measurement data from an experiment at MEC in 2012 and at LLNL's Titan laser facility in 2011 are also included. These bremsstrahlung dose yield measurements were shown earlier in Figure 27 without uncertainties to reduce the visual clutter when comparing to the dose yield curves.

Bremsstrahlung dose yield measurements at the LLNL's Titan laser facility in 2011 were taken parasitically to another experiment by SLAC before the start of this dissertation, and characterization of laser parameters at the time were not as robust as at SLAC's MEC laser facility. Take note in Figure 59 that an overall improvement in

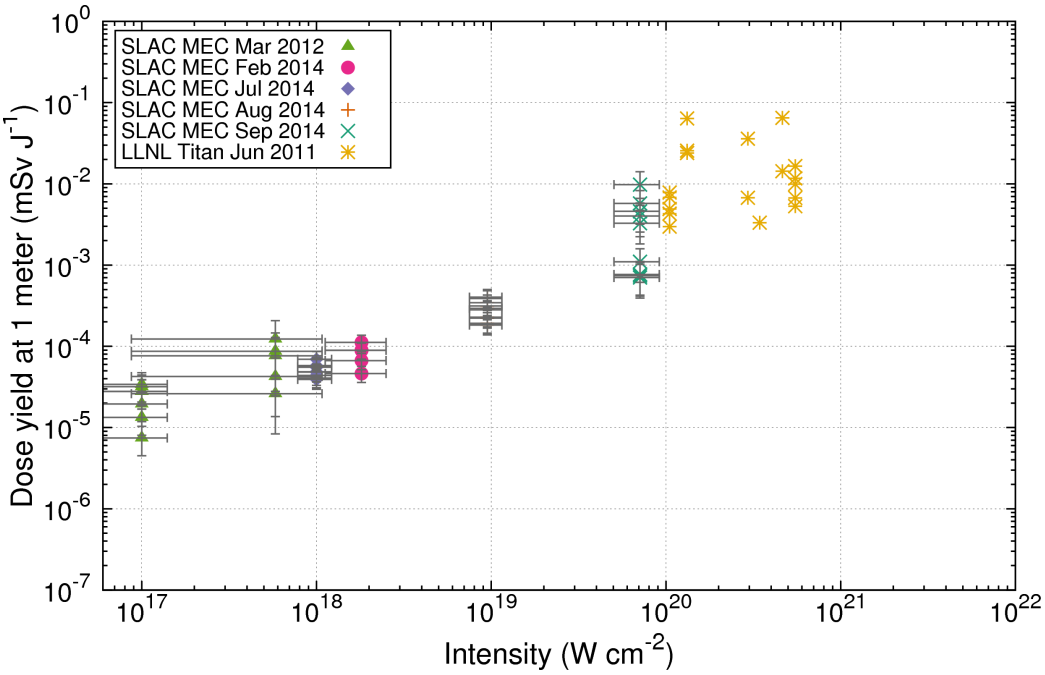

Figure 59: Measurement data of bremsstrahlung dose yield SLAC MEC and Titan LLNL. The measurements were taken outside the target chamber at varying angles and elevation (hence, the vertical spread). Differences between the model and measurements are due to target chamber attenuation, measurement angle, target Z, target thickness, detector sensitivity, and uncertainties in the laser beam characterization..

laser characterization by the laser facility staff at MEC led to a decrease in uncertainty from 2012 to 2014.

Uncertainties in measurement data were calculated using the error propagation method for multiplication of measured quantities. Uncertainties in the laser intensity (x-axis) are due to the uncertainties in the laser parameters ($\pm$ variation) such as pulse energy, pulse length, and spot size. The inherent detector uncertainty was estimated to be about 20% and combining this with the uncertainty in the laser pulse energy on target yields the y-axis uncertainty. Tables 5 and 6 provide examples of the error propagation calculation for the July 2014 and August 2014 laser-solid experiments at the MEC laser facility.

Table 5: Summary of laser parameters from the high-intensity laser-solid experiment at SLAC's MEC during July 2014. A fraction of 0.77 of the laser energy was within the main peak of the laser.

Laser parameters	July 2014
FWHM pulse length (fs)	50 ± 5 (10%)
Laser pulse energy (J)	0.7 ± 0.1 (14%)
Total laser power (TW)	14 ± 2.4 (17%)
Horizontal $1/e^2$ radial spot size (μm)	37 ± 2.2 (6%)
Vertical $1/e^2$ radial spot size (μm)	19 ± 2.2 (12%)
Peak laser intensity (W cm^{-2})	$(1.0 \pm 0.2)10^{18}$ (22%)

Table 6: Summary of laser parameters from the high-intensity laser-solid experiment at SLAC's MEC during July 2014. A fraction of 0.44 of the laser energy was within the main peak of the laser.

Laser parameters	August 2014
FWHM pulse length (fs)	50 ± 5 (10%)
Laser pulse energy (J)	0.7 ± 0.1 (14%)
Total laser power (TW)	14 ± 2.4 (17%)
Horizontal $1/e^2$ radial spot size (μm)	9.2 ± 0.45 (5%)
Vertical $1/e^2$ radial spot size (μm)	4.4 ± 0.45 (10%)
Peak laser intensity (W cm^{-2})	$(1.0 \pm 0.2)10^{19}$ (21%)

5.5 Neutron dose measurements

Polyethylene-moderated tubes filed with BF_3 gas (designed in-house at SLAC) were deployed around the target chamber and measured the neutron fluence generated from laser-solid experiments at MEC. Neutrons are produced primarily from photonuclear (γ, n) interactions when high energy bremsstrahlung from hot electrons interact with the target material or the chamber walls.

The BF_3 neutron detectors were calibrated with an 11 GBq PuBe neutron source and compared to the ambient neutron dose equivalent rate measured by a Model 5085 Meridian neutron survey meter. A conversion factor is derived for each BF_3 detector to convert the neutron fluence to ambient dose equivalent of neutrons. A typical conversion factor for a BF_3 is about 10^5 counts per μSv.

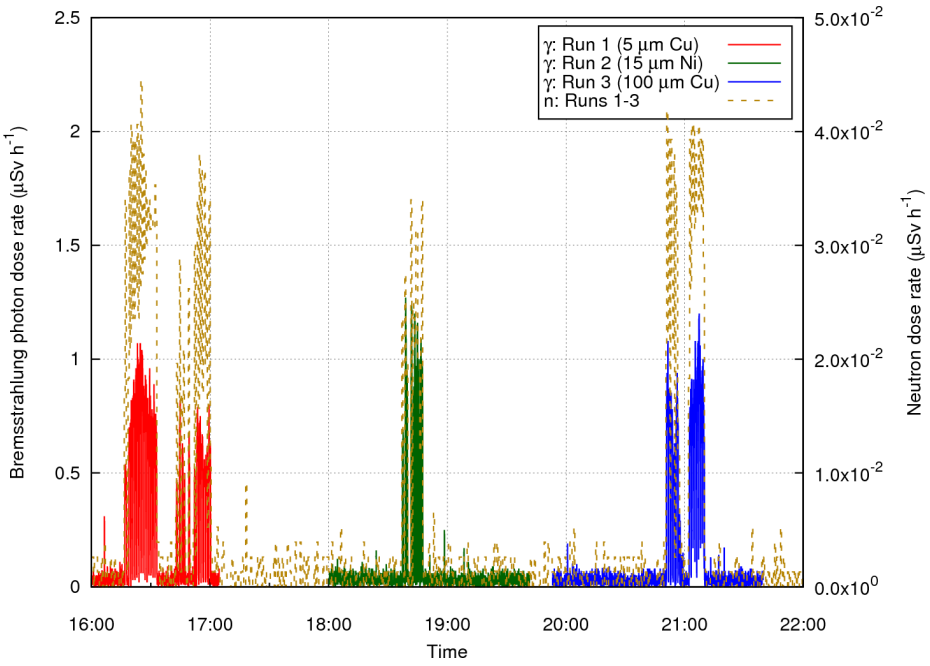

Figure 60: Concurrent bremsstrahlung and neutron dose rate (μSv h^{-1}) measurements at 3.3 m from the laser-target interaction point and +0° relative to the laser forward direction. Measurements were performed during the July 2014 laser-solid experiment at MEC with peak laser intensity of 10^{18} W cm^{-2}. Note the different scales for bremsstrahlung photons and neutrons.

Figure 60 shows an example of the measurements performed by both a BF_3 neutron detector and a Victoreen 451P ion chamber. The plot shows that whenever the ion chambers measured photons, the BF_3 also measured neutrons at the same time. In addition, the instruments showed that a neutron dose rate of about 3–4$\times10^{-2}$ μSv h^{-1} was consistently generated from a bremsstrahlung dose rate of about 1 μSv h^{-1}.

The ambient neutron dose equivalent rates (μSv h^{-1}) measured by BF_3 detectors can be normalized into a neutron dose yield (μSv J^{-1}) since laser beam parameters such as laser repetition rate and pulse energy are known. Figure 61 shows the neutron dose yields normalized to a distance of 1 meter from laser-solid interactions. The original distance from the laser-target interaction point and the angle relative to the laser axis is labeled by each data point. The March 2012 measurement at MEC is detailed by Bauer *et al.* in 2013.[6]. The data suggests the neutron dose yield

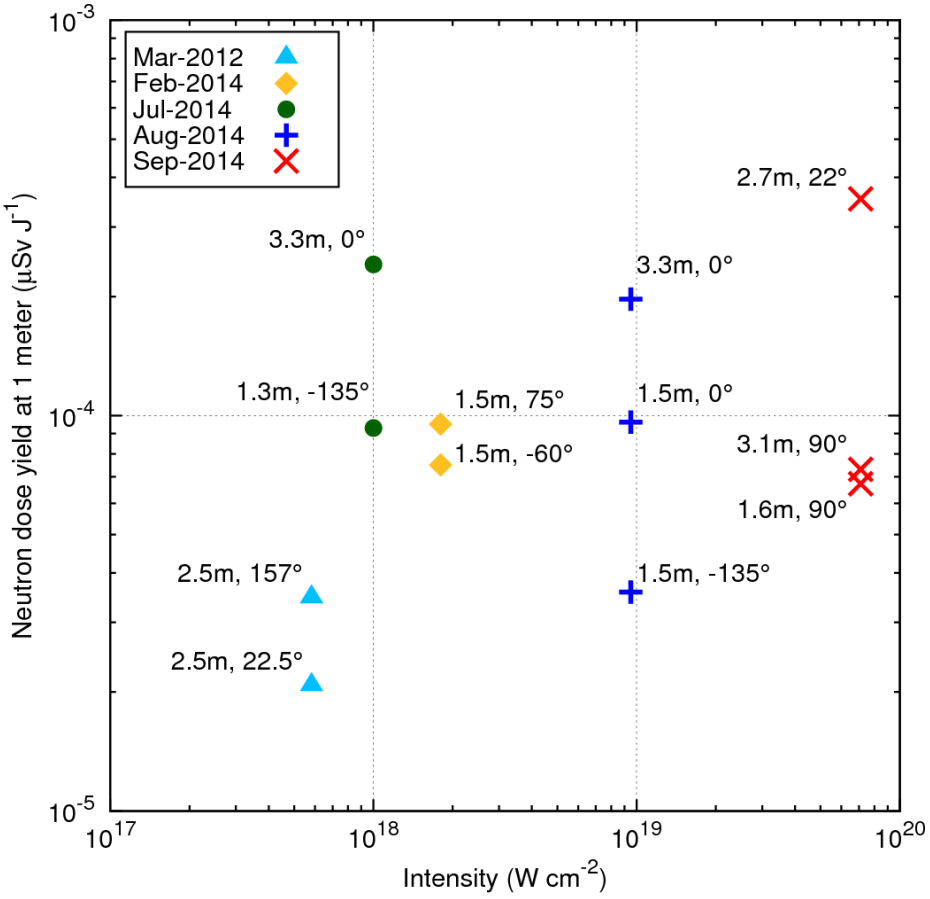

Figure 61: Neutron dose yield (μSv J^{-1}) as a function laser intensity and normalized to a distance of 1 m from laser-solid experiments at MEC. The original distance from the laser-target interaction point and the angle relative to the laser axis is labeled by each data point.

increases with laser intensity, which is expected. The prompt neutron dose rate is small compared to the prompt photon dose rates, but at higher intensities, it has the potential to activate equipment inside and around the target chamber.

5.6 Electron spectra measurements

Measurements of electron spectra with electron spectrometers (based on a depth dose curve approach) were performed during several laser-solid experiments at the MEC laser facility. The spectrometers were placed inside the target vacuum chamber at various angles relative to the laser beam direction and at a distance of 30 cm from the laser's target. Care was taken to ensure the front face of the spectrometer had

a direct line-of-sight to the laser's target. The spectrometer will measure dose from both electrons and bremsstrahlung photons inside the target chamber. However, the dose deposited in the spectrometer is dominated by electrons (up to three orders of magnitude higher). Evidence of this will be presented with FLUKA simulations.

An electron spectrometer (Figure 62) consisted of seven alternating layers of nanoDot dosimeters (2-mm-thick) and Plexiglas (3-mm-thick, 1.18 g cm^{-3}). The Plexiglas layers attenuate the incident electrons from the high-intensity laser-solid interactions. The dose deposited in the dosimeter layers are then plotted as a function of depth of attenuating material to provide insight into the energy distribution of hot electrons.

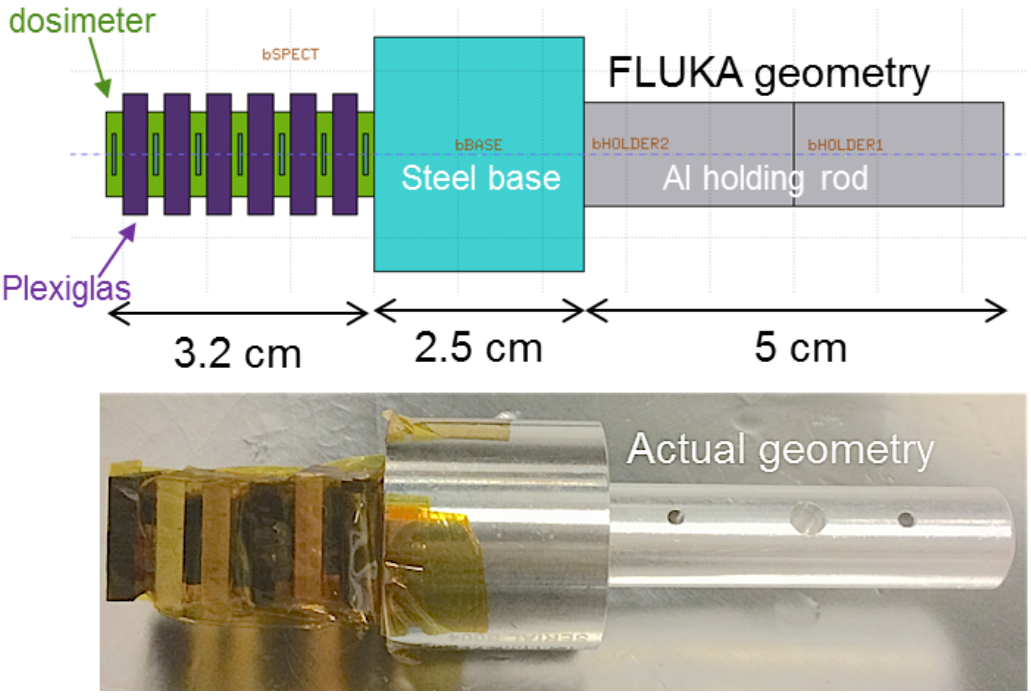

Figure 62: The electron spectrometer consisted of seven alternating layers of Plexiglas and Landauer nanoDot dosimeters. Each Plexiglas layer is 1.5 cm × 1.5 cm in size with a thickness of 3 mm, and the dosimeter is 1 cm × 1 cm in size with a thickness of 2 mm. Electrons enter the spectrometer from left to right, are attenuated by the Plexiglas, and deposit dose in the dosimeters.

The depth-dose response of the electron spectrometers in Figure 62 was also simulated with FLUKA. The spectrometer was exposed to a hot electron energy spectrum

with temperature T_h associated with the laser intensity from the MEC experiment. Matching experimental conditions, the hot electrons in FLUKA first interacted with a thin metal foil. The hot electron temperature T_h (MeV) was previously found to increase with laser intensity I (W cm^{-2}) as given in Equation 23.[42]

$$T_h = 1.05 \times 10^{-10}\ I^{0.514} \tag{23}$$

Two types of energy distributions were used in FLUKA for the hot electrons. The Maxwellian distribution of Equation 11, and the relativistic Maxwellian distribution of Equation 12 were used for comparison. The relativistic Maxwellian is a harder energy spectrum with an average energy of $3 \times T_h$ compared with $1.5 \times T_h$ for the Maxwellian. Both distributions have been used in numerous studies to estimate the hot electron source.[37,11,30,40]

FLUKA simulations scored the dose deposited in the layers, and depth-dose curves were generated. The plots in Figure 63 show the depth-dose curves from these FLUKA simulations, which are labeled in the legend with the type of energy distribution used as the hot electron source term. For a given laser intensity, both energy distributions had the same hot electron temperature T_h.

The electron spectrometry depth-dose data from the two respective laser-solid experiments at MEC are also plotted in Figure 63, and the angles in the legend indicate the location of the electron spectrometer relative to the laser direction. The dose is plotted relative to the maximum dose (i.e., the dose of the unshielded, 1st dosimeter). Despite varying angles and even target material types, the shapes of the depth-dose curves all have similar profiles within each MEC experiment. This suggests that the energy spectrum of hot electrons ejected from the plasma during laser-solid interactions does not significantly depend on the emission angle.

As expected, the temperature of the hot electron energy spectra depends on the laser intensity. Using the scaling in Equation 23, the T_h of the hot electron energy spectra increases with laser intensity from 0.61 MeV to 1.65 MeV (10^{19} W cm^{-2}

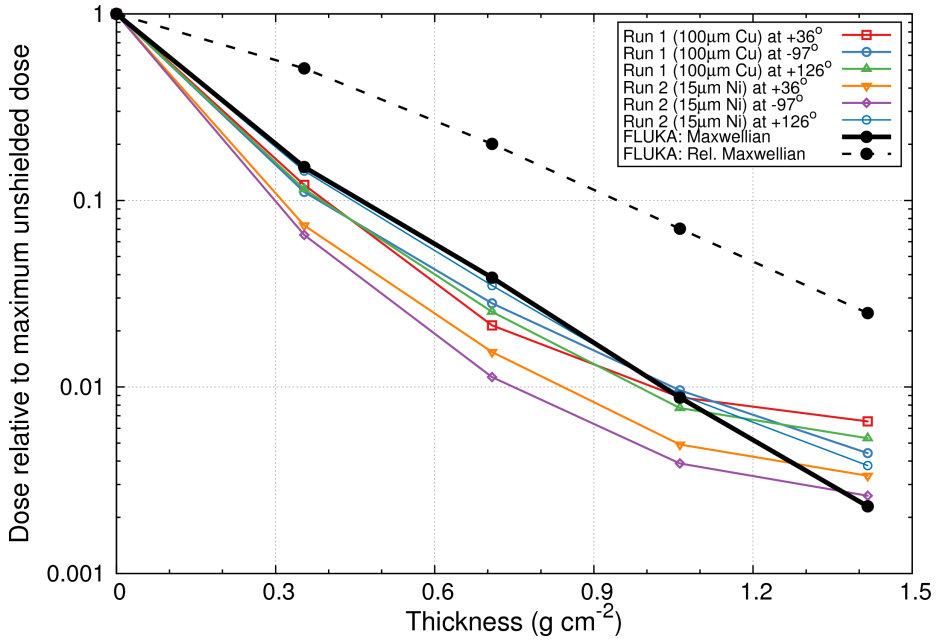

(a) August 2014 MEC experiment (10^{19} W cm^{-2}).

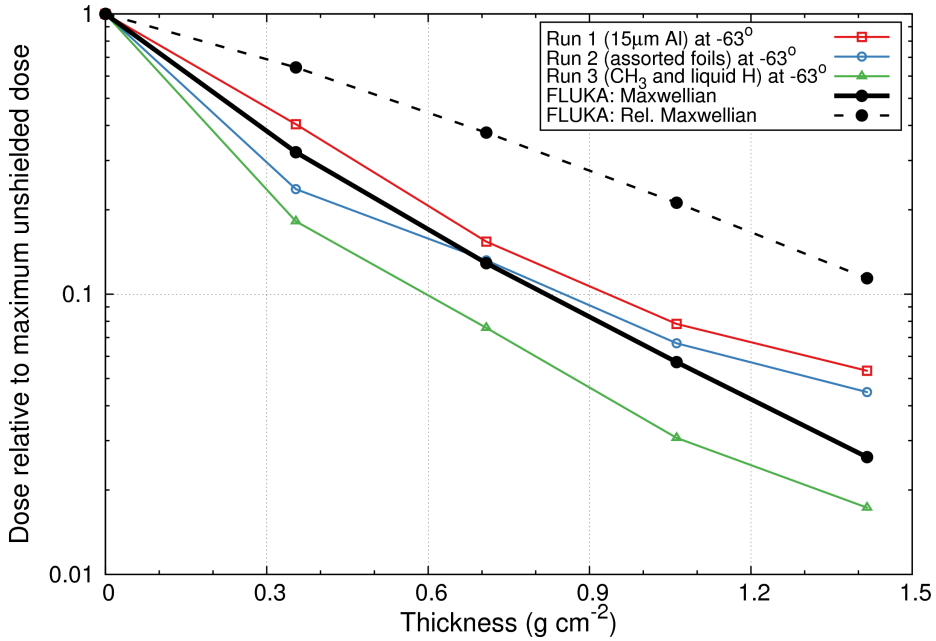

(b) September 2014 MEC experiment (7×10^{19} W cm^{-2}).

Figure 63: Electron spectrometry measurements from August 2014 and September 2014 laser-solid experiments at MEC.[40] FLUKA simulations used a Maxwellian and Relativistic Maxwellian distribution of hot electrons with T_h chosen from the actual experiments' laser intensities. Angles indicate the location of the electron spectrometer relative to the laser direction.

to 7×10^{19} W cm^{-2}, respectively) for the two MEC experiments. This leads to a 'shallower' slope for the depth-dose curve with increasing laser intensity as seen in Figure 63(b).

For both Figures 63(a) and 63(b), the FLUKA-calculated depth-dose curve from a Maxwellian hot electron source agrees better with the measurement data than the one from a relativistic Maxwellian. Even if an artificial lower T_h was chosen for the relativistic Maxwellian source, it would still not fit the data as well. This agreement also confirms the PIC simulation conclusions (Ref. 42) that 1) the hot electron energy spectra from high-intensity laser-solid interactions is better described with a Maxwellian distribution and 2) the temperature versus laser intensity relationship in Equation 23.

5.7 Simulation of experiment from hot electron source

The FLUKA code can calculate the ambient dose equivalent $H^*(10)$ of bremsstrahlung photons generated from hot electrons interacting with the target material and target chamber. This simulation allows for comparison with radiation dose measurement at the MEC laser facility by modeling the full target chamber geometry in FLUKA and using a hot electron source based on the experiment's peak laser intensity. This study provides additional confirmation on bremsstrahlung dose yield of the hot electron source term characterized earlier in this dissertation with EPOCH.

The laser-solid experiment at MEC during August 2014 took measurements with a laser beam that interacted at a peak intensity of 10^{19} W cm^{-2} with 100 μm Cu foils.[40] For this laser intensity, EPOCH characterized the hot electron source term as electrons with a Maxwellian energy distribution and temperature T_h of 0.61 MeV, a Gaussian angular distribution with σ of 45°, a forward-to-backward emission ratio of 1.3, and a laser-to-electron energy conversion efficiency of $\eta = 0.51$.

Figure 64 shows the bremsstrahlung dose yield (mSv J^{-1}) at the target plane as

simulated with FLUKA using the hot electron source term described above. The hot electrons interact with the 100 μm Cu foil at the center of the target chamber (radius of about 1 m) and generate bremsstrahlung. The target chamber wall has varying thicknesses of Al, and glass view ports are located every 22.5°.

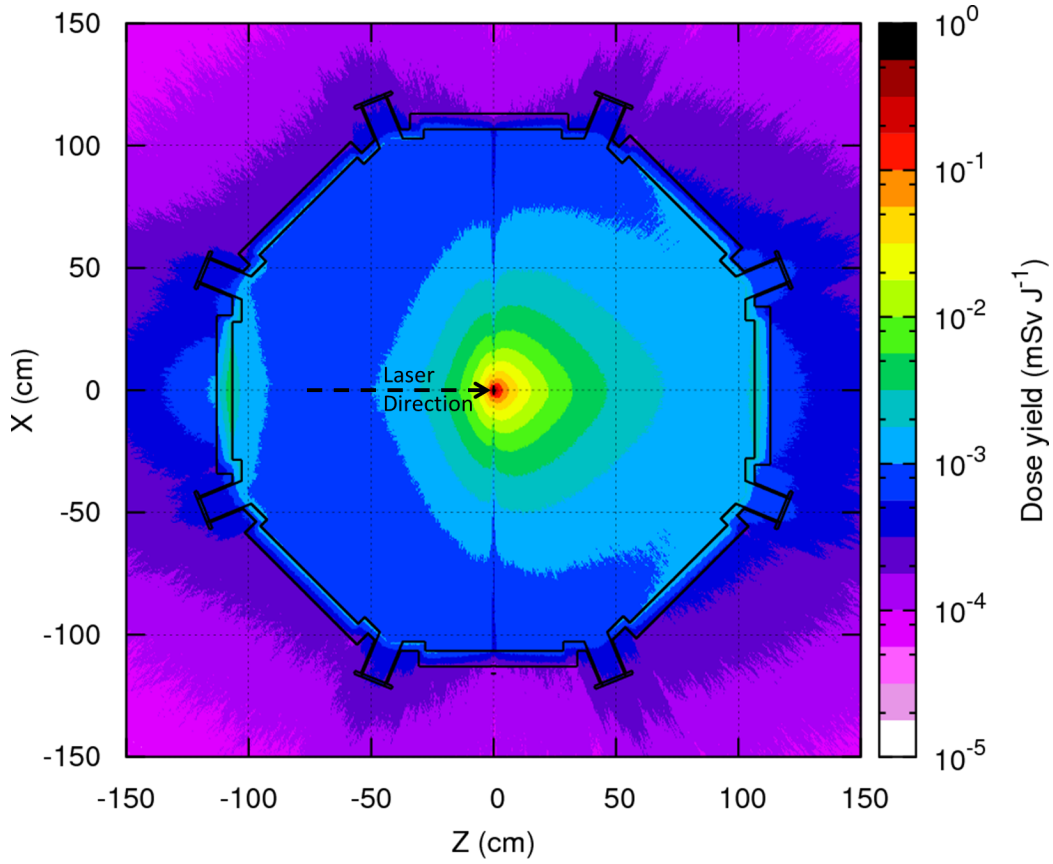

Figure 64: Bremsstrahlung photon dose yield (mSv J^{-1}) at the target plane calculated with FLUKA for the MEC laser-solid experiment in August 2014.[40] The laser with intensity 10^{19} W cm^{-2} traveled from 'left-to-right' in the Z-direction and interacted with the 100 μm Cu foil located at the center of the target chamber.

Bremsstrahlung dose from the hot electrons interacting with the target is peaked along the laser beam direction (+Z). A fraction of the hot electrons also escape the 100 μm-thick target and generate additional bremsstrahlung when interacting with the Al chamber wall. This is most obvious in Figure 64 in the laser backward (–Z) direction where unattenuated hot electrons stream out of the backside of the Cu foil and generate bremsstrahlung with the target chamber's Al wall.

Figure 65 plots the 360° dose yield profile inside the target vacuum chamber at 0.3 m from the target: $H^*(10)$ of electrons separated from that of bremsstrahlung photons. As can be seen, the dose inside the chamber is dominated by hot electrons unattenuated by thin 100 μm Cu target, and the electron dose yield is between a factor of 10 (90°) and 1000 (0°, 180°) higher than the bremsstrahlung photon dose yield. The electron spectrometers earlier from Figure 63(a) were exposed to this mixed field of electrons and photons.

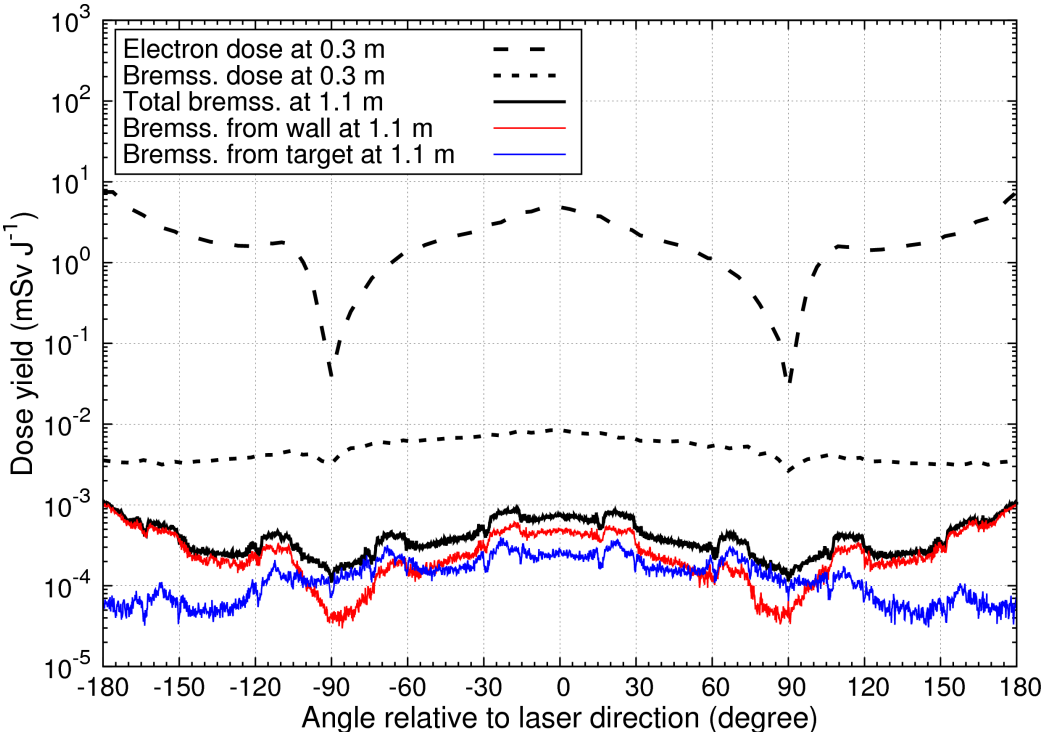

Figure 65: The electron dose yield is dominant over the bremsstrahlung photon dose yield inside the target vacuum chamber at 0.3 m. Outside the target chamber at 1.1 m, the bremsstrahlung dose yield has a component generated from hot electrons interacting with the target itself and another from unattenuated hot electrons interacting with the target chamber's Al wall.

The bremsstrahlung photon dose yield outside the target chamber at 1.1 m from the target is also shown in Figure 65. The high electron dose inside the target chamber does not escape the target chamber, and instead it is attenuated and also converted into bremsstrahlung photons upon interaction with the Al wall of the target chamber.

Therefore, the bremsstrahlung dose yield outside the target chamber has a component generated from the target itself and another from the Al wall. For the majority of the angles, the bremsstrahlung dose generated from hot electrons (unattenuated by the thin foil) interacting with the Al walls is higher except at around 90°.

In addition, the 360° bremsstrahlung dose yield profiles outside the target chamber at 1.5 m from the target was extracted from Figure 64 and plotted in Figure 66 as a function of angle relative to the laser direction. The bremsstrahlung dose yield at 1.1 m from Figure 65 was again plotted for comparison. These distances from the target correspond to distances of detector locations.

The 0° angle (laser forward direction) and the ±180° angles (laser 'backward' direction) have peaked radiation doses about 10 times higher than those at ±90°. This angular dose pattern is because the hot electron source has an an-isotropic angular distribution and is peaked along the laser direction. In addition, the MEC target chamber has non-uniform Al wall thickness and glass viewports every 22.5°, which produce a non-smooth dose curve. Also plotted for comparison are dose measurements taken with active ion chambers (Victoreen 451P and HPI-6031) and passive ion chambers (Arrow-Tech Model 2 pocket dosimeters) that were deployed outside of the target vacuum chamber at various angles and distances during the experiment at MEC.

The measurement data in Figure 66 agree well with the angular profile of the FLUKA-calculated dose yield curve, peaking as the angle approaches 0° and ±180°. However, all measurements are below the calculated curves because the FLUKA calculations used optimal dose yield parameters for all laser shots and does not account for shot-by-shot variations in the laser intensity present during the experiment. Considering the uncertainties involved (e.g., shot-by-shot laser variation, detector energy response, and non-uniform chamber wall), FLUKA simulations with the hot electron source term in this dissertation are consistent with the dose measurements and can

be used for estimating the bremsstrahlung dose yield from high-intensity laser-solidi interactions

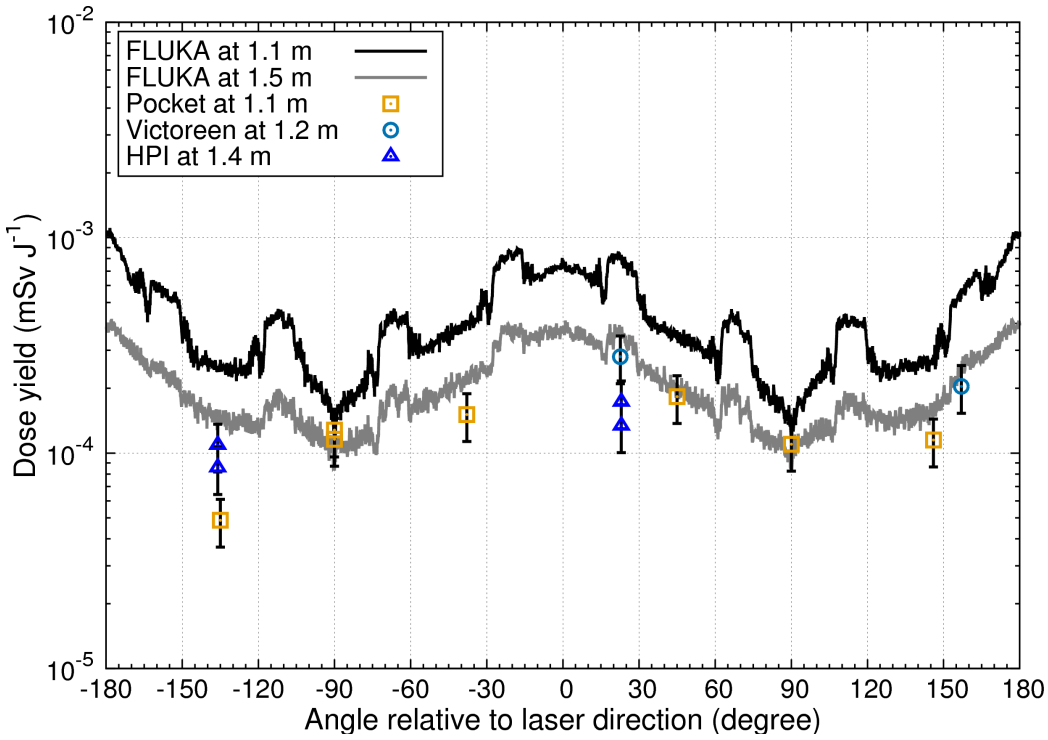

Figure 66: Comparison of the bremsstrahlung dose yield profile from FLUKA with measurement data from the MEC laser-solid experiment during August 2014 (10^{19} W cm^{-2}). Dose yields around the outside of the target chamber and at various distances from the laser target are plotted as a function of angle. The measurement points are from active (Victoreen and HPI) and passive (pocket) ion chambers that were deployed outside the MEC target chamber at various angles and distances.

CHAPTER VI

CONCLUSION

High-intensity laser facilities have seen rapid growth over the past two decades with experimenters pushing the laser systems to higher powers and high intensities. Laser-matter interactions are used to explore matter under extreme conditions, produce highly energetic beams of electrons and ions, generated beams of X-rays, and explore inertial confinement fusion. However, the radiation protection of these laser facilities is necessary to mitigate the ionizing radiation hazards to personnel.

In this dissertation, the hot electron source term from laser-solid interactions has been characterized with the plasma physics code EPOCH. The hot electrons have a Maxwellian energy distribution with temperature T_h, a Gaussian angular distribution with σ of 45°, and a laser-to-electron conversion efficiency that increases with laser intensity up to 60%. Radiation dose calculations with FLUKA that fully utilize the characterized hot electron source term have been performed to estimate the bremsstrahlung photon dose yield (mSv J^{-1}) as a function of laser intensity from such laser-solid interactions. Comparison with radiation measurement data performed at SLAC's Matter in Extreme Conditions (MEC) laser facility showed good agreement and confirmed the simulation results.

For the first time, a bremsstrahlung dose yield source term for laser-solid interactions has been developed by coupling a plasma code with a radiation transport code. This source term combined with the tenth-value layer (TVL) shielding calculations provide a guideline for radiation protection and hazard analysis for laser-solid interactions between 10^{17} and 10^{22} W cm^{-2} at high-intensity laser facilities both at SLAC and around the world.

Funding

The EPOCH code used in this work was in part funded by the UK EPSRC grants EP/G054950/1, EP/G056803/1, EP/G055165/1 and EP/M022463/1.

The material in this dissertation is based upon work supported by the U.S. Department of Energy, Office of Science, Office of Basic Energy Sciences, under Contract No. DE-AC02-76SF00515.

APPENDIX A

EXAMPLE OF EPOCH INPUT

```
################
### COMMENTS ###
################

# EPOCH2D v4.5.0
# 0.4 um, 1e20 W/cm2, 10nc
# 31 October 2016

######################
### CONSTANTS BLOCK ###
######################

begin:constant
# number of macro-particles to initialize
macropart = 2e6

# plasma critical density 1/m^3
nc = 1.74e27

# Z-number of target material
#targZ = 13.0 # Al
targZ = 29.0 # Cu
#targZ = 79.0 # Au

# parameters of laser beam
wavelength = 0.4 * micron
theta = 0.0
intensity0 = 1e20 #W/cm^2
duration0 = 40 * femto #FWHM
plength = 1.6986436 / 2 * duration0 #1/e^2 spot
#waist = 2 * wavelength  #FWHM spot
#spot = waist / 2.35482  #1/e2 spot
spot = 4 * micron

# time steps of simulation
dt = 10 * femto
full_dt = 10
stept = 40

# density ramp parameters
rampN0 = 0.0127
rampNX = 10
startX = 0 * micron
deltaX = 8 * micron
scaleL = deltaX/loge(rampN0/rampNX)
ratioL = scaleL/wavelength
end:constant

####################
### CONTROL BLOCK ###
####################

begin:control
nx = 400
ny = 400
t_end = stept * dt
x_min =   0*micron
x_max =  20*micron
```

```
y_min = -10*micron
y_max =  10*micron
field_ionisation = F
print_constants = T
stdout_frequency = 10
#use_random_seed = T
end:control

######################
### BOUNDARY BLOCK ###
######################

begin:boundaries
bc_x_min = simple_laser
bc_x_max = simple_outflow
bc_y_max = periodic
bc_y_min = periodic
end:boundaries

######################
### SPECIES BLOCKS ###
######################

begin:species
name = Ion
charge = 1.0
mass = 1836.2 * targZ
npart = macropart/2
rho = if((x gt 0*micron) and (x lt  8*micron) and (y gt -10*micron) and
            (y lt 10*micron), nc*rampN0*exp(-1*(x-startX)/scaleL), 0)
rho = if((x gt 8*micron) and (x lt 12*micron) and (y gt -10*micron) and
            (y lt 10*micron), rampNX*nc , rho(Ion))
end:species

begin:species
name = Electron
charge = -1.0
mass = 1.0
npart = macropart/2
rho = if((x gt 0*micron) and (x lt  8*micron) and (y gt -10*micron) and
            (y lt 10*micron), nc*rampN0*exp(-1*(x-startX)/scaleL), 0)
rho = if((x gt 8*micron) and (x lt 12*micron) and (y gt -10*micron) and
            (y lt 10*micron), rampNX*nc , rho(Electron))
end:species

####################
### LASER BLOCK ###
####################

begin:laser
boundary = x_min
intensity_w_cm2 = intensity0
lambda = wavelength
#lambda = wavelength * cos(theta)
#phase = -2.0 * pi * y * sin(theta) / wavelength
#pol_angle = 0 #pi/2.0
profile = gauss(y, 0, spot)
t_profile = gauss(time, 2.5 * plength, plength)
end:laser

####################
### OUTPUT BLOCK ###
####################

begin:output
```

```
dt_snapshot = dt
full_dump_every = stept

# Particle variables
particles = always
px = always + single
py = always + single
particle_energy = always + single
particle_weight = always + single
#gamma = always + single

# Grid variables
#grid = always
#ey = always
#bz = always

# Derived grid variables
#ekbar = always + species + single
#ekflux = always + species + single
number_density = always + species + single

# Other variables
particle_probes = full
absorption = always
total_energy_sum = always
end:output

####################
### PROBE BLOCKS ###
####################

begin:probe
name = eprobe_down
point = (8*micron, 0.0)
normal = (1.0, 0.0)
ek_min = 0.0
ek_max = -1.0
include_species:Electron
dumpmask = full
end:probe

begin:probe
name = eprobe_up
point = (4*micron, 0.0)
normal = (-1.0, 0.0)
ek_min = 0.0
ek_max = -1.0
include_species:Electron
dumpmask = full
end:probe
```

APPENDIX B

EXAMPLE OF FLUKA INPUT

```
TITLE
MEC 2014-08 Run 1: 100um Cu  (1e19 W/cm2, Th=0.68 MeV)
* --+----1----+----2----+----3----+----4----+----5----+----6----+----7----+----8
DEFAULTS                                                              PRECISIO
*
* --+----1----+----2----+----3----+----4----+----5----+----6----+----7----+----8
BEAM           -0.05      0.02   -1850.0       0.0       0.0       1.0ELECTRON
BEAMPOS          0.0       0.0     0.001       0.0       0.0
SOURCE         680.0      45.0       1.3
*
* --+----1----+----2----+----3----+----4----+----5----+----6----+----7----+----8
* ==Rotate geometries to align with beam axis
ROT-DEFI        101.       0.0      90.0       0.0       0.0          alignZ
ROT-DEFI        200.       0.0      90.0       0.0       0.0          alignZ
*
* --+----1----+----2----+----3----+----4----+----5----+----6----+----7----+----8
GEOBEGIN                                                              COMBNAME
0    0          Hutch 6 MEC
$start_transform alignZ
RPP blkhole    -1000.0 1000.0 -1000.0 1000.0 -1000.0 1000.0
RPP hall       -200.0 200.0 -200.0 200.0 -70.0 150.0
* ==Planes of inside of the chamber body
PLA bp_i1      1.0 0.0 0.0 102.87 0.0 0.0
PLA bp_i2      1. 1. 0.0 72.74 72.74 0.0
PLA bp_i3      0.0 1.0 0.0 0.0 102.87 0.0
PLA bp_i4      -1. 1. 0.0 -72.74 72.74 0.0
PLA bp_i5      -1.0 0.0 0.0 -102.87 0.0 0.0
PLA bp_i6      -1. -1. 0.0 -72.74 -72.74 0.0
PLA bp_i7      0.0 -1.0 0.0 0.0 -102.87 0.0
PLA bp_i8      1. -1. 0.0 72.74 -72.74 0.0
* ==Planes of outside of the chamber body
PLA bp_o1      1.0 0.0 0.0 106.68 0.00 0.0
PLA bp_o2      1.0 1.0 0.0 75.41 75.41 0.0
PLA bp_o3      0.0 1.0 0.0 0.00 106.68 0.0
PLA bp_o4      -1.0 1.0 0.0 -75.41 75.41 0.0
PLA bp_o5      -1.0 0.0 0.0 -106.68 0.00 0.0
PLA bp_o6      -1.0 -1.0 0.0 -75.41 -75.41 0.0
PLA bp_o7      0.0 -1.0 0.0 0.00 -106.68 0.0
PLA bp_o8      1.0 -1.0 0.0 75.41 -75.41 0.0
* ==Top and bottom planes of the chamber body
XYP bp_t       46.18
XYP bp_b       -46.18
* ==Bottom plate 4 inches
RCC bottom     0.0 0.0 -56.34 0.0 0.0 10.2 118.1
* ==Body door opens
BOX do1 102.77 -27.92 -38.97 4.21 0.0 0.0 0.0 56.4 0.0 0.0 0.0 77.95
BOX do2 92.42 52.93 -38.97 2.98 2.98 0.0 -39.88 39.88 0.0 0.0 0.0 77.95
BOX do3 27.92 102.77 -38.97 0.0 4.21 0.0 -56.4 0.0 0.0 0.0 0.0 77.95
BOX do4 -52.93 92.42 -38.97 -2.98 2.98 0.0 -39.88 -39.88 0.0 0.0 0.0 77.95
BOX do5 -102.77 27.92 -38.97 -4.21 0.0 0.0 0.0 -56.40 0.0 0.0 0.0 77.95
BOX do6 -92.42 -52.93 -38.97 -2.98 -2.98 0.0 39.88 -39.88 0.0 0.0 0.0 77.95
BOX do7 -27.92 -102.77 -38.97 0.00 -4.21 0.0 56.40 0.0 0.0 0.0 0.0 77.95
BOX do8 52.93 -92.42 -38.97 2.98 -2.98 0.00 39.88 39.88 0.0 0.0 0.0 77.95
* ==Door blocks
BOX door_1 106.44 -30.52 -43.29 6.60 0.0 0.0 0.0 64.68 0.0 0.0 0.0 86.58
BOX door_2 96.84 53.68 -43.29 4.67 4.67 0.0 -45.73 45.73 0.0 0.0 0.0 86.58
BOX door_3 30.52 106.44 -43.29 0.0 6.60 0.0 -64.68 0.0 0.0 0.0 0.0 86.58
```

```
BOX door_4 -53.68 96.84 -43.29 -4.67 4.67 0.0 -45.73 -45.73 0.0 0.0 0.0 86.58
BOX door_5 -106.44 30.52 -43.29 -6.60 0.0 0.0 0.0 -64.68 0.0 0.0 0.0 86.58
BOX door_6 -96.84 -53.68 -43.29 -4.67 -4.67 0.0 45.73 -45.73 0.0 0.0 0.0 86.58
BOX door_7 -30.52 -106.44 -43.29 0.0 -6.6 0.0 64.68 0.0 0.0 0.0 0.0 86.58
BOX door_8 53.68 -96.84 -43.29 4.67 -4.67 0.0 45.73 45.73 0.0 0.0 0.0 86.58
* ==Door viewports
RCC dv11_i      113.28 0.00 0.00 -7.10 0.00 0.00 17.78
RCC dv21_i      80.10 80.10 0.00 -5.02 -5.02 0.00 17.78
RCC dv31_i      0.00 113.28 0.00 0.00 -7.10 0.00 17.78
RCC dv41_i      -80.10 80.10 0.00 5.02 -5.02 0.00 17.78
RCC dv51_i      -113.28 0.00 0.00 7.10 0.00 0.00 17.78
RCC dv61_i      -80.10 -80.10 0.00 5.02 5.02 0.00 17.78
RCC dv71_i      0.00 -113.28 0.00 0.00 7.10 0.00 17.78
RCC dv81_i      80.10 -80.10 0.00 -5.02 5.02 0.00 17.78
RCC dv11_o      112.28 0.00 0.00 3.67 0.00 0.00 22.23
RCC dv21_o      81.99 81.99 0.00 -2.60 -2.60 0.00 22.23
RCC dv31_o      0.00 115.95 0.00 0.00 -3.67 0.00 22.23
RCC dv41_o      -81.99 81.99 0.00 2.60 -2.60 0.00 22.23
RCC dv51_o      -112.28 0.00 0.00 -3.67 0.00 0.00 22.23
RCC dv61_o      -81.99 -81.99 0.00 2.60 2.60 0.00 22.23
RCC dv71_o      0.00 -115.95 0.00 0.00 3.67 0.00 22.23
RCC dv81_o      81.99 -81.99 0.00 -2.60 2.60 0.00 22.23
RCC dv12_i      111.60 0.00 30.53 -15.00 0.00 -4.10 5.08
RCC dv22_i      78.91 78.91 30.53 -10.61 -10.61 -4.10 5.08
RCC dv32_i      0.00 111.60 30.53 0.00 -15.00 -4.10 5.08
RCC dv42_i      -78.91 78.91 30.53 10.61 -10.61 -4.10 5.08
RCC dv52_i      -111.60 0.00 30.53 15.00 0.00 -4.10 5.08
RCC dv62_i      -78.91 -78.91 30.53 10.61 10.61 -4.10 5.08
RCC dv72_i      0.00 -111.60 30.53 0.00 15.00 -4.10 5.08
RCC dv82_i      78.91 -78.91 30.53 -10.61 10.61 -4.10 5.08
*
RCC dv12_o      111.60 0.00 30.53 3.17 0.00 0.87 6.67
RCC dv22_o      78.91 78.91 30.53 2.24 2.24 0.87 6.67
RCC dv32_o      0.00 111.60 30.53 0.00 3.17 0.87 6.67
RCC dv42_o      -78.91 78.91 30.53 -2.24 2.24 0.87 6.67
RCC dv52_o      -111.60 0.00 30.53 -3.17 0.00 0.87 6.67
RCC dv62_o      -78.91 -78.91 30.53 -2.24 -2.24 0.87 6.67
RCC dv72_o      0.00 -111.60 30.53 0.00 -3.17 0.87 6.67
RCC dv82_o      78.91 -78.91 30.53 2.24 -2.24 0.87 6.67
* ==Body viewports
RCC bv1_i       119.37 49.44 0.0 -31.18 -12.92 0.0 5.08
RCC bv1_o1      89.17 36.94 0.0 29.57 12.25 0.0 5.72
RCC bv1_o2      119.09 49.33 0.0 -1.176395 -0.4785336 0.0 8.26
RCC bv2_i       49.44 119.37 0.0 -12.92 -31.18 0.0 5.08
RCC bv2_o1      36.94 89.17 0.0 12.25 29.57 0.0 5.72
RCC bv2_o2      49.33 119.09 0.0 -0.47853362 -1.1763952 0.0 8.26
RCC bv3_i       -49.44 119.37 0.0 12.92 -31.18 0.0 5.08
RCC bv3_o1      -36.94 89.17 0.0 -12.25 29.57 0.0 5.72
RCC bv3_o2      -49.33 119.09 0.0 0.47853362 -1.1763952 0.0 8.26
RCC bv4_i       -119.37 49.44 0.0 31.18 -12.92 0.0 5.08
RCC bv4_o1      -89.17 36.94 0.0 -29.57 12.25 0.0 5.72
RCC bv4_o2      -119.09 49.33 0.0 1.1763952 -0.47853362 0.0 8.26
RCC bv5_i       -119.37 -49.44 0.0 31.18 12.92 0.0 5.08
RCC bv5_o1      -89.17 -36.94 0.0 -29.57 -12.25 0.0 5.72
RCC bv5_o2      -119.09 -49.33 0.0 1.176395 0.4785336 0.0 8.26
RCC bv6_i       -49.44 -119.37 0.0 12.92 31.18 0.0 5.08
RCC bv6_o1      -36.94 -89.17 0.0 -12.25 -29.57 0.0 5.72
RCC bv6_o2      -49.33 -119.09 0.0 0.47853362 1.1763952 0.0 8.26
RCC bv7_i       49.44 -119.37 0.0 -12.92 31.18 0.0 5.08
RCC bv7_o1      36.94 -89.17 0.0 12.25 -29.57 0.0 5.72
RCC bv7_o2      49.33 -119.09 0.0 -0.47853362 1.1763952 0.0 8.26
RCC bv8_i       119.37 -49.44 0.0 -31.18 12.92 0.0 5.08
RCC bv8_o1      89.17 -36.94 0.0 29.57 -12.25 0.0 5.72
RCC bv8_o2      119.09 -49.33 0.0 -1.1763952 0.47853362 0.0 8.26
* ==Top plate 2 inches
XYP top_z       51.26
RCC top_i       0.00 0.00 51.28 0.0 0.0 -5.15 102.1
RCC top_o       0.00 0.00 51.28 0.0 0.0 -5.14 118.1
```

```
* ==Lid sphere
SPH lid_i       0.0 0.0 -125.17 203.84
SPH lid_o       0.0 0.0 -125.17 205.75
* ==Top viewport
RCC tv_i        0.0 0.0 90.47 0.0 0.0 -16.85 15.24
RCC tv_o        0.0 0.0 90.42 0.0 0.0 -16.75 22.23
XYP glass_z     88.42
* ==Lid viewports
RCC lv1_i       86.40 0.00 80.47 -23.42 0.00 -21.81 9.53
RCC lv2_i       71.84 48.00 80.47 -19.47 -13.01 -21.81 9.53
RCC lv3_i       48.00 71.84 80.47 -13.01 -19.47 -21.81 9.53
RCC lv4_i       0.00 86.40 80.47 0.00 -23.42 -21.81 9.53
RCC lv5_i       -48.00 71.84 80.47 13.01 -19.47 -21.81 9.53
RCC lv6_i       -71.84 48.00 80.47 19.47 -13.01 -21.81 9.53
RCC lv7_i       -86.40 0.00 80.47 23.42 0.00 -21.81 9.53
RCC lv8_i       -71.84 -48.00 80.47 19.47 13.01 -21.81 9.53
RCC lv9_i       -48.00 -71.84 80.47 13.01 19.47 -21.81 9.53
RCC lv10_i      0.00 -86.40 80.47 0.00 23.42 -21.81 9.53
RCC lv11_i      48.00 -71.84 80.47 -13.01 19.47 -21.81 9.53
RCC lv12_i      71.84 -48.00 80.47 -19.47 13.01 -21.81 9.53
RCC lv1_o1      85.47 0.00 79.60 -21.64 0.00 -20.20 12.70
RCC lv2_o1      71.06 47.48 79.60 -18.00 -12.02 -20.20 12.70
RCC lv3_o1      47.48 71.06 79.60 -12.02 -18.00 -20.20 12.70
RCC lv4_o1      0.00 85.47 79.60 0.00 -21.64 -20.20 12.70
RCC lv5_o1      -47.48 71.06 79.60 12.02 -18.00 -20.20 12.70
RCC lv6_o1      -71.06 47.48 79.60 18.00 -12.02 -20.20 12.70
RCC lv7_o1      -85.47 0.00 79.60 21.64 0.00 -20.20 12.70
RCC lv8_o1      -71.06 -47.48 79.60 18.00 12.02 -20.20 12.70
RCC lv9_o1      -47.48 -71.06 79.60 12.02 18.00 -20.20 12.70
RCC lv10_o1     0.00 -85.47 79.60 0.00 21.64 -20.20 12.70
RCC lv11_o1     47.48 -71.06 79.60 -12.02 18.00 -20.20 12.70
RCC lv12_o1     71.06 -47.48 79.60 -18.00 12.02 -20.20 12.70
RCC lv1_o2      85.90 0.00 80.00 -0.92777 0.00 -0.86726 16.62
RCC lv2_o2      71.43 47.73 80.00 -0.778673 -0.519116 -0.858537 16.62
RCC lv3_o2      47.73 71.43 80.00 -0.519116 -0.778673 -0.858537 16.62
RCC lv4_o2      0.00 85.90 80.00 0.00 -0.92777 -0.86726 16.62
RCC lv5_o2      -47.73 71.43 80.00 0.519116 -0.778673 -0.858537 16.62
RCC lv6_o2      -71.43 47.73 80.00 0.778673 -0.519116 -0.858537 16.62
RCC lv7_o2      -85.90 0.00 80.00 0.92777 0.00 -0.86726 16.62
RCC lv8_o2      -71.43 -47.73 80.00 0.778673 0.519116 -0.858537 16.62
RCC lv9_o2      -47.73 -71.43 80.00 0.519116 0.778673 -0.858537 16.62
RCC lv10_o2     0.00 -85.90 80.00 0.00 0.92777 -0.86726 16.62
RCC lv11_o2     47.73 -71.43 80.00 -0.519116 0.778673 -0.858537 16.62
RCC lv12_o2     71.43 -47.73 80.00 -0.778673 0.519116 -0.858537 16.62
RPP magnet      -24.0 0.0 1.6 16.1 -4.0 4.0
RCC det3        106.5 8.85 0.0 200.0 0.0 0.0 2.5
RCC det4        106.5 8.85 0.0 201.0 0.0 0.0 3.5
XCC hole2       13.0 0.0 0.635
RPP shield1a    90.65 95.65 -20.32 20.32 -20.32 20.32
RPP shield1b    95.651 100.731 -20.32 20.32 -20.32 20.32
RPP shield2a    28.166 33.166 -53.34 -6.4 -5.0 5.0
RPP shield2b    33.167 43.327 -53.34 -6.4 -5.0 5.0
RCC shield3a    18.5 0.0 0.0 5.0 0.0 0.0 5.715
RCC shield3b    23.66 0.0 0.0 8.5852 0.0 0.0 5.08
XCC hole3       0.0 0.0 0.47625
RPP hole1a      20.0 120.0 -1.9 1.9 -0.95 0.95
RPP hole1b      20.0 120.0 -1.9 1.9 -0.95 0.95
* ==Target foil
RPP target      0.0 0.01 -2.0 2.0 -2.0 2.0
SPH source      0.0 0.0 0.0 0.05
RPP leadw1      305.0 315.0 -10.0 10.0 -10.0 10.0
* ==Water beam monitor
RPP water       500.0 507.0 -45.593 45.593 -33.909 33.909
RPP case        499.6825 507.3175 -45.9105 45.9105 -34.2265 34.2265
* ==diamond window during Aug-2014 run
RCC diamd1      0.0 -120.0 0.0 0.0 7.1 0.0 1.0
XZP diamd2      -115.94
* ==Hutch 6
```

```
RPP h6in       -849. 533. -480. 594. -106. 351.
RPP h6out      -950.0 800.0 -481.0 700.0 -110.0 600.0
YZP h6xpl1     -848.91
YZP h6xpl2     -660.
YZP h6xpl3     -355.
YZP h6xpl4     -354.
YZP h6xpl5     -353.92
YZP h6xpl6     532.92
XZP h6ypl1     -479.92
XZP h6ypl2     296.8789
XZP h6ypl3     297.
XZP h6ypl4     593.92
* ==4 inches concrete
XYP h6zpl1     340.84
* ==6 inches concrete under control room
XYP h6zpl2     366.34
RPP conc1      -849.0 533.0 -510.1 -480.1 -106.0 351.0
RPP conc2      -849.0 533.0 -480.0 594.0 -136.1 -106.1
RPP ctrlrm     -225. 515. 20. 442. 351.1 595.1
RPP conc6in    -225. 515. 20. 442. 325.59 340.83
* ==air detectors outside target chamber
SPH det0       120.0 0.0 0.0 0.62035
SPH det45      84.8528 84.8528 0.0 0.62035
SPH det90      0.0 120.0 0.0 0.62035
SPH det135     -84.8528 84.8528 0.0 0.62035
SPH det180     -120.0 0.0 0.0 0.62035
SPH detcr      0.0 0.0 120.0 0.62035
$end_transform
END
*
* --+----1----+----2----+----3----+----4----+----5----+----6----+----7----+----8
BLKHOLE     10 +blkhole -h6out
MEC1        10 |+hall  -bp_t  +top_z  -top_o
|+hall  -top_z -lid_o  -tv_o
-lv1_o1  -lv2_o1  -lv3_o1  -lv4_o1
-lv5_o1  -lv6_o1  -lv7_o1  -lv8_o1
-lv9_o1  -lv10_o1 -lv11_o1 -lv12_o1
-lv1_o2  -lv2_o2  -lv3_o2  -lv4_o2
-lv5_o2  -lv6_o2  -lv7_o2  -lv8_o2
-lv9_o2  -lv10_o2 -lv11_o2 -lv12_o2
-detcr
MEC2        10 +hall  +bp_t  -bp_b
-(+bp_o1  +bp_o2  +bp_o3  +bp_o4
+bp_o5  +bp_o6  +bp_o7  +bp_o8)
-bv1_o1  -bv1_o2  -bv2_o1  -bv2_o2
-bv3_o1  -bv3_o2  -bv4_o1  -bv4_o2
-bv5_o1  -bv5_o2  -bv6_o1  -bv6_o2
-bv7_o1  -bv7_o2  -bv8_o1  -bv8_o2
-door_1  -door_2  -door_3  -door_4
-door_5  -door_6  -door_7  -door_8
-dv11_o  -dv12_o
-dv31_o  -dv32_o
-dv51_o  -dv52_o
-dv71_o  -dv72_o
-det0 -det45 -det90 -det135 -det180 -detcr
MEC3        10 +hall  +bp_b  -bottom
* ==Air detectors outside target chamber
DET0        10 +det0
DET45       10 +det45
DET90       10 +det90
DET135      10 +det135
DET180      10 +det180
DETCR       10 +detcr
* ==Target chamber bottom
*
CHMB_BT     10 +bottom  +bp_b
TARGET      10 +target
```

```
#if 0
SOURCE      10 +source
#endif
CHMB_IN     10 +bp_t  -bp_b
+bp_i1  +bp_i2  +bp_i3  +bp_i4
+bp_i5  +bp_i6  +bp_i7  +bp_i8
-target
CHMB_BD     10 +bp_t  -bp_b
+bp_o1  +bp_o2  +bp_o3  +bp_o4
+bp_o5  +bp_o6  +bp_o7  +bp_o8
-(+bp_i1  +bp_i2  +bp_i3  +bp_i4
+bp_i5  +bp_i6  +bp_i7  +bp_i8)
-bv1_o1 -bv2_o1 -bv3_o1 -bv4_o1
-bv5_o1 -bv6_o1 -bv7_o1 -bv8_o1
-do1    -do2    -do3    -do4
-do5    -do6    -do7    -do8
* ==Target chamber doors
DOPEN1      10 +do1 -bp_i1 +bp_o1
DOPEN2      10 +do2  -bp_i2  +bp_o2
DOPEN3      10 +do3  -bp_i3  +bp_o3
DOPEN4      10 +do4  -bp_i4  +bp_o4
DOPEN5      10 +do5  -bp_i5  +bp_o5
DOPEN6      10 +do6  -bp_i6  +bp_o6
DOPEN7      10 +do7  -bp_i7  +bp_o7
DOPEN8      10 +do8  -bp_i8  +bp_o8
DOOR1       10 +door_1 -bp_o1 -dv11_i -dv12_i -dv12_o
DVIEW11I    10 +door_1 -bp_o1 +dv11_i
DVIEW11O    10 +dv11_o -door_1
DVIEW12I    10 +door_1 -bp_o1 +dv12_i -dv12_o
DVIEW12O    10 +dv12_o
DOOR2       10 +door_2  -bp_o2
DOOR3       10 +door_3  -bp_o3  -dv31_i  -dv32_i  -dv32_o
DVIEW31I    10 +door_3  -bp_o3  +dv31_i
DVIEW31O    10 +dv31_o  -door_3
DVIEW32I    10 +door_3 -bp_o3 +dv32_i -dv32_o
DVIEW32O    10 +dv32_o
DOOR4       10 +door_4  -bp_o4
DOOR5       10 +door_5  -bp_o5  -dv51_i  -dv52_i  -dv52_o
DVIEW51I    10 +door_5  -bp_o5  +dv51_i
DVIEW51O    10 +dv51_o  -door_5
DVIEW52I    10 +door_5 -bp_o5 +dv52_i -dv52_o
DVIEW52O    10 +dv52_o
DOOR6       10 +door_6  -bp_o6
DOOR7       10 +door_7  -bp_o7  -dv71_i  -dv72_i  -dv72_o
DVIEW71I    10 +door_7 -bp_o7 +dv71_i -diamd1
DVIEW71O    10 +dv71_o -door_7 -diamd1
DVIEW72I    10 +door_7 -bp_o7 +dv72_i -dv72_o
DVIEW72O    10 +dv72_o
DOOR8       10 +door_8  -bp_o8
BVIEW1A     10 +bv1_i   +bv1_o1  -bv1_o2  -(+bp_i1 +bp_i2)
BVIEW1W     10 |+bv1_o1  -bv1_o2  -bv1_i   -(+bp_i1 +bp_i2)
|+bv1_o2  -bv1_i
BVIEW1G     10 +bv1_i   +bv1_o2
BVIEW2A     10 +bv2_i   +bv2_o1  -bv2_o2  -(+bp_i2 +bp_i3)
BVIEW2W     10 |+bv2_o1  -bv2_o2  -bv2_i   -(+bp_i2 +bp_i3)
|+bv2_o2  -bv2_i
BVIEW2G     10 +bv2_i   +bv2_o2
BVIEW3A     10 +bv3_i   +bv3_o1  -bv3_o2  -(+bp_i3 +bp_i4)
BVIEW3W     10 |+bv3_o1  -bv3_o2  -bv3_i   -(+bp_i3 +bp_i4)
|+bv3_o2  -bv3_i
BVIEW3G     10 +bv3_i   +bv3_o2
BVIEW4A     10 +bv4_i   +bv4_o1  -bv4_o2  -(+bp_i4 +bp_i5)
BVIEW4W     10 |+bv4_o1  -bv4_o2  -bv4_i   -(+bp_i4 +bp_i5)
|+bv4_o2  -bv4_i
BVIEW4G     10 +bv4_i   +bv4_o2
BVIEW5A     10 +bv5_i   +bv5_o1  -bv5_o2  -(+bp_i5 +bp_i6)
```

```
BVIEW5W     10 |+bv5_o1  -bv5_o2  -bv5_i   -(+bp_i5 +bp_i6)
|+bv5_o2  -bv5_i
BVIEW5G     10 +bv5_i   +bv5_o2
BVIEW6A     10 +bv6_i   +bv6_o1  -bv6_o2  -(+bp_i6 +bp_i7)
BVIEW6W     10 |+bv6_o1  -bv6_o2  -bv6_i   -(+bp_i6 +bp_i7)
|+bv6_o2  -bv6_i
BVIEW6G     10 +bv6_i   +bv6_o2
BVIEW7A     10 +bv7_i   +bv7_o1  -bv7_o2  -(+bp_i7 +bp_i8)
BVIEW7W     10 |+bv7_o1  -bv7_o2  -bv7_i   -(+bp_i7 +bp_i8)
|+bv7_o2  -bv7_i
BVIEW7G     10 +bv7_i   +bv7_o2
BVIEW8A     10 +bv8_i   +bv8_o1  -bv8_o2  -(+bp_i8 +bp_i1)
BVIEW8W     10 |+bv8_o1  -bv8_o2  -bv8_i   -(+bp_i8 +bp_i1)
|+bv8_o2  -bv8_i
BVIEW8G     10 +bv8_i   +bv8_o2
* ==Target chamber lid
TOPRO       10 +top_o  -top_i  -bp_t   +top_z
TOPRI       10 +top_o  +top_i  -bp_t   +top_z
LIDO        10 +lid_o  -lid_i  -top_z  -tv_o
-lv1_o1  -lv2_o1  -lv3_o1  -lv4_o1
-lv5_o1  -lv6_o1  -lv7_o1  -lv8_o1
-lv9_o1  -lv10_o1 -lv11_o1 -lv12_o1
LIDI        10 +lid_i  -top_z
TOPVO       10 +tv_o   -tv_i   -lid_i
TOPVI1      10 +tv_o   +tv_i           -glass_z
TOPVI2      10 +tv_o   +tv_i   -lid_i  +glass_z
* ==Target chamber lid viewports
LVIEW1A     10 +lv1_i  +lv1_o1 -lv1_o2  -lid_i
LVIEW1W     10 |-lv1_i  +lv1_o1 -lv1_o2  -lid_i
|-lv1_i  +lv1_o2
LVIEW1G     10 +lv1_i  +lv1_o2
LVIEW2A     10 +lv2_i  +lv2_o1 -lv2_o2  -lid_i
LVIEW2W     10 |-lv2_i  +lv2_o1 -lv2_o2  -lid_i
|-lv2_i  +lv2_o2
LVIEW2G     10 +lv2_i  +lv2_o2
LVIEW3A     10 +lv3_i  +lv3_o1 -lv3_o2  -lid_i
LVIEW3W     10 |-lv3_i  +lv3_o1 -lv3_o2  -lid_i
|-lv3_i  +lv3_o2
LVIEW3G     10 +lv3_i  +lv3_o2
LVIEW4A     10 +lv4_i  +lv4_o1 -lv4_o2  -lid_i
LVIEW4W     10 |-lv4_i  +lv4_o1 -lv4_o2  -lid_i
|-lv4_i  +lv4_o2
LVIEW4G     10 +lv4_i  +lv4_o2
LVIEW5A     10 +lv5_i  +lv5_o1 -lv5_o2  -lid_i
LVIEW5W     10 |-lv5_i  +lv5_o1 -lv5_o2  -lid_i
|-lv5_i  +lv5_o2
LVIEW5G     10 +lv5_i  +lv5_o2
LVIEW6A     10 +lv6_i  +lv6_o1 -lv6_o2  -lid_i
LVIEW6W     10 |-lv6_i  +lv6_o1 -lv6_o2  -lid_i
|-lv6_i  +lv6_o2
LVIEW6G     10 +lv6_i  +lv6_o2
LVIEW7A     10 +lv7_i  +lv7_o1 -lv7_o2  -lid_i
LVIEW7W     10 |-lv7_i  +lv7_o1 -lv7_o2  -lid_i
|-lv7_i  +lv7_o2
LVIEW7G     10 +lv7_i  +lv7_o2
LVIEW8A     10 +lv8_i  +lv8_o1 -lv8_o2  -lid_i
LVIEW8W     10 |-lv8_i  +lv8_o1 -lv8_o2  -lid_i
|-lv8_i  +lv8_o2
LVIEW8G     10 +lv8_i  +lv8_o2
LVIEW9A     10 +lv9_i  +lv9_o1 -lv9_o2  -lid_i
LVIEW9W     10 |-lv9_i  +lv9_o1 -lv9_o2  -lid_i
|-lv9_i  +lv9_o2
LVIEW9G     10 +lv9_i  +lv9_o2
LVIEW10A    10 +lv10_i  +lv10_o1 -lv10_o2  -lid_i
LVIEW10W    10 |-lv10_i  +lv10_o1 -lv10_o2  -lid_i
|-lv10_i  +lv10_o2
```

```
LVIEW10G    10 +lv10_i  +lv10_o2
LVIEW11A    10 +lv11_i  +lv11_o1 -lv11_o2  -lid_i
LVIEW11W    10 |-lv11_i  +lv11_o1 -lv11_o2  -lid_i
|-lv11_i  +lv11_o2
LVIEW11G    10 +lv11_i  +lv11_o2
LVIEW12A    10 +lv12_i  +lv12_o1 -lv12_o2  -lid_i
LVIEW12W    10 |-lv12_i  +lv12_o1 -lv12_o2  -lid_i
|-lv12_i  +lv12_o2
LVIEW12G    10 +lv12_i  +lv12_o2
* ==Hutch 6 room
H6IN        10 | +h6in -h6ypl2 +h6ypl4 -h6xpl5 +h6xpl6 +h6zpl1
| (+h6in  -h6ypl1 +h6ypl2 -h6xpl1 +h6xpl6 -hall
+h6zpl1 )
H6OUT       10 | +h6out -h6in -ctrlrm
| +h6in -h6ypl3 +h6xpl4
H6WALL      10 | +h6in -h6xpl6
| +h6in -h6ypl4 +h6xpl6 -h6xpl5
| +h6in +h6xpl5 -h6ypl3 -h6xpl4
| +h6in +h6ypl1 +h6xpl6 -h6xpl1
| +h6in +h6xpl1 +h6ypl3
| +h6in +h6ypl3 -h6ypl2 -h6xpl1 +h6xpl2
| +h6in +h6ypl3 -h6ypl2 -h6xpl3 +h6xpl5
H6ROOF      10 | +h6in -h6zpl1 +h6ypl2 -h6xpl1 +h6xpl6 -h6ypl1
| +h6in -h6zpl1 -h6ypl2 -h6xpl5 +h6xpl6 +h6ypl4
H6ROLLUP    10 +h6in -h6ypl2 +h6ypl3 -h6xpl2 +h6xpl3
H6CTRLRM    10 +ctrlrm -h6zpl2
CONCROOF    10 +ctrlrm +h6zpl2
DIAMDWIN    10 +diamd1 +diamd2 +dv71_o
DIAMDGAP    10 +diamd1 -diamd2 +dv71_o
END
*
GEOEND
*
* --+----1----+----2----+----3----+----4----+----5----+----6----+----7----+----8
*
MATERIAL         24.   51.9961      7.18                              CHROMIUM
MATERIAL         19.   39.0983     0.862                              POTASSIU
MATERIAL         15. 30.973761       2.2                              PHOSPHO
MATERIAL         25. 54.938049      7.44                              MANGANES
* ==Air
MATERIAL                       0.0012048                              AIR
COMPOUND    -1.24E-4    CARBON -0.755267  NITROGEN -0.231781    OXYGENAIR
COMPOUND   -0.012827     ARGON                                       AIR
* ==Air2 (identical to Air)
MATERIAL                       0.0012048                              AIR2
COMPOUND    -1.24E-4    CARBON -0.755267  NITROGEN -0.231781    OXYGENAIR2
COMPOUND   -0.012827     ARGON                                       AIR2
* ==Pyrex Glass
MATERIAL                           2.23                              PYRXGLAS
COMPOUND     -4.0064  BERYLLIU  -53.9561    OXYGEN   -2.8191    SODIUMPYRXGLAS
COMPOUND     -1.1644  ALUMINUM  -37.7219   SILICON   -0.3321  POTASSIUPYRXGLAS
* ==Typical Stainless Steel from FLUKA
MATERIAL                           8.0                               Stainles
COMPOUND        18.0  CHROMIUM      74.0      IRON       8.0    NICKELStainles
* ==Portland Concrete from FLUKA
MATERIAL                           2.3                               PORTLAND
COMPOUND       -0.01  HYDROGEN    -0.001    CARBON -0.529107    OXYGENPORTLAND
COMPOUND      -0.016    SODIUM    -0.002  MAGNESIU -0.033872  ALUMINUMPORTLAND
COMPOUND   -0.337021   SILICON    -0.013  POTASSIU    -0.044   CALCIUMPORTLAND
COMPOUND      -0.014      IRON                                       PORTLAND
* ==Liquid H2 jet for Glenzer experiment
MATERIAL                          0.07                               LH2
COMPOUND        -1.0  HYDROGEN                                       LH2
MATERIAL         33.                5.73                              ARSENIC
* ==Lead Glass from FLUKA
*
```

```
MATERIAL                              6.22                                LEAD-GLA
COMPOUND   -0.156453    OXYGEN -0.080866   SILICON -0.008092  TITANIUMLEAD-GLA
COMPOUND   -0.002651   ARSENIC -0.751938      LEAD                     LEAD-GLA
* ==Polyethylene Marlex
* Density variation of polyethylene is 0.91 - 1.05 g/cm3. "Low" density is
*  0.920, "medium" is .93, and "high" is .95. Special polyethelene is made
* for nuclear shielding, and this has loaded densities up to 1.08 g/cm3
MATERIAL                              0.95                                Polyethy
COMPOUND         4.0  HYDROGEN       2.0    CARBON                       Polyethy
* ==90% Tungsten alloy (0.614 lbs/in3)
MATERIAL                              17.0                                W90
COMPOUND        -0.9  TUNGSTEN     -0.06    NICKEL     -0.04    COPPERW90
MATERIAL                              3.52                                DIAMD
COMPOUND        -1.0    CARBON                                            DIAMD
*
* --+----1----+----2----+----3----+----4----+----5----+----6----+----7----+----8
ASSIGNMA    BLCKHOLE   BLKHOLE
ASSIGNMA         AIR      MEC1
ASSIGNMA         AIR      MEC2
ASSIGNMA         AIR      MEC3
ASSIGNMA      VACUUM   CHMB_IN
ASSIGNMA    ALUMINUM   CHMB_BD
ASSIGNMA    ALUMINUM   CHMB_BT
ASSIGNMA      VACUUM    DOPEN1
ASSIGNMA      VACUUM    DOPEN2
ASSIGNMA      VACUUM    DOPEN3
ASSIGNMA      VACUUM    DOPEN4
ASSIGNMA      VACUUM    DOPEN5
ASSIGNMA      VACUUM    DOPEN6
ASSIGNMA      VACUUM    DOPEN7
ASSIGNMA      VACUUM    DOPEN8
ASSIGNMA    ALUMINUM     DOOR1
ASSIGNMA    ALUMINUM     DOOR2
ASSIGNMA    ALUMINUM     DOOR3
ASSIGNMA    ALUMINUM     DOOR4
ASSIGNMA    ALUMINUM     DOOR5
ASSIGNMA    ALUMINUM     DOOR6
ASSIGNMA    ALUMINUM     DOOR7
ASSIGNMA    ALUMINUM     DOOR8
ASSIGNMA    ALUMINUM  DVIEW11I
ASSIGNMA         AIR  DVIEW11O
ASSIGNMA      VACUUM  DVIEW12I
ASSIGNMA    ALUMINUM  DVIEW12O
ASSIGNMA    ALUMINUM  DVIEW31I
ASSIGNMA         AIR  DVIEW31O
ASSIGNMA      VACUUM  DVIEW32I
ASSIGNMA    ALUMINUM  DVIEW32O
ASSIGNMA    ALUMINUM  DVIEW51I
ASSIGNMA         AIR  DVIEW51O
ASSIGNMA      VACUUM  DVIEW52I
ASSIGNMA    ALUMINUM  DVIEW52O
ASSIGNMA    ALUMINUM  DVIEW71I
ASSIGNMA         AIR  DVIEW71O
ASSIGNMA      VACUUM  DVIEW72I
ASSIGNMA    ALUMINUM  DVIEW72O
ASSIGNMA      VACUUM   BVIEW1A
ASSIGNMA    ALUMINUM   BVIEW1W
ASSIGNMA    PYRXGLAS   BVIEW1G
ASSIGNMA      VACUUM   BVIEW2A
ASSIGNMA    ALUMINUM   BVIEW2W
ASSIGNMA    PYRXGLAS   BVIEW2G
ASSIGNMA      VACUUM   BVIEW3A
ASSIGNMA    ALUMINUM   BVIEW3W
ASSIGNMA    PYRXGLAS   BVIEW3G
ASSIGNMA      VACUUM   BVIEW4A
ASSIGNMA    ALUMINUM   BVIEW4W
ASSIGNMA    PYRXGLAS   BVIEW4G
```

```
ASSIGNMA      VACUUM   BVIEW5A
ASSIGNMA    ALUMINUM   BVIEW5W
ASSIGNMA    PYRXGLAS   BVIEW5G
ASSIGNMA      VACUUM   BVIEW6A
ASSIGNMA    ALUMINUM   BVIEW6W
ASSIGNMA    PYRXGLAS   BVIEW6G
ASSIGNMA      VACUUM   BVIEW7A
ASSIGNMA    ALUMINUM   BVIEW7W
ASSIGNMA    PYRXGLAS   BVIEW7G
ASSIGNMA      VACUUM   BVIEW8A
ASSIGNMA    ALUMINUM   BVIEW8W
ASSIGNMA    PYRXGLAS   BVIEW8G
ASSIGNMA    ALUMINUM     TOPRO
ASSIGNMA      VACUUM     TOPRI
ASSIGNMA    ALUMINUM      LIDO
ASSIGNMA      VACUUM      LIDI
ASSIGNMA    ALUMINUM     TOPVO
ASSIGNMA    ALUMINUM    TOPVI1
ASSIGNMA      VACUUM    TOPVI2
ASSIGNMA      VACUUM   LVIEW1A
ASSIGNMA    ALUMINUM   LVIEW1W
ASSIGNMA    ALUMINUM   LVIEW1G
ASSIGNMA      VACUUM   LVIEW2A
ASSIGNMA    ALUMINUM   LVIEW2W
ASSIGNMA    ALUMINUM   LVIEW2G
ASSIGNMA      VACUUM   LVIEW3A
ASSIGNMA    ALUMINUM   LVIEW3W
ASSIGNMA    ALUMINUM   LVIEW3G
ASSIGNMA      VACUUM   LVIEW4A
ASSIGNMA    ALUMINUM   LVIEW4W
ASSIGNMA    ALUMINUM   LVIEW4G
ASSIGNMA      VACUUM   LVIEW5A
ASSIGNMA    ALUMINUM   LVIEW5W
ASSIGNMA    ALUMINUM   LVIEW5G
ASSIGNMA      VACUUM   LVIEW6A
ASSIGNMA    ALUMINUM   LVIEW6W
ASSIGNMA    ALUMINUM   LVIEW6G
ASSIGNMA      VACUUM   LVIEW7A
ASSIGNMA    ALUMINUM   LVIEW7W
ASSIGNMA    ALUMINUM   LVIEW7G
ASSIGNMA      VACUUM   LVIEW8A
ASSIGNMA    ALUMINUM   LVIEW8W
ASSIGNMA    ALUMINUM   LVIEW8G
ASSIGNMA      VACUUM   LVIEW9A
ASSIGNMA    ALUMINUM   LVIEW9W
ASSIGNMA    PYRXGLAS   LVIEW9G
ASSIGNMA      VACUUM  LVIEW10A
ASSIGNMA    ALUMINUM  LVIEW10W
ASSIGNMA    ALUMINUM  LVIEW10G
ASSIGNMA      VACUUM  LVIEW11A
ASSIGNMA    ALUMINUM  LVIEW11W
ASSIGNMA    ALUMINUM  LVIEW11G
ASSIGNMA      VACUUM  LVIEW12A
ASSIGNMA    ALUMINUM  LVIEW12W
ASSIGNMA    ALUMINUM  LVIEW12G
ASSIGNMA    BLCKHOLE      H6IN
ASSIGNMA         AIR     H6OUT
ASSIGNMA        LEAD    H6WALL
ASSIGNMA    PORTLAND    H6ROOF
ASSIGNMA    Stainles  H6ROLLUP
ASSIGNMA        AIR2  H6CTRLRM
ASSIGNMA    PORTLAND  CONCROOF
ASSIGNMA         AIR      DET0
ASSIGNMA         AIR     DET45
ASSIGNMA         AIR     DET90
ASSIGNMA         AIR    DET135
ASSIGNMA         AIR    DET180
ASSIGNMA         AIR     DETCR
```

```
ASSIGNMA      COPPER    TARGET
ASSIGNMA       DIAMD  DIAMDWIN
ASSIGNMA         AIR  DIAMDGAP
*ASSIGNMA     VACUUM    SOURCE
* --+----1----+----2----+----3----+----4----+----5----+----6----+----7----+----8
* ==transport (by region): 100 keV e-  100 keV gamma
EMFCUT       -0.0001      1E-4       0.0      MEC1  @LASTREG
EMFCUT       -0.0001      1E-4       0.0  HYDROGEN  @LASTMAT          PROD-CUT
* ==(NOT USED)set 1 GeV photon production cut for Al-walled MEC chamber
*EMFCUT       -1E-06       1.0       1.0  ALUMINUM                    PROD-CUT
* ==field strength of magnet
*MGNFIELD       30.0      0.05       0.1       0.0       0.0      -0.6
*EMF-BIAS      1022.       0.0       0.0      MEC1  @LASTREG
PHOTONUC        0.0                       HYDROGEN  @LASTMAT
*
*LAM-BIAS        0.0      0.02    COPPER    PHOTON
*PART-THR    -1.0E-6    PROTON
*
* --+----1----+----2----+----3----+----4----+----5----+----6----+----7----+----8
* ==score particle fluence
USRBIN           10.  BEAMPART      -30.     150.0      15.0     150.0beampart
USRBIN        -150.0     -15.0    -150.0     300.0       1.0     300.0 &
* --+----1----+----2----+----3----+----4----+----5----+----6----+----7----+----8
* ==score dose equivalent
USRBIN           10.   DOSE-EQ      -31.     150.0      15.0     150.0deq.tot
USRBIN        -150.0     -15.0    -150.0     600.0       1.0     600.0 &
AUXSCORE      USRBIN  ALL-PART             deq.tot                    AMB74
USRBIN           10.   DOSE-EQ      -31.     150.0      15.0     150.0deq.e-
USRBIN        -150.0     -15.0    -150.0     600.0       1.0     600.0 &
AUXSCORE      USRBIN  ELECTRON             deq.e-                     AMB74
USRBIN           10.   DOSE-EQ      -31.     150.0      15.0     150.0deq.ph
USRBIN        -150.0     -15.0    -150.0     600.0       1.0     600.0 &
AUXSCORE      USRBIN    PHOTON             deq.ph                     AMB74
* --+----1----+----2----+----3----+----4----+----5----+----6----+----7----+----8
* ==score energy spectra
USRTRACK         -1.  BEAMPART      -29.    TARGET               200.0source
USRTRACK         0.2      1E-5                                        &
USRTRACK         -1.    PHOTON      -29.      MEC2               200.0h6.ph
USRTRACK         0.2      1E-5                                        &
USRTRACK         -1.  ELECTRON      -29.      MEC2     200.0     200.0h6.e-
USRTRACK         0.2      1E-5                                        &
*
* --+----1----+----2----+----3----+----4----+----5----+----6----+----7----+----8
RANDOMIZ         1.0        1.
START            1E7
*
STOP
```

Bibliography

[1] *NCRP Report No. 144: Radiation Protection for Particle Accelerator Facilities*. National Council on Radiation Protection and Measurements, 1 ed., Nov 2003.

[2] *Intense Laser Labs World Wide*. The International Committee on Ultra-High Intensity Lasers, 19 Feb 2017.

[3] Albert, F., Pollock, B. B., Shaw, J. L., Marsh, K. A., Ralph, J. E., Chen, Y.-H., Alessi, D., Pak, A., Clayton, C. E., Glenzer, S. H., and Joshi, C., "Angular Dependence of Betatron X-Ray Spectra from a Laser-Wakefield Accelerator," *Phys. Rev. Lett.*, vol. 111, p. 235004, Dec 2013.

[4] Andreev, A. A., Sonobe, R., Kawata, S., Miyazaki, S., Sakai, K., Miyauchi, K., Kikuchi, T., Platonov, K., and Nemoto, K., "Effect of a laser prepulse on fast ion generation in the interaction of ultra-short intense laser pulses with a limited-mass foil target," *Plasma Physics and Controlled Fusion*, vol. 48, no. 11, p. 1605, 2006.

[5] Arber, T. D., Bennett, K., Brady, C. S., Lawrence-Douglas, A., Ramsay, M. G., Sircombe, N. J., Gillies, P., Evans, R. G., Schmitz, H., Bell, A. R., and Ridgers, C. P., "Contemporary particle-in-cell approach to laser-plasma modelling," *Plasma Phys. Control. Fusion*, vol. 57, no. 11, p. 113001, 2015.

[6] Bauer, J., Liu, J. C., Prinz, A. A., Rokni, S. H., Tran, H., Woods, M., Xia, Z., Galtier, E., Lee, H. J., Milathianaki, D., and Nagler, B., "Measurements of Ionizing Radiation Doses Induced by High Irradiance Laser on Targets in LCLS MEC Instrument," *SLAC Publication*, no. SLAC-PUB-15889, 2013.

[7] Bauer, J., Liu, J. C., Prinz, A. A., Tran, H., and Xia, Z., "High Intensity Laser Induced Radiation Measurements at LLNL," *SLAC Radiation Physics Note*, no. RP–11–11, pp. 1–16, 2011.

[8] Bennett, K., "EPOCH is the Extendable PIC Open Collaboration project to develop a UK community advanced relativistic EM PIC code," https://cfsa-pmw.warwick.ac.uk/EPOCH/epoch.

[9] Berger, M., Coursey, J., Zucker, M., , and Chang, J., "ESTAR, PSTAR, and ASTAR: Computer Programs for Calculating Stopping-Power and Range Tables for Electrons, Protons, and Helium Ions (version 1.2.3)," *National Institute of Standards and Technology*, February 2017.

[10] Böhlen, T. T., Cerutti, F., Chin, M. P. W., Fassò, A., Ferrari, A., Ortega, P. G., Mairani, A., Sala, P. R., Smirnov, G., and Vlachoudis,

V., "The FLUKA Code: Developments and Challenges for High Energy and Medical Applications," *Nuclear Data Sheets*, vol. 120, pp. 211 – 214, 2014.

[11] Borne, F., Delacroix, D., M. Gel, J., Mass, D., and Amiranoff, F., "Radiation Protection for an Ultra-high Intensity Laser," *Radiation Protection Dosimetry*, vol. 102, no. 1, pp. 61–70, 2002.

[12] Chen, H., McLean, H. S., Patel, P. K., and Wilks, S. C., "Hot Electron Measurement and Modeling for Short-Pulse Laser Plasma Interactions," *Lawrence Livermore National Laboratory*, no. UCRL-JC-155353, 2003.

[13] Chen, L. M., Forget, P., Fourmaux, S., Kieffer, J. C., Krol, A., Chamberlain, C. C., Hou, B. X., Nees, J., and Mourou, G., "Study of hard x-ray emission from intense femtosecond Ti:sapphire lasersolid target interactions," *Phys. Plasmas*, vol. 11, no. 9, 2004.

[14] Chen, L. M., Yan, W. C., Li, D. Z., Hu, Z. D., Zhang, L., Wang, W. M., Hafz, N., Mao, J. Y., Huang, K., Ma, Y., Zhao, J. R., Ma, J. L., Li, Y. T., Lu, X., Sheng, Z. M., Wei, Z. Y., Gao, J., and Zhang, J., "Bright betatron X-ray radiation from a laser-driven-clustering gas target," *Sci. Rep.*, vol. 3, pp. 520–525, May 2013.

[15] Dixon, W. R., "Energy and Angular Distributions of of Photoneutrons Produced by 70-MeV. X-rays," *Can. J. Phys.*, vol. 37, pp. 785–796, 1955.

[16] Faure, J., Rechatin, C., Norlin, A., Lifschitz, A., Glinec, Y., and Malka, V., "Controlled injection and acceleration of electrons in plasma wakefields by colliding laser pulses," *Nature*, vol. 444, pp. 737–739, Dec 2006.

[17] Ferrari, A., Sala, P. R., Fassò, A., and Ranft, J., "FLUKA: a multi-particle transport code," *CERN-2005-10*, 2005.

[18] Ferrari, A., Sala, P., Guaraldi, R., and Padoani, F., "An improved multiple scattering model for charged particle transport," *Nuclear Instruments and Methods in Physics Research Section B: Beam Interactions with Materials and Atoms*, vol. 71, no. 4, pp. 412 – 426, 1992.

[19] Fourmaux, S., Buffechoux, S., Albertazzi, B., Capelli, D., Lvy, A., Gnedyuk, S., Lecherbourg, L., Lassonde, P., Payeur, S., Antici, P., Ppin, H., Marjoribanks, R. S., Fuchs, J., and Kieffer, J. C., "Investigation of laser-driven proton acceleration using ultra-short, ultra-intense laser pulses," *Phys. Plasmas*, vol. 20, no. 1, p. 013110, 2013.

[20] Fritzler, S., Lefebvre, E., Malka, V., Burgy, F., Dangor, A. E., Krushelnick, K., Mangles, S. P. D., Najmudin, Z., Rousseau, J.-P., and Walton, B., "Emittance Measurements of a Laser-Wakefield-Accelerated Electron Beam," *Phys. Rev. Lett.*, vol. 92, p. 165006, Apr 2004.

[21] Fuchs, J., Antici, P., d'Humières, E., Lefebvre, E., Borghesi, M., Brambrink, E., Cecchetti, C. A., Kaluza, M., Malka, V., Manclossi, M., Meyroneinc, S., Mora, P., Schreiber, J., Toncian, T., Pepin, H., and Audebert, P., "Laser-driven proton scaling laws and new paths towards energy increase," *Nat. Phys.*, vol. 2, pp. 48–54, 2006.

[22] Fuchs, T., *Laser-accelerated particles: Investigations towards applications in radiotherapy*. PhD thesis, Presented to Combined Faculties for the Natural Science and for Mathematics of the Ruperto-Carola University of Heidelberg, Germany, 2007.

[23] Gahn, C., Tsakiris, G. D., Pukhov, A., Meyer-ter Vehn, J., Pretzler, G., Thirolf, P., Habs, D., and Witte, K. J., "Multi-MeV Electron Beam Generation by Direct Laser Acceleration in High-Density Plasma Channels," *Phys. Rev. Lett.*, vol. 83, pp. 4772–4775, Dec 1999.

[24] Gibbon, P., *Short Pulse Laser Interactions with Matter: An Introduction*. World Scientific Publishing Company, 1 ed., Sep 2005.

[25] Glenzer, S. H., Fletcher, L. B., Galtier, E., Nagler, B., Alonso-Mori, R., Barbrel, B., Brown, S. B., Chapman, D. A., Chen, Z., Curry, C. B., Fiuza, F., Gamboa, E., Gauthier, M., Gericke, D. O., Gleason, A., Goede, S., Granados, E., Heimann, P., Kim, J., Kraus, D., MacDonald, M. J., Mackinnon, A. J., Mishra, R., Ravasio, A., Roedel, C., Sperling, P., Schumaker, W., Tsui, Y. Y., Vorberger, J., Zastrau, U., Fry, A., White, W. E., Hasting, J. B., and Lee, H. J., "Matter under extreme conditions experiments at the Linac Coherent Light Source," *Journal of Physics B: Atomic, Molecular and Optical Physics*, vol. 49, p. 092001, Apr 2016.

[26] Guillot, T., "Interiors of Giant Planets Inside and Outside the Solar System," *Science*, vol. 286, pp. 72–77, Oct 1999.

[27] Guo, T., Spielmann, C., Walker, B. C., and Barty, C. P. J., "Generation of hard x rays by ultrafast terawatt lasers," *Rev. Sci. Instr.*, vol. 72, no. 1, 2001.

[28] Haberberger, D., Tochitsky, S., Fiuza, F., Gong, C., Fonseca, R. A., Silva, L. O., Mori, W. B., and Joshi, C., "Collisionless shocks in laser-produced plasma generate monoenergetic high-energy proton beams," *Nat Phys*, vol. 8, pp. 95–99, Nov 2012.

[29] Hatchett, S. P., Brown, C. G., Cowan, T. E., Henry, E. A., Johnson, J. S., Key, M. H., Koch, J. A., Langdon, A. B., Lasinski, B. F., Lee, R. W., Mackinnon, A. J., Pennington, D. M., Perry, M. D., Phillips, T. W., Roth, M., Sangster, T. C., Singh, M. S., Snavely, R. A., Stoyer, M. A., Wilks, S. C., and Yasuike, K., "Electron, photon, and ion beams from the relativistic interaction of Petawatt laser pulses with solid targets," *Physics of Plasmas*, vol. 7, no. 5, pp. 2076–2082, 2000.

[30] Hayashi, Y., Fukumi, A., Matsukado, K., Mori, M., Kotaki, H., Kando, M., Chen, L. M., Daito, I., Kondo, S., Kanazawa, S., Yamazaki, A., Ogura, K., Nishiuchi, M., Kado, M., Sagisaka, A., Nakamura, S., Li, Z., Orimo, S., Homma, T., and Daido, H., "Estimation of photon dose generated by a short pulse high power laser," *Radiation Protection Dosimetry*, vol. 121, no. 2, pp. 99–107, 2006.

[31] Hu, S. X., Michel, D. T., Edgell, D. H., Froula, D. H., Follett, R. K., Goncharov, V. N., Myatt, J. F., Skupsky, S., and Yaakobi, B., "Hydrodynamic simulations of long-scale-length two-plasmondecay experiments at the Omega Laser Facility," *Physics of Plasmas*, vol. 20, no. 3, 2013.

[32] Kaluza, M., Schreiber, J., Santala, M. I. K., Tsakiris, G. D., Eidmann, K., Meyer-ter Vehn, J., and Witte, K. J., "Influence of the Laser Prepulse on Proton Acceleration in Thin-Foil Experiments," *Phys. Rev. Lett.*, vol. 93, p. 045003, Jul 2004.

[33] Key, M. H., Cable, M. D., Cowan, T. E., Estabrook, K. G., Hammel, B. A., Hatchett, S. P., Henry, E. A., Hinkel, D. E., Kilkenny, J. D., Koch, J. A., Kruer, W. L., Langdon, A. B., Lasinski, B. F., Lee, R. W., MacGowan, B. J., MacKinnon, A., Moody, J. D., Moran, M. J., Offenberger, A. A., Pennington, D. M., Perry, M. D., Phillips, T. J., Sangster, T. C., Singh, M. S., Stoyer, M. A., Tabak, M., Tietbohl, G. L., Tsukamoto, M., Wharton, K., and Wilks, S. C., "Hot electron production and heating by hot electrons in fast ignitor research," *Physics of Plasmas*, vol. 5, no. 5, 1998.

[34] Kim, L., Pratt, R. H., Seltzer, S. M., and Berger, M. J., "Ratio of positron to electron bremsstrahlung energy loss: An approximate scaling law," *Phys. Rev. A*, vol. 33, pp. 3002–3009, May 1986.

[35] Kluge, T., Cowan, T., Debus, A., Schramm, U., Zeil, K., and Bussmann, M., "Electron Temperature Scaling in Laser Interaction with Solids," *Phys. Rev. Lett.*, vol. 107, p. 205003, Nov 2011.

[36] Kulcsár, G., AlMawlawi, D., Budnik, F. W., Herman, P. R., Moskovits, M., Zhao, L., and Marjoribanks, R. S., "Intense Picosecond X-Ray Pulses from Laser Plasmas by Use of Nanostructured "Velvet" Targets," *Phys. Rev. Lett.*, vol. 84, pp. 5149–5152, May 2000.

[37] Ledingham, K. W. D., Spencer, I., McCanny, T., Singhal, R. P., Santala, M. I. K., Clark, E., Watts, I., Beg, F. N., Zepf, M., Krushelnick, K., Tatarakis, M., Dangor, A. E., Norreys, P. A., Allott, R., Neely, D., Clark, R. J., Machacek, A. C., Wark, J. S., Cresswell, A. J., Sanderson, D. C. W., and Magill, J., "Photonuclear Physics when a Multiterawatt Laser Pulse Interacts with Solid Targets," *Phys. Rev. Lett.*, vol. 84, pp. 899–902, Jan 2000.

[38] Leemans, W. P., Nagler, B., Gonsalves, A. J., Toth, C., Nakamura, K., Geddes, C. G. R., Esarey, E., Schroeder, C. B., and Hooker, S. M., "GeV electron beams from a centimetre-scale accelerator," *Nat. Phys.*, vol. 2, pp. 696–699, Sep 2006.

[39] Liang, T., Bauer, J., Blaha, J., Cimeno, M., Ferrari, A., Liu, J., Rokni, S., and Woods, M., "Ionizing Radiation Measurements from Interaction of MEC Laser (0.7 J, 10^{19} W/cm^2) with Cu and Ni Targets," *SLAC Radiation Physics Note*, no. RP–14–23, pp. 1–22, 2014.

[40] Liang, T., Bauer, J., Cimeno, M., Ferrari, A., Galtier, E., Granados, E., Lee, H. J., Liu, J., Nagler, B., Prinz, A., Rokni, S., Tran, H., and Woods, M., "Radiation Dose Measurements for High-Intensity Laser Interactions with Solid Targets at SLAC," *Radiation Protection Dosimetry*, vol. 172, no. 4, pp. 346–355, 2016.

[41] Liang, T., Bauer, J., Cimeno, M., Ferrari, A., Galtier, E., Granados, E., Liu, J., Nagler, B., Prinz, A., Rokni, S., Tran, H., and Woods, M., "Measurements of High-Intensity Laser Induced Ionizing Radiation at SLAC," *SLAC Publication*, no. SLAC-PUB-15973, pp. 1–18, 2014.

[42] Liang, T., Bauer, J., Liu, J., and Rokni, S., "Bremsstrahlung Dose Yield for High-Intensity Short-Pulse Laser-Solid Experiments," *Radiation Protection Dosimetry*, 2016.

[43] Liang, T., Bauer, J., Liu, J., and Rokni, S., "Development of a Photon Dose Yield Model for Laser-Solid Interaction by Coupling EPOCH and FLUKA," *SLAC Radiation Physics Note*, no. RP–16–14, pp. 1–28, 2016.

[44] Mckenna, P., Neely, D., Bingham, R., and Jaroszynski, D. A., *Laser-Plasma Interactions and Applications*. Springer International Publishing Switzerland, 2013.

[45] Meyerhofer, D. D., Chen, H., Delettrez, J. A., Soom, B., Uchida, S., and Yaakobi, B., "Resonance absorption in high-intensity contrast, picosecond laserplasma interactions," *Physics of Fluids B*, vol. 5, no. 7, 1993.

[46] Myatt, J., Theobald, W., Delettrez, J. A., Stoeckl, C., Storm, M., Sangster, T. C., Maximov, A. V., and Short, R. W., "High-intensity laser interactions with mass-limited solid targets and implications for fast-ignition experiments on OMEGA EPa)," *Physics of Plasmas*, vol. 14, no. 5, 2007.

[47] Nagler, B., Arnold, B., Bouchard, G., Boyce, R. F., Boyce, R. M., Callen, A., Campell, M., Curiel, R., Galtier, E., Garofoli, J., Granados, E., Hastings, J., Hays, G., Heimann, P., Lee, R. W., Milathianaki, D., Plummer, L., Schropp, A., Wallace, A., Welch, M., White, W., Xing, Z., Yin, J., Young, J., Zastrau, U., and Lee, H. J.,

"The Matter in Extreme Conditions instrument at the Linac Coherent Light Source," *J. of Synchrotron Radiat.*, vol. 22, pp. 520–525, May 2015.

[48] Norreys, P. A., Santala, M., Clark, E., Zepf, M., Watts, I., Beg, F. N., Krushelnick, K., Tatarakis, M., Dangor, A. E., Fang, X., Graham, P., McCanny, T., Singhal, R. P., Ledingham, K. W. D., Creswell, A., Sanderson, D. C. W., Magill, J., Machacek, A., Wark, J. S., Allott, R., Kennedy, B., and Neely, D., "Observation of a highly directional -ray beam from ultrashort, ultraintense laser pulse interactions with solids," *Physics of Plasmas*, vol. 6, no. 5, pp. 2150–2156, 1999.

[49] Ping, Y., Shepherd, R., Lasinski, B. F., Tabak, M., Chen, H., Chung, H. K., Fournier, K. B., Hansen, S. B., Kemp, A., Liedahl, D. A., Widmann, K., Wilks, S. C., Rozmus, W., and Sherlock, M., "Absorption of Short Laser Pulses on Solid Targets in the Ultrarelativistic Regime," *Phys. Rev. Lett.*, vol. 100, p. 085004, Feb 2008.

[50] Purvis, M. A., Shlyaptsev, V. N., Hollinger, R., Bargsten, C., Pukhov, A., Prieto, A., Wang, Y., Luther, B. M., Yin, L., Wang, S., and Rocca, J. J., "Relativistic plasma nanophotonics for ultrahigh energy density physics," *Nature Photonics*, vol. 7, no. 10, pp. 796–800, 2013.

[51] Qiu, R., Liu, J. C., Prinz, A. A., Rokni, S. H., Woods, M., and Xia, Z., "Analysis and Mitigation of X-ray Hazard Generated from High Intensity Laser-Target Interactions," *SLAC Publication*, no. SLAC-PUB-14351, 2011.

[52] Seltzer, S. M. and Berger, M. J., "Bremsstrahlung spectra from electron interactions with screened atomic nuclei and orbital electrons," *Nuclear Instruments and Methods in Physics Research Section B: Beam Interactions with Materials and Atoms*, vol. 12, no. 1, pp. 95 – 134, 1985.

[53] Seltzer, S. M. and Berger, M. J., "Bremsstrahlung energy spectra from electrons with kinetic energy 1 keV10 GeV incident on screened nuclei and orbital electrons of neutral atoms with Z = 1100," *Atomic Data and Nuclear Data Tables*, vol. 35, no. 3, pp. 345 – 418, 1986.

[54] Sircombe, N. J., Hughes, S. J., and Ramsay, M. G., "Integrated calculations of short-pulse laser interactions with matter," *New Journal of Physics*, vol. 15, no. 2, p. 025025, 2013.

[55] Spencer, I., Ledingham, K. W. D., McKenna, P., McCanny, T., Singhal, R. P., Foster, P. S., Neely, D., Langley, A. J., Divall, E. J., Hooker, C. J., Clarke, R. J., Norreys, P. A., Clark, E. L., Krushelnick, K., and Davies, J. R., "Experimental study of proton emission from 60-fs, 200-mJ high-repetition-rate tabletop-laser pulses interacting with solid targets," *Phys. Rev. E*, vol. 67, p. 046402, Apr 2003.

[56] Swanson, W. P., "Improved Calculation of Photoneutron Yields Released by Incident Electrons," *Health Physics*, vol. 37, 1979.

[57] Tabak, M., Hammer, J., Glinsky, M. E., Kruer, W. L., Wilks, S. C., Woodworth, J., Campbell, E. M., Perry, M. D., and Mason, R. J., "Ignition and high gain with ultrapowerful lasers," *Physics of Plasmas*, vol. 1, pp. 1656–1634, Jan 1994.

[58] Tajima, T. and Dawson, J. M., "Laser Electron Accelerator," *Phys. Rev. Lett.*, vol. 43, pp. 267–270, Jul 1979.

[59] Wilks, S. C. and Kruer, W. L., "Absorption of ultrashort, ultra-intense laser light by solids and overdense plasmas," *IEEE Journal of Quantum Electronics*, vol. 33, pp. 1954–1968, Nov 1997.

[60] Wilks, S. C., Kruer, W. L., Tabak, M., and Langdon, A. B., "Absorption of ultra-intense laser pulses," *Phys. Rev. Lett.*, vol. 69, pp. 1383–1386, Aug 1992.

[61] Woods, M., "Laser Beam Focusing and Propagation," *SLAC Memorandum: Laser Safety Technote*, no. 2010-1, 2010.

[62] Yang, B., Qiu, R., Li, J. L., Lu, W., Wu, Z., and Li, C., "Photon dose estimation from ultraintense lasersolid interactions and shielding calculation with Monte Carlo simulation," *Radiation Physics and Chemistry*, vol. 131, pp. 13 – 21, 2017.

[63] Zhao, Y., Zhang, N., Yang, J., and Zhu, X., "Laser-induced air ionization microscopy," *Appl. Phys. Lett.*, vol. 88, no. 24, p. 241102, 2013.